Universität Bonn

Argelander-Institut für Astronomie

On Higher Multipoles of Finger-of-the-Observer Effect

Kartik Tiwari

Dieser Forschungsbericht wurde als Masterarbeit von der
Mathematisch-Naturwissenschaftlichen Fakultät der Universität Bonn angenommen.

Angenommen am:	6th October 2025
1. Primary Supervisor:	Prof. Dr. Cristiano Porciani
2. Secondary Supervisor:	Prof. Dr. Peter Schneider

Acknowledgements

I would like to thank Prof. Cristiano Porciani for introducing me to the fascinating field of relativistic effects on the large scale structure and suggesting the interesting question of observer velocity that this dissertation tackles. I have derived great delight in my conversations with him throughout my graduate education in Bonn.

I would also like to thank Mohamed Yousry Elkhashab with whom I have shared the many joys and frustrations of debugging large codes and, albeit only over our weekly zoom calls, managed to develop a sincere friendship.

Daniele Bertacca and Mikolaj Borzyszkowski have played a crucial role in the development of `LIGER` i.e. a tool in the absence of which this research project would have been substantially more convoluted and, quite possibly, completely intractable.

My discussions with Dennis Lehmkuhl, Erik Curiel, Jonathan, Gal, Juliusz, Noah, Martin, Dan, Nurida and other members of the Lichtenberg Group for History and Philosophy of Physics have kept me distracted enough from my primary pursuits to ensure that I never lose sight of the forest for the trees.

Vips managed to make even the gloomiest winter days a little warmer. My friends Martina, Aarathi, Anik, Elyas, Vlad and Piet have made sure that Germany continues to feel like home.

Finally, I am immensely grateful for the generous funding of Bonn-Cologne Graduate School for making this wonderful education accessible to many students like me.

Abstract

Peculiar velocity (i.e. inhomogeneity-driven deviation from idealized Hubble flow) leaves distinct imprints on cosmological observations. Well known effects of peculiar velocity include the dipole anisotropy in the cosmic microwave background (CMB), caused by the observer's motion, and the apparent flattening or elongation of structures in galaxy redshift surveys, caused by the velocities of distant sources. Several attempts have been made to measure a dipole anisotropy in the matter distribution and relate it to the CMB dipole, but results remain inconclusive.

In this master's project, I build on a recently proposed technique for using Stage IV large-scale structure (LSS) surveys, such as Euclid and the Square Kilometer Array (SKA), to infer observer's peculiar velocity. This technique, called the Finger-of-the-Observer (FOTO) effect, utilizes general relativistic distortions arising from linear-order perturbations to Friedmann–Lemaitre–Robertson–Walker (FLRW) cosmology. My work focuses on modelling higher-order multipoles of the FOTO signal, assessing the feasibility of their detection, and estimating the additional constraining power they may provide. In particular, I set-up an efficient pipeline to generate 125 mock skies using a sequence of Einstein-Boltzmann solver, N-body initial condition generation, post-hoc application of linear order relativistic distortions and baryon painting via survey functions. I show that, under full sky assumption and using a wide redshift bin of a Euclid-like survey, FOTO effect can constrain observer velocity up to $\pm 16\%$ relative errors. Commenting on the statistical information contained within these mock skies, I describe how the multipole structure of the FOTO effect relates to signal-to-noise ratios, shrinkage in Bayesian inference posteriors and data compression techniques. Finally, on the basis of the underlying symmetries and the preceding statistical results, I argue that early truncations of the 1D power-spectrum multipole expansion recover most of the constraining power otherwise obtained by combining higher (more computationally demanding) multipole estimates.

Contents

Abstract **v**

1 Introduction **1**
1.1 Why Care about Peculiar Velocity? . . . 1
1.2 Historical Developments . . . 3
1.2.1 Analyzing Anisotropies . . . 4
1.2.2 Simulations and Surveys . . . 5
1.3 General Relativistic Redshift Space Distortions . . . 6
1.3.1 A Schematic of the Derivation . . . 7
1.3.2 Relativistic Effects, Step by Step . . . 9
1.3.3 Assembling Redshift Space Overdensity . . . 20
1.4 Isolating Finger-of-the-Observer Effect . . . 24

2 Methods **27**
2.1 Two-Point Statistics . . . 28
2.1.1 Global Plane-Parallel Approximation . . . 29
2.1.2 Yamamoto-Bianchi Estimator . . . 31
2.1.3 FOTO Multipole Moments . . . 33
2.1.4 FFT Implementations . . . 37
2.2 Generating Relativistic Mocks . . . 40
2.2.1 MonophonIC (`MUSIC2`) Newtonian Snapshots . . . 40
2.2.2 Light Cones in General Relativity (`LIGER`) . . . 41
2.2.3 `Buildcone` Routine . . . 43

3 Results **51**
3.1 Comparing FOTO Measurements . . . 51
3.1.1 Signal-to-Noise Ratio . . . 54
3.1.2 Bayesian Inference . . . 56
3.2 Discussion . . . 65
3.3 Outlook . . . 67
3.3.1 Anisotropic Cosmological Models . . . 67
3.3.2 Challenges and Prospects . . . 69
3.4 Summary . . . 72

Bibliography **75**

List of Figures 87

List of Tables 93

"I and this mystery, here we stand."

— *Leaves of Grass*, Walt Whitman

CHAPTER 1

Introduction

1.1 Why Care about Peculiar Velocity?

An observer's motion through the universe imprints itself on cosmological observations as well as their theoretical interpretations. Therefore, this work is concerned with refining a recently proposed technique (Elkhashab, Porciani and Bertacca, 2024) to measure the motion of an observer moving with respect to the cosmic filaments and voids.

One of the essential insights underlying modern precision cosmology is the idea of an everywhere isotropic universe. In such an idealized model of a universe, no spatial location is privileged and all matter uniformly recedes from everything else, comoving along the Hubble flow of cosmic expansion. The presence of structure implies that the universe deviates from the aforementioned 'Cosmological Principle' because, on sufficiently small scales, points in space can be slightly denser or less dense than their surroundings. The observed distortions in our redshift survey maps (discussed in §1.3) establish that although distant galaxies and galaxy clusters primarily appear to be moving farther, there is also another, more intricate, component of the velocity field tracing the grooves in gravitational potential carved by the large scale structure. This deviation in motion is called the observer peculiar velocity when referring to our solar system and, often, just peculiar velocity when the referent is a distant galaxy. Both kinds of peculiar velocities are vitally connected to our understanding of cosmic inhomogeneities and structure formation. The peculiar velocity of galaxies, by virtue of it imparting a more noticeable distortion in our surveys, has received substantial attention (Hamilton, 1998). However, for reasons described in the following paragraphs, we argue that observer peculiar velocity warrants further investigation into its nature and magnitude, especially in light of modern observational capabilities unlocked by projects like Euclid (Euclid Collaboration et al., 2025) and SKAO (Aharonian et al., 2013).

To more concretely understand the 'vital connection' between observer peculiar velocity and our standard model of cosmology, consider the dipole anisotropy of the most important primordial relic of the Hot Big Bang – Cosmic Microwave Background (CMB) radiation. By 1970, studies had already shown that, in contrast to the ideal theoretical picture of a completely isotropic CMB, one half of the sky appears to be hotter than the other half. The discovery of CMB was immediately followed by several competing attempts to measure the dipole anisotropy and, thus, the 'firsts' are hard to isolate but we suggest consulting Lineweaver (1996) for one chronological listing of early dipole measurements.

The allure of studying the CMB dipole was manifold. For instance, J. M. Stewart and Sciama (1967) interpreted the dipole as a consequence of the motion within our super-cluster and studied it with an interest in trying to validate Mach's principle (Huggett, Hoefer and Read, 2024). Arguably, however, one of the most consequential aspects of the kinematic dipole discovery was ironically its systematic subtraction from the CMB maps, which revealed the rich oscillatory features corresponding to Baryon Acoustic Oscillation (BAO). These oscillations in the CMB power spectrum, which 'become visible' only after accounting for the dipole correction, have strengthened our understanding of processes occurring even before 'the first light'. The dipole correction (i.e. Lorentz boosting to the rest frame defined by an apparently isotropic CMB to cancel our peculiar velocity) is a crucial systematic that appears in a vast majority of our cosmological parameter estimations involving the early universe. Considering the ubiquitous nature of this correction, it would be a naturally lucrative problem to acquire a reliable understanding of our motion through various measurement techniques independent of the CMB.

Now, further consider the fact that the status of compatibility between our peculiar velocity measurements using probes of the early universe (i.e. using CMB data from Planck Collaboration et al. (2020)) and late universe (i.e. using LSS) is currently a shaky affair (Secrest et al., 2022). To summarize the disagreements, we must begin with Ellis and Baldwin (1984) who proposed that if the kinematic interpretation of the dipole is correct then there should also be a corresponding anisotropy in the distribution of luminous sources in the sky. Although, in principle, the strength of this method lies in its largely model independent prescription, in practice, observational subtleties have led to a puzzling collection of claims. Based on the technique by Ellis and Baldwin (1984), some studies (using radio continuum galaxies) indicate a good compatibility between the different peculiar velocity measurements (Darling, 2022) while other analyses (utilizing infrared galaxies in CatWISE data (Eisenhardt et al., 2020)) claim a 5σ discrepancy (Singal, 2021; Dam, G. F. Lewis and Brewer, 2023). The situation is further aggravated when we consider that for a $v_{\text{obs}} = 370$ km/s, the dipole in the number count across the sky would only be enhanced by 0.5% (Dam, G. F. Lewis and Brewer, 2023). We have summarized a small selection of claims made about the magnitude of peculiar velocity on the basis of late universe measurements in Fig. 1.1. In the context of the potential dependence of such results on sky cuts, estimator bias, selection effects, etc., Elkhashab, Porciani and Bertacca (2024) succinctly describe the situation in the following sentence – "A dipole anisotropy consistent with the CMB one (Blake and Wall, 2002) and a signal discrepant both in amplitude and direction (Gibelyou and Huterer, 2012) have been extracted from the same catalog".

In this work, we study a possible extension[1] of a novel independent probe (using relativistic distortions on the power spectrum) that can serve as a potential tie-breaker over the current scientific disagreements. We acknowledge that, unlike Ellis and Baldwin (1984), our suggested measurement methodology depends on the underlying cosmological model. But the compatibility of peculiar velocity measurements between the early and late universe can serve as another addition in the long list of achievements for ΛCDM. Furthermore, an incompatibility could constrain our search for a theoretical alternative that accommodates this tension (a brief review of such models would be presented in §3.3.1). Besides being a pressing necessity at this juncture, in the following sections I hope to demonstrate that the proposed tie-breaker - Finger-of-the-Observer (FOTO) Effect (Elkhashab,

---

[1] By 'extending', I mean extending the statistical estimators to higher-order multipoles (as opposed to the current state-of-the-art which employs only the power spectra monopole) in order to extract more information about our peculiar velocity from the survey data. These details become clearer in Chapter 2.

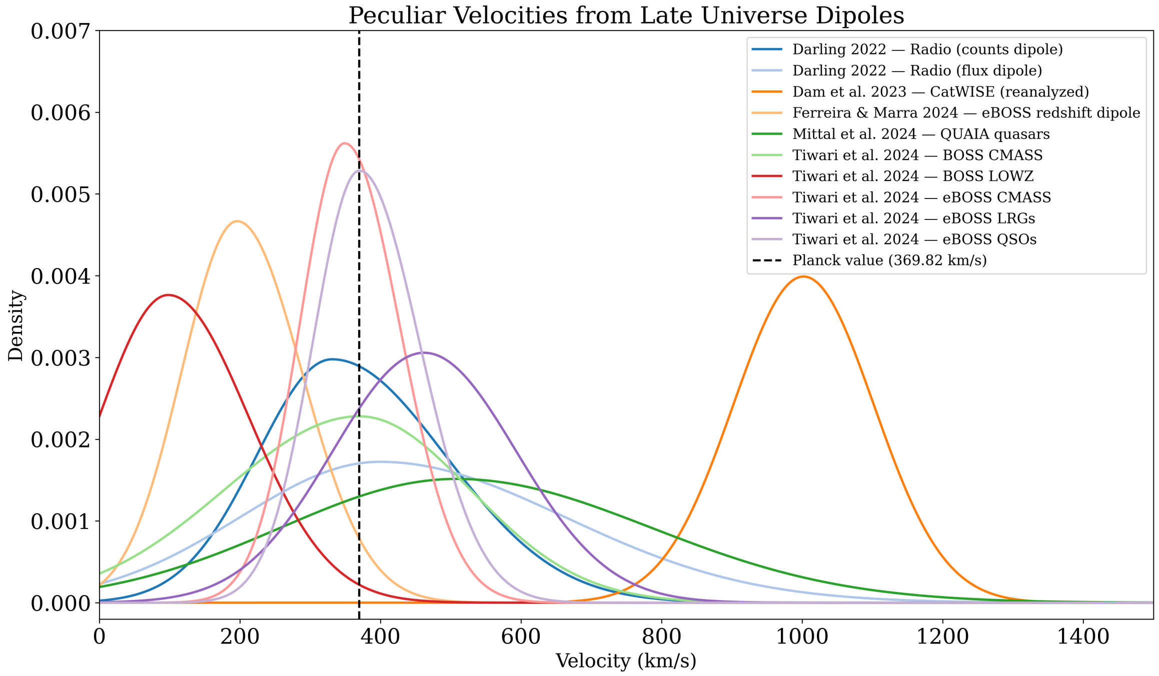

Figure 1.1: Comparing a selection of claims in literature about observer peculiar velocity as inferred from a late universe dipole. We see that while some measurements are in general agreement with the CMB measurement (vertical dashed line), other can display a tension up to 4.9σ. Measurements and errors are reported from Darling (2022), Dam, G. F. Lewis and Brewer (2023), P. d. S. Ferreira and Marra (2024), Mittal, Oayda and G. F. Lewis (2023), Tiwari et al. (2024) and Planck Collaboration et al. (2020). Also see Fig. 1 of P. d. S. Ferreira and Marra (2024) for a comparison between a different set of late universe dipole measurements.

Porciani and Bertacca, 2024) - is also a fascinating aspect of perturbative cosmology.

1.2 Historical Developments

Constructing the theoretical scaffolding to describe the nature of the Finger-of-the-Observer (FOTO) signal and to generate forecasts for upcoming surveys requires the careful assembly of several results from the perturbative, general relativistic treatment of cosmological large-scale structure (Challinor and A. Lewis, 2011; Jeong, Schmidt and Hirata, 2012). Considering the chain of mathematical reasoning that the remainder of this chapter is dedicated to, it is appropriate to contextualize these theoretical results with some landmark developments that have enabled much of the science contained within this thesis.

The conceptual origins of large-scale structure cosmology can be traced back to the early developments in GR around 1920. Einstein initially rejected the idea that the universe of matter might be a limited island in asymptotically flat space because such a cosmology conflicted with Mach's Principle (Peebles, 2022). The conflict arises because Einstein believed that, in such a configuration, a star could travel arbitrarily far from the 'island universe' while retaining its inertial properties[2]. At first, Einstein toyed with solutions to this conflict with line elements that become singular outside the realm of matter but was soon drawn to the more elegant solution of a homogeneous closed universe. Hence, strikingly, the idea of grounding cosmology in homogeneity predates even the discovery of other galaxies. Once this insight crystallized, discussions of homogeneous solutions to the Einstein field equations with varying matter contents entered the scientific zeitgeist.

---

[2] The question regarding the stability of 'finite matter islands' situated in infinite space has been discussed much before

1.2.1 Analyzing Anisotropies

One of the earliest scientific efforts towards analyzing the dipole anisotropy on the celestial sphere was made by James Bradley in 1728, when he observed and partially explained something conceptually similar to the Finger-of-the-Observer Effect. Bradley had observed a 'wobbling' of stellar positions and he correctly identified it as our own velocity painting the sky with a dipole (Bradley, 1728).

Bradley was trying to detect the parallax in γ-Draconis but did not find the expected helical motion around the true position. Theoretically, the star should have been at its lowest point in December and the highest in June but, instead, the maxima and minima were achieved in March and September respectively. He hypothesized that the deviation from the timetable arose because, besides the expected parallax effect, there was an additional contribution to the motion of the star. The phenomenon that Bradley had discovered is called *aberration* (Kovalevsky, 2003) i.e. an apparent motion displayed by a celestial object around its true position. The modern ideas of relativistic beaming and light time corrections are related to aberration but it is notably distinct from the effects of parallax.

Even in 1727, with barely a hundred years of decent astrometric observations, Bradley could explain this aberration in terms of the finite speed of light through a series of highly intricate (and interesting) arguments (Bradley, 1728)[3],[4]. Beyond providing an explanatory model, Bradley also used his observations to measure the speed of light. However, these observations were incompatible with the 18th century theories of light and became a motivation for aether drag ideas which were later developed by people like Fresnel and Stokes in the 19th century (Schaffner, 1972).

Moving ahead two centuries from the time of Bradley, through the developments in general relativity, cosmology and non-galactic astrophysics, we arrive at the 'cosmology on null cone' proposal by Kristian and Sachs (1966). They present their work on matter inhomogeneities with a modest introduction claiming that nothing that is not implicit in the literature is introduced in assembling their conceptual framework and that they are only 'applying these results to a specific problem'. According to them, the three 'results of note' from their paper (Kristian and Sachs, 1966) were that

1. All cosmological models (GR or not) satisfy a relation between infinitesimal area elements and solid angles, i.e. $dA = r^2\, d\Omega$, where r is the corrected luminosity distance[5].

2. Knowledge over only one side of the universe should be taken very cautiously and it is the variation of effects on the celestial sphere which give decisive information.

Einstein and Mach. I do not intend to suggest that homogeneous cosmologies were Einstein's original invention. Consult Chapter IX of Schlick (2007) for a more insightful summary.

[3] The (probably apocryphal) story says that he got this breakthrough insight on noticing that people who are walking in the rain need to hold their umbrellas at an angle corresponding to their pace.

[4] Interestingly, this discovery by Bradley was published in the Royal Society's Philosophical Transactions, which is considered to be the first and, as of now, the oldest-running scientific journal.

[5] In a personal correspondence with Sachs, Penrose provided another independent proof of this

3. There is a distortion effect which squashes distant spherical objects into ellipses on the photographic plates and this can be measured.

In 1987, Kaiser investigated these ‘squashing’ distortions further (arising due to coherent inflow velocities within large structures) and studied the presence of a quadrupole[6] in the Shapley-Ames catalog (Kaiser, 1987). Soon after this landmark paper, Hamilton (1998) gave Kaiser’s results (more specifically, the result in the regime of smaller virialized structures) a much more evocative name, calling the radial stalactite-like patterns ‘Fingers of God’. It is as a play on (and an ode to) this iconic ‘Finger of God Effect’, that Elkhashab, Porciani and Bertacca (2024) call the effect arising from our peculiar velocity ‘Finger-of-the-Observer’ effect. Admittedly, the FOTO signal in redshift survey maps does not particularly resemble fingers in appearance (see §2.1.1). Nevertheless, it remains a fitting name as it corresponds to a metaphorical fingerprint of our motion on the apparent matter distribution in the sky.

1.2.2 Simulations and Surveys

These conceptual seeds along with several others, over time, led to a dramatic increase in our observational and computational cosmology capabilities. A landmark paper by Davis et al. (1985) introduced one of the first ‘large’ n-body simulations of structure formation in our universe [7]. Though groundbreaking for its time with 64^3 grid cells and roughly 30,000 particles, it was orders of magnitude coarser than today’s flagship simulations (such as FLAMINGO (Schaye et al., 2023)), which feature gigaparsec boxes and upwards of 10^{11} particles.

Observationally, the improvement in our maps of galaxy distribution has been equally dramatic. For instance, one of the first maps of the LSS was the iconic image by Lapparent, Geller and Huchra (1986) that consisted of 1100 galaxies measured across 700 square degrees of the sky. In comparison, a current generation survey like DESI (DESI Collaboration et al., 2016) can contain up to 30 million objects and map over 15,000 square degrees[8]. Our mapping capabilities have grown so tremendously that the very discipline has been reshaped. Yet, despite this progress, from one perspective, our cosmic maps might still resemble the early paradigm-establishing cartographic efforts of Herodotus and Ptolemy. The current data, while revealing many answers, invariably underscores the vastness of what remains unknown. Hence, the pursuit of refinement, cross-validation, and theoretical deepening continues.

The study of the large scale web-like structure of the visible universe has proven itself to be a highly promising discipline, revealing connections to dark energy (Schimd, 2009), primordial non-Gaussianity (Desjacques and Seljak, 2010), modified gravity (Clifton, P. G. Ferreira et al., 2012) and more. One particularly promising probe to study this large scale structure and constrain cosmological parameters, is a collection of effects termed *Redshift Space Distortions* (Hamilton, 1998), which I shall now discuss in some detail.

---

[6] We will return to the power spectrum quadrupole when we discuss multipole expansions in §2.1.1.

[7] Although even earlier attempts had been made to perform analog calculations of particles moving only under the influence of gravity using light bulbs by Holmberg (1941), leveraging the fact that both gravity and light-flux follow an inverse squared distance relation

[8] In a public interview titled The forest was full of cities we couldn’t see, Mesoamerican archaeologist Fransisco Estrada-Belli, describing the LIDAR mapping of ancient Tikal, said “In five minutes, we discovered more sites than in my entire career.” A similar sentiment aptly captures the scale of modern redshift surveys.

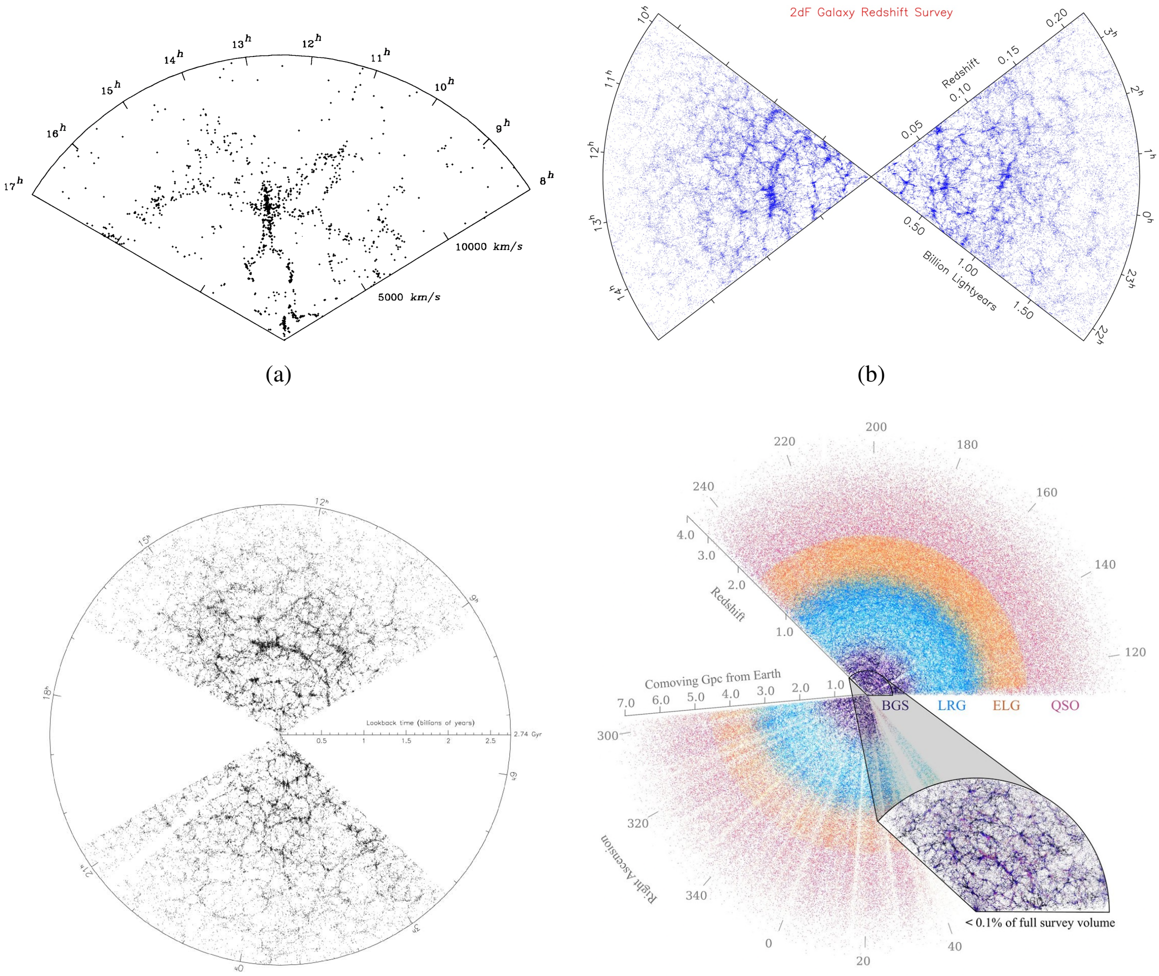

(a) (b)

(c) (d)

Figure 1.2: Wedges from early and modern surveys illustrating filaments and voids in the large scale matter distribution: (a) Center for Astrophysics (CfA) Survey (Lapparent, Geller and Huchra, 1986); (b) 2 degree Field Galaxy Redshift Survey (2dFGRS) (Cole et al., 1998); (c) Sloan Digital Sky Survey (SDSS)(Gott III et al., 2005); (d) Dark Energy Spectroscopic Instrument (DESI) Survey (with inverted colors) (DESI Collaboration et al., 2016).

1.3 General Relativistic Redshift Space Distortions

The only relevant direct measurements accessible while mapping the large scale structure are the sky position and redshift of the tracer galaxies. The choice of cosmological model determines a distance-redshift relationship, allowing us to convert coordinates in redshift space (acquired directly through the survey) to real-space coordinates (and vice-versa). Since the coordinate conversion is dependent on the choice of cosmology, we obtain different redshift space maps for ideal FLRW and perturbed FLRW, even if we apply the mappings to the same underlying real-space structures. Current cosmological surveys can be sensitive to these differences caused by metric perturbations (Elkhashab, Bertacca et al., 2024) and, hence, our conversions between real-space and redshift space quantities should be based on the relations derived using the perturbed FLRW cosmology. When we derive these relations later in this section, it would be helpful to remember the key move that is being made – *we are transforming real-space coordinates into the observed over-density fields, by tracing how photon trajectories and volume elements are distorted in slightly curved, expanding spacetime.*

This section sets the stage by introducing the general formalism that underpins our approach and the following section §1.4 will then focus on disentangling the specific imprint of the FOTO effect from the broader tapestry of redshift-space distortions. In §1.3.1, I lay out a schematic which illustrates the sequence of steps, at a glance, that we need to take in order to accomplish the 'key move'. Then, §1.3.2 will present the actual mathematical steps described in the schematic map. Lastly, before isolating the FOTO signal, we briefly interpret the various terms appearing in our final result[9].

1.3.1 A Schematic of the Derivation

At a conceptual level, the task of transforming from real-space positions to redshift space overdensities can be broadly stated as a sequence of three moves. First, we establish how the redshift and sky position of every photon is shifted due to metric perturbation; this gives us a coordinate map from real-space to what the survey measures. Second, we describe how the map deforms volumes and solid angles. Third, we trace the impact of the deformed volumes on the survey's selection function (via magnification and evolution biases). These three central pieces give all the terms required to assemble the FOTO signal (as we will do in §1.3.3).

For organizing the algebra, one convenient heuristic is to expand these three fundamental ideas into the following seven concrete stages.

1. Declaring **Gauge and Notation**
   a) Describe scalar-restricted synchronous comoving gauge and the Poisson gauge,
   b) Adopt the 'Cosmic Rulers Prescription', which relates real-space coordinates with redshift-space counterparts,
   c) Define differential operators along line-of-sight $\nabla_{\|}$ and transverse $\nabla_{\perp}$ directions.
2. Asserting the **Conservation of Galaxy Number Counts**, which will serve as the fundamental link between real and redshift space.
3. Using the **Geodesic Vector** to find the form of coordinate shifts:
   a) The time component of the real-space geodesic vector yields a frequency shift δf,
   b) The spatial component yields a shift in direction δn^{i},
   c) These quantities are calculated by solving the geodesic equation to first order in Steps 4 and 5.
4. Computing the **Redshift Perturbation** δz (or, equivalently, scale factor perturbation $\delta \ln a$)
   a) Including the classic Doppler term (i.e., the Kaiser piece),
   b) Local gravitational potential terms,

---

[9] Standard derivations from cosmological perturbation theory about structure growth, the kinds one would expect to encounter in a graduate level advanced course on the topic, have not been recapitulated in the interest of brevity. Detailed discussions on all such topics can be found in the textbook by Peebles (2020).

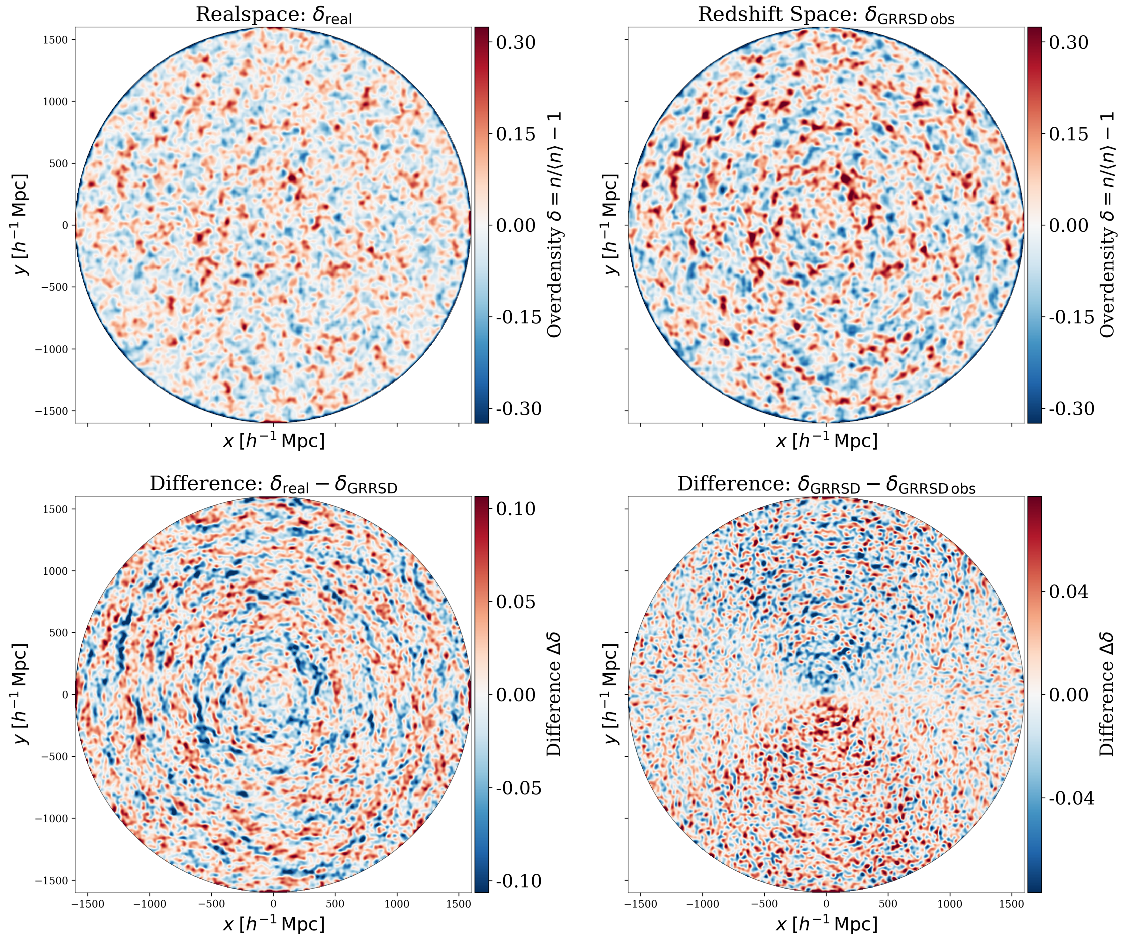

Figure 1.3: Visualizing impact of linear-order general-relativistic redshift-space distortions (GRRSD). Simulated large-scale matter distribution on an observer light-cone shown within an equatorial slice ($z \in [-250, 250]\, h^{-1}$Mpc) and with a Gaussian smoothing kernel ($\sigma = 1.8$px). Top Left: Dark matter overdensities as represented in their real-space positions. Top Right: Same filaments and voids after including GR-RSD in heliocentric frame. Bottom Left: The difference between real-space overdensities and the overdensities represented in redshift space for an observer in the CMB frame. Here, one can see large-scale concentric compression (Kaiser effect). Bottom Right: The difference between overdensities in redshift space for CMB and heliocentric frames. The most noticeable effect is the dipole in the overdensities induced by the observer velocity. While these features are already suggestive, the full cosmological information encoded in these distortions can only be harvested with the systematic modeling and estimators described later in this thesis. See §2.2.2 for details of the LIGER method used to generate these mock observations.

   c) Integrated Sachs-Wolfe (ISW) contributions.

5. Computing the **Coordinate Maps** Δx^μ
   a) The temporal shift Δx^0 uses contributions from Step 4,
   b) The spatial shift Δx^i derives from the deflection δn^i in Step 3.

6. Computing the **Volume Distortion (Jacobian Terms)**
   a) Compute the metric determinant to linear order and the volume Jacobian deformation,
   b) Express the change in volume ΔV in terms of lensing convergence κ.

7. Calculating the new **Bias Terms** (apart from linear bias) using number density perturbation
   a) The magnification bias $Q(z)$ accounts for sources made visible by lensing-induced flux magnification,
   b) The evolution bias $\mathcal{E}(z)$ captures deviations from a static luminosity function across redshift.

Once we go through these seven steps, we can assemble all the required pieces in §1.3.3 and also recover the well-known Kaiser term in the non-relativistic limit. Finally, then, we would be in a position to isolate the effects of observer peculiar velocity on overdensity maps in the redshift space.

1.3.2 Relativistic Effects, Step by Step

Now, we will fill the above-described schematic with the complete mathematical details and, at certain points, note some features of interest.

1. **Gauge and Notation** follows, mostly, Bertacca (2015):
   To bridge the theoretical nature of the FOTO signal with the forecasts of potential observables, we invariably require simulations which can forward model 'mock skies' (discussed in §2.2). One way to simulate the relativistic distortions on the large-scale structure would be to run a numerical relativity program which is meant to solve a highly non-linear, strongly coupled set of partial differential equations (called the Einstein Field Equations) corresponding to our cosmological model (Adamek et al., 2013; Adamek et al., 2016). This is possible but it is a very involved, expensive and delicate technique. The alternative strategy, applicable for a system which deviates only slightly from an otherwise highly symmetric and idealized model, would be to expand all the relevant quantities as a power series and to solve for the first order perturbations to the necessary equations. This is the strategy adopted in the `LIGER` method[10] (Borzyszkowski, Bertacca and Porciani, 2017) and it considerably reduces the computational demands while forward modeling the relativistic effects. The gain in computational efficiency is afforded at the cost of being applicable only to the first order statistics. But, when we discuss the results in greater detail, we will show that interesting observables become accessible already at the level of first order perturbations (Elkhashab, Porciani and Bertacca, 2021; Borzyszkowski, Bertacca and Porciani, 2017).
   There is, however, one issue that is ubiquitous among such perturbative treatments in physics

---

[10] This will be described in greater detail in §2.2.2.

— perturbations do not ‘really’ exist out there in our universe. Nature provides us with some distribution of physical quantities (like density or temperature) but she does not explicitly label or demarcate how much of the measured quantity should have been there as opposed to how much of it is the deviation from the ideal situation. In other words, when we order effects in a perturbative expansion, we introduce redundant structure in our theory and the underlying physics should remain invariant to the choice of this additional structure[11]. In practice, this means that there are some variables in our formalism which we have freedom to choose (Clifton, Gallagher et al., 2020) . More specifically, in our case, the choice of foliating the four-dimensional Riemannian manifold with three-dimensional hypersurfaces is the arbitrary structure that we introduce[12]. Such a ‘slicing’ of our cosmic history is one manifestation of a more general procedure called ‘Gauge Fixing’.

As mentioned earlier, this choice can be made arbitrarily as per our convenience (Clifton, Gallagher et al., 2020) and it should not affect any physical observables. In our case, there are two distinct ‘conveniences’ that can be achieved by two different gauge choices. In *Synchronous Comoving Gauge* (SC) (Bruni et al., 2014; Bartolo et al., 2010), the Hubble flow vanishes because the coordinate grid co-moves with the matter. This makes it computationally convenient and gives a direct definition of the local bias using a ‘peak background-split’ approach i.e. $\delta_\mathrm{g} = b\,\delta_\mathrm{SC}$. On the other hand, *Conformal Newtonian Gauge* gives clear and intuitive interpretations to certain variables. The FOTO signal, like other measurable quantities, is gauge invariant and we can use either of the gauges to perform our calculations. It is a common practice in cosmological perturbation theory to use multiple gauges depending on the aspect of the problem being solved (Ma and Bertschinger, 1994). We can do the same once we establish how quantities in the two gauge choices are related to each other. Similar treatments have also been performed in longitudinal gauge (Green and Wald, 2012) and in completely gauge-invariant ways too.

First we begin by connecting the Newtonian quantities to the SC gauge. Later, we will relate the SC gauge to Conformal Newtonian Gauge. For natural units, a metric element can be written in the SC gauge as

$$ds^2 = a^2(\tau)\left[-d\tau^2\gamma_\mathrm{ij}\,dx^\mathrm{i}dx^\mathrm{j}\right] \tag{1.1}$$

where a is the scale factor, τ is the conformal time and γ_ij is the spatial metric. We also assume irrotational dust flow with fundamental observers possessing four-velocity $u_\mu = [-a, 0, 0, 0]$ (i.e. the unperturbed geodesics are aligned with the world-lines of our ‘fundamental’ observers and the cosmic time coincides with the proper time of fluid elements).

Next, we define the deformation tensor which contains information about volume expansion.

$$\mathcal{D}^\mu_\nu \equiv a u^\mu_{;\nu} - \mathcal{H}\delta^{K\mu}_\nu \tag{1.2}$$

where the semicolon denotes the covariant derivative, $\mathcal{H} = a'/a$ with primes denoting conformal time derivatives (i.e. equivalent to saying $\mathcal{H} = aH$) and δ is the density contrast. The trace $\mathcal{D}$ and traceless $\mathcal{D}^{TS\mu}_\nu$ components of the deformation tensor corresponds to inhomogeneous and anisotropic parts of the volume expansion. In our case, since the deformation tensor is purely spatial, we can substitute the Greek indices with the Latin ones and relate them to the components of the spatial metric

---

[11] Gomes (2025) is a concise distillation of Henrique Gomes’ decade long effort of carefully investigating important philosophical considerations surrounding gauge freedom and gauge fixing — concepts that permeate our modern scientific worldview, from cosmology to conformal field theories.

[12] This is done by selecting an appropriate lapse function and a shift vector, which describe how points on one 3D hypersurface get mapped to the next adjacent hypersurface.

$$\mathcal{D}^{\mathrm{i}}_{\mathrm{j}} = \frac{1}{2}\gamma^{ik}\gamma'_{kj}. \tag{1.3}$$

Following standard textbook prescriptions, we get the relativistic energy conservation equation in SC gauge as

$$\delta'_{\mathrm{SC}} + (1 + \delta_{\mathrm{SC}})\mathcal{D} = 0 \tag{1.4}$$

and an evolution equation for the trace of the deformation tensor

$$\mathcal{D}^2 + \mathcal{H}\mathcal{D} + \mathcal{D}^{\mathrm{i}}_{\mathrm{j}}\mathcal{D}^{\mathrm{j}}_{\mathrm{i}} + \frac{3}{2}\mathcal{H}^2\Omega_{\mathrm{m}}\delta_N = 0 \tag{1.5}$$

where the subscript N depicts that the quantity is expressed in Newtonian gauge. Next, we linearize the spatial metric

$$\gamma_{\mathrm{ij}} = (1 - 2\zeta)\ \delta^K_{\mathrm{ij}} + \left(\partial_{\mathrm{j}}\partial_{\mathrm{j}} - \delta^K_{\mathrm{ij}}\nabla^2\right)\chi \tag{1.6}$$

by writing it in terms of the two scalar potentials ζ and χ. The metric degrees of freedom are summarized by two scalar quantities here because we are ignoring the vector and tensors degrees of freedom as they remain linearly independent at the first order of perturbations. These scalar potentials in SC gauge are related to the two gauge invariant Bardeen potentials (Bardeen, 1980)

$$\Phi_B = -\frac{1}{2}\left(\chi'' - \mathcal{H}\chi'\right), \tag{1.7}$$

$$\Psi_B = \zeta + \frac{1}{6}\nabla^2 + \frac{1}{2}\mathcal{H}\chi \tag{1.8}$$

where Φ can be directly interpreted as the Newtonian-like gravitational potential and Ψ which matches Φ for vanishing anisotropic stress (i.e. no neutrino shear). Since the Bardeen potential Φ acts like the Newtonian gravitational potential, it can be computed with a Poisson-like equation sourced from matter overdensity

$$\nabla^2\Phi_B = \frac{3}{2}\mathcal{H}^2\Omega_{\mathrm{m}}\delta_{\mathrm{SC}} \tag{1.9}$$

which allows us to match the relativistic and Newtonian prescriptions. For instance, consider the Newtonian equations corresponding to a perturbed cosmological fluid

$$\frac{\partial\delta_N}{\partial\tau} + \nabla.\left[(1 + \delta_N)\boldsymbol{v}\right] = 0, \tag{1.10}$$

$$\frac{\partial(\nabla.\boldsymbol{v})}{\partial\tau} + \mathcal{H}\nabla.\boldsymbol{v} + \nabla.(v.\nabla)\boldsymbol{v} + \frac{3}{2}\mathcal{H}^2\Omega_{\mathrm{m}}\delta_N = 0, \tag{1.11}$$

$$\frac{3}{2}\mathcal{H}^2\Omega_{\mathrm{m}}\delta_N = \nabla^2\varphi. \tag{1.12}$$

To match the SC gauge, we rewrite the Newtonian equations in Lagrangian coordinates using the substitution

$$\frac{d}{d\tau} = \frac{\partial}{\partial\tau} + \boldsymbol{v}.\nabla \tag{1.13}$$

which gives us

$$\frac{\partial\delta_N}{\partial\tau} + (z+\delta_N)\mathcal{D}_N = 0, \tag{1.14}$$

$$\frac{\partial\mathcal{D}_N}{\partial\tau} + \mathcal{H}\mathcal{D}_N + \mathcal{D}^{\mathrm{i}}_{Nj}\mathcal{D}^{\mathrm{j}}_{Ni} + \frac{3}{2}\mathcal{H}^2\Omega_{\mathrm{m}}\delta_N = 0 \tag{1.15}$$

where we have also defined $\mathcal{D}^{\mathrm{i}}_{Nj} = \partial^{\mathrm{i}}\partial_{\mathrm{j}}\phi$ with ϕ being the scalar potential. With this, we now have a clear dictionary to translate the Newtonian quantities to the relativistic linear order formalism in SC gauge. This is given by

$$\frac{1}{d\tau} \longrightarrow \frac{\partial}{\partial\tau} \tag{1.16}$$

$$\delta_N \longrightarrow \delta_{\mathrm{SC}} \tag{1.17}$$

$$\partial^{\mathrm{i}}v_{\mathrm{j}} \longrightarrow \mathcal{D}^{\mathrm{i}}_{\mathrm{j}} \tag{1.18}$$

$$\phi \longrightarrow \Phi_B. \tag{1.19}$$

We needed such a dictionary to use the dual-gauge approach because, in SC gauge, the potential computed via the Poisson equation does not correspond to the perturbative metric scalar degree of freedom. Secondly, the simulation peculiar velocities are not matched to the relativistic peculiar velocities (because the latter vanishes, by construction, in SC gauge). However, there is one gauge choice that allows us to have the 'best of both worlds' with one single gauge choice. This is called the scalar-restricted Poisson gauge (also called conformal Newtonian gauge) (Chisari and Zaldarriaga, 2011), given by

$$ds^2 = a^2(\tau)\left[(1+\psi)d\tau^2 + (1+\phi)\delta^K_{\mathrm{ij}}\,dx^{\mathrm{i}}dx^{\mathrm{j}}\right]. \tag{1.20}$$

Poisson gauge solves both problems with the SC gauge because the metric potentials directly coincide with Bardeen potentials and the peculiar velocities match the Newtonian peculiar velocities (assuming no velocity bias (Chisari and Zaldarriaga, 2011)). However, in this gauge the peak-background split approach (Jeong, Schmidt and Hirata, 2012) can no longer be applied. Thus, the linear bias is accounted for by the following transformation (Challinor and A. Lewis, 2011; Jeong, Schmidt and Hirata, 2012)

$$\delta_{g,P} = b\,\delta_{\mathrm{SC}} + (3-\mathcal{E})\,\mathcal{H}\,\Phi_v. \tag{1.21}$$

where Φ_v is the linear velocity potential and δ_{SC} is the dark matter overdensity in synchronous-comoving gauge.

Another helpful choice of convention for this derivation is to adopt the 'Cosmic Rulers Prescription' (Schmidt and Jeong, 2012), which allows us to relate physical coordinates with redshift space counterparts perturbatively. If we define $\boldsymbol{n} \equiv \boldsymbol{x}/x$ as the observed direction, then we describe the null geodesic of a photon x^{μ} in redshift space with following coordinate frame (for a spatially flat universe)

$$x^{\mu} = \left(c\eta_0 - x, x\boldsymbol{n}\right) \tag{1.22}$$

where $\eta_0 = \eta + x/c$ is the present day value of the conformal time η. Note, that x here is computed using the background universe (i.e. ideal FLRW without perturbations)

$$x(z) = \int_0^z \frac{c dz'}{H(z')}. \tag{1.23}$$

The inner product for these coordinates can be computed using FLRW written in the conformal coordinates

$$ds^2 = a^2(\eta)\left[-c^2 d\eta^2 + \delta^K_{\mathrm{ij}} dx^{\mathrm{i}} dx^{\mathrm{j}}\right]. \tag{1.24}$$

Before computing the coordinate shifts which relate the physical coordinates to their redshift counterparts i.e. the Δx^{μ} in

$$x^{\mu}_{\mathrm{r}}\left(x_{\mathrm{r}}\right) = x^{\mu}(x) + \Delta x^{\mu}(x), \tag{1.25}$$

we define some notation that will simplify later expressions. For a vector $\mathbf{A}$, we can define its parallel and orthogonal components as

$$\boldsymbol{n}.\boldsymbol{A} = n_{\mathrm{i}}A^{\mathrm{i}} = A_{\|}\, ,\, A^{\mathrm{i}}_{\perp} = A^{\mathrm{i}} - n^{\mathrm{i}}A_{\|}. \tag{1.26}$$

The same can be extended to the gradient operators

$$\frac{\partial}{\partial x^{\mathrm{i}}} = \partial_{\mathrm{i}}, \tag{1.27}$$

$$\boldsymbol{n}.\boldsymbol{\nabla} = n^{\mathrm{i}}\partial_{\mathrm{i}} = \partial_{\|}, \tag{1.28}$$

$$\partial_{\perp,\mathrm{i}} = \partial_{\mathrm{i}} - n^{\mathrm{i}}\partial_{\perp}, \tag{1.29}$$

$$\boldsymbol{\nabla}^2_{\perp} = \partial_{\perp,i}\partial^{\mathrm{i}}_{\perp} = \delta^{Kij}\partial_{\mathrm{i}}\partial_{\mathrm{j}} - \partial^2_{\|} - \frac{2}{x}\partial_{\|}. \tag{1.30}$$

Finally, the affine parameter adopted for all calculations is the redshift space comoving distance x. Consequently, the total derivatives for any quantity would be

$$\frac{d}{dx} = \frac{-1}{c}\frac{\partial}{\partial\eta} + \boldsymbol{n}.\boldsymbol{\nabla} = \frac{-1}{c}\frac{\partial}{\partial\eta} + \partial_{\|} \tag{1.31}$$

2. **Asserting Galaxy Number Conservation**
   In the previous step, we largely established the conventions that our formalism follows. The first ‘real’ step in deriving the relativistic distortions is to assert the conservation of the number of galaxies. More formally, we can describe the physical number of galaxies of some population in a given volume $\mathcal{V}$ as

$$\mathcal{N} = \int_{\mathcal{V}} a^3_{\mathrm{r}}\left(x^0_{\mathrm{r}}\right) n_{\mathrm{g}}\left(x^{\mu}_{\mathrm{r}}, F_{\mathrm{r}}\right)\, d\mathcal{V}_{\mathrm{r}} \tag{1.32}$$

where n_g is the physical number density, a_r is the real-space scale factor, F_r is the flux and and x_r^μ are the physical comoving coordinates. The same $\mathcal{N}$ can be equated to the number of galaxies in the redshift space for some flux-limited survey with only those which have an observed flux greater than the survey flux limit (i.e. $F_\mathrm{r} > F_\mathrm{lim}$). The number of galaxies, then, by construction becomes

$$\mathcal{N} = \int_{\mathcal{V}} a_\mathrm{r}^3 \left(x^0\right) n_\mathrm{g} \left(x^\mu, F > F_\mathrm{lim}\right) d\mathcal{V} \tag{1.33}$$

where the scale factor, coordinates, flux and volume element are not written in redshift space (thus, without the subscript r which represented 'real-space'). In the redshift space, x^μ are the observed coordinates and the scale factor is $a = (1 + z_\mathrm{obs})^{-1}$.
With the conservation of galaxy number as our guiding constraint, the next step is to determine how the trajectories of photons are altered by perturbations to the background geometry. These null geodesics form the fundamental channels which convey information about both redshift and positional distortions. Thus, solving the perturbed photon geodesic equation is the next key step.

3. **Using the Geodesic Vector:**
Now, we want to derive the form of the coordinate shift $\Delta x^\mu(x)$. We begin by writing

$$x_\mathrm{r}^\mu = x^\mu(x_\mathrm{r}) + \delta x^\mu(x_\mathrm{r}) \tag{1.34}$$

and writing the physical comoving distance x_r in the arguments of RHS, as a perturbation around redshift space position (computed using background FLRW)

$$x_\mathrm{r}^\mu(x_\mathrm{r}) = x^\mu(x) + \frac{dx^\mu}{dx}\delta x + \delta x^\mu + \delta x^\mu(x)\frac{d\delta x^\mu}{dx^2}. \tag{1.35}$$

Restricting ourselves to the first order, we ignore the $O(\delta^2)$ term in the previous equation. On comparing Eq. (1.25) and Eq. (1.35) , we can identify the form of the coordinate shift

$$\Delta x^\mu = \frac{dx^\mu}{dx}\delta x + \delta x^\mu(x). \tag{1.36}$$

Since the terms mix-up later, it is worth clarifying on the onset that the scalar δx is the radial shift in the affine parameter, the vector δx^μ is the perturbation to the photon's trajectory and Δx^μ is the total coordinate shift (including both the factors). If we ignore the first derivative term and continue with this derivation (akin to assuming that real-space and redshift space positions overlap), we can reconstruct the standard non-relativistic treatment of redshift space distortions, which yields the Kaiser effect. On doing so, however, we blind ourselves to several important and observable effects. Therefore, we will keep both the terms.
We defined our d/dx operator (Eq. (1.31)) towards the end of Step 1 and if we apply it to our redshift space coordinate x^μ (Eq.), we easily get the geodesic vector in redshift space

$$k^\mu = \frac{dx^\mu}{dx} = (-1, \boldsymbol{n}) \tag{1.37}$$

which implies

$$\Delta x^0(x) = -\delta x + \delta x^0(x) \tag{1.38}$$

$$\Delta x^{\mathrm{i}}(x) = n^{\mathrm{i}}\delta x + \delta x^{\mathrm{i}}(x). \tag{1.39}$$

To get the real-space geodesic vector k_{r}^{μ}, we can use Eq. (1.34) as follows

$$k_{\mathrm{r}}^{\mu} \equiv \frac{dx_{\mathrm{r}}^{\mu}}{dx} = \frac{d}{dx}(x^{\mu} + \delta x^{\mu}) = (-1 + \delta f, n^{\mathrm{i}} + \delta n^{\mathrm{i}}) \tag{1.40}$$

where we have defined the frequency and spatial shift as

$$\delta f \equiv \frac{d\delta x^0}{dx} \tag{1.41}$$

$$\delta n^{\mathrm{i}} \equiv \frac{d\delta x^{\mathrm{i}}}{dx} \tag{1.42}$$

Now, that the various shifts for the different quantities have been defined in both real and redshift space, we can move ahead with trying to systematically solve for them.

4. **Redshift (and Scale Factor) Perturbation:**
   To derive Δx^0 from the previous step, we will relate the scale factors between real and redshift space. We can expanding the argument of $a_{\mathrm{r}}(x_{\mathrm{r}}^0)$ in terms of x^0 and some linear order perturbation Δx^0(similar to what we did with $x_{\mathrm{r}}^{\mu}(x_{\mathrm{r}})$ earlier),

$$a_{\mathrm{r}}\left(x_{\mathrm{r}}^0\right)) = \left(x^0 + \Delta x^0\right) \tag{1.43}$$

$$= a\left(x^0\right) + \frac{\partial a}{\partial x^0}\Delta x^0 a\left(x^0\right)\left[1 + \frac{1}{a(x^0)}\frac{\partial a}{\partial x^0}\Delta x^0\right] \tag{1.44}$$

$$= a\left(x^0\right)\left[1 + \mathcal{H}\Delta x^0\right], \tag{1.45}$$

where we defined

$$\mathcal{H} \equiv \frac{1}{a\left(x^0\right)}\frac{\partial a}{\partial x^0} = aH. \tag{1.46}$$

We can read the fractional change in scale factor across real and redshift space from Eq. (1.45) as

$$\delta \ln a = \frac{a_{\mathrm{r}}}{a} - 1 = \mathcal{H}\Delta x^0. \tag{1.47}$$

To compute $\delta \ln a$ (and subsequently Δx^0), we use the standard definition of observed redshift described by Synge in 1960 (Synge, 1960; Schmidt and Jeong, 2012; Jeong, Schmidt and Hirata, 2012)

$$(1 + z_{\mathrm{obs}}) \equiv (1 + z) = \frac{\left(g_{\mu\alpha}u_{\mathrm{r}}^{\mu}p_{\mathrm{r}}^{\alpha}\right)|_{\mathrm{e}}}{\left(g_{\mu\alpha}u_{\mathrm{r}}^{\mu}p_{\mathrm{r}}^{\alpha}\right)|_{\mathrm{o}}} \tag{1.48}$$

where p^{μ} is the four-momentum, u^{α} is the four-velocity and subscripts denote evaluation at the emission and observation frames. The photon four-momentum has the usual expression

$$p_{\mathrm{r}}^{\mu} = \frac{f\left(a_{\mathrm{r}}\right)}{a_{\mathrm{r}}} k_{\mathrm{r}}^{\mu} \tag{1.49}$$

with $f(a)$ being the photon frequency at scale factor a. To solve the inner products, we will make use of the perturbed spacetime metric written in terms of dimensionless Bardeen potentials because the `LIGER` code (see §2.2.2) implements the conformal Newtonian gauge

$$ds^2 = a_{\mathrm{r}}^2(\eta)\left[-c^2(1+2\psi)\,d\eta^2 + (1-2\phi)\,\delta_{\mathrm{ij}}^{K}\,dx_{\mathrm{r}}^{\mathrm{i}}\,dx_{\mathrm{r}}^{\mathrm{j}}\right]. \tag{1.50}$$

Using Eqs. (1.24), (1.34), (1.48) and (1.49), and keeping only terms in linear order, some algebraic manipulations eventually yield

$$1 + \delta \ln a = \frac{1 + \psi_{\mathrm{e}} + \delta f_{\mathrm{e}} + v_{\|,\mathrm{e}}/c}{1 + \psi_{\mathrm{o}} + \delta f_{\mathrm{o}} + v_{\|,\mathrm{o}}/c}. \tag{1.51}$$

In order to find the perturbation to scale factor completely in terms of variables accessible to us in a (mock or real) survey, we will need to explicitly compute δf. We will do so by integrating the geodesic equation in real-space (Bertacca, 2015)

$$\frac{dk_{\mathrm{r}}^{\mu}}{dx} + \left(\Gamma_{\alpha\beta}^{\mu} + \delta x_{\mathrm{r}}^{\gamma}\frac{\partial\Gamma_{\alpha\beta}^{\mu}}{\delta x^{\gamma}}\right) k_{\mathrm{r}}^{\alpha} k_{\mathrm{r}}^{\beta} = 0 \tag{1.52}$$

where $\Gamma_{\alpha\beta}^{\mu}$ corresponds to the Levi-Civita connection of the metric defined in Eq. (1.50). By solving the time components, we get

$$\delta f = -[\psi_{\mathrm{o}} - v_{\|,\mathrm{o}}/c] + 2\psi + \int_0^x \frac{(\phi' + \psi')}{c} d\tilde{x}, \tag{1.53}$$

which can be further fed into Eq. (1.51) to get our first result worthy of a box

$$\boxed{\delta \ln a = \left[\frac{v_{\|,\mathrm{e}} - v_{\|,\mathrm{o}}}{c} - (\psi_{\mathrm{e}} - \psi_{\mathrm{o}}) - \int_0^x \frac{(\phi' + \psi')}{c} d\tilde{x}\right]}. \tag{1.54}$$

This expression of scale factor perturbation includes, in addition to the classic Doppler term, contributions from the local potential wells and the gravitational influences encountered along the path of the photon.

5. **Coordinate Map:**
Solving the time-component of the geodesic equation has given us δf but we still do not have all the pieces to compute the coordinate shifts Δx^{μ}. Thus, we also solve the spatial part of the geodesic equation to get

$$\delta n^{\mathrm{i}} = -v_{\mathrm{o}}^{\mathrm{i}} - n^{\mathrm{i}}\phi_{\mathrm{o}} - \int^x \partial_{\tilde{x}}(\psi + \phi) d\tilde{x}, \tag{1.55}$$

where we have introduced $\partial_{\tilde{x}=\partial/\partial_{\tilde{x}}}$. From the definitions of δf and δn^{i} in Eq. (1.42), we can see that integrating them will give us

$$\delta x^0 = -x\left[\psi_{\mathrm{o}} - v_{\parallel\mathrm{o}}/c\right] + \int_0^x \left[2\psi + (x-\tilde{x})\frac{(\phi' + \psi')}{c}\right] d\tilde{x}, \tag{1.56}$$

$$\begin{aligned} \delta x^{\mathrm{i}} = {} & n^{\mathrm{i}} x\left[\psi_{\mathrm{o}} - v_{\parallel\mathrm{o}}/c\right] - x v^{\mathrm{i}}_{\perp\mathrm{o}}/c \\ & - \int_0^x n^{\mathrm{i}}\left[(\psi - \phi) + (x-\tilde{x})\frac{(\phi' + \psi')}{c}\right] d\tilde{x} \\ & - \int_0^x (x-\tilde{x})\left[\partial^{\mathrm{i}}_{\tilde{x}} - n^{\mathrm{i}}(n_{\mathrm{j}}\partial^{\mathrm{j}}_{\tilde{x}})\right](\psi + \phi) d\tilde{x}. \end{aligned} \tag{1.57}$$

Combining δx^0, Δx^0 and $\Delta \ln a$, we can assemble

$$\begin{aligned} \delta x = {} & -\left(x + \frac{1}{\mathcal{H}}\right)\left[\psi_{\mathrm{o}} - v_{\parallel\mathrm{o}}/c\right] + \frac{1}{\mathcal{H}}\left[\psi_{\mathrm{e}} - v_{\parallel\mathrm{e}}/c\right] \\ & + \int_0^x \left[2\psi + (x-\tilde{x})\frac{(\phi' + \psi')}{c}\right] d\tilde{x} + \frac{1}{\mathcal{H}}\int_0^x \frac{(\phi' + \psi')}{c} d\tilde{x}. \end{aligned} \tag{1.58}$$

Finally, we have all the pieces to summarize the coordinate map demanded in Eq. (1.25), which now includes not only the Doppler effects along LOS but also the deflections in the sky position caused by gravitational lensing

$$\boxed{\Delta x^0 = \frac{c}{\mathcal{H}}\delta \ln a} \tag{1.59}$$

$$\boxed{\begin{aligned} \Delta x^{\mathrm{i}} = {} & -n^{\mathrm{i}} x\left(\phi_{\mathrm{o}} + \psi_{\mathrm{o}} + \frac{v_{\parallel\mathrm{e}}}{c}\right) - x\frac{v^{\mathrm{i}}_{\mathrm{o}}}{c} - \frac{c}{\mathcal{H}} n^{\mathrm{i}}\delta \ln a \\ & + n^{\mathrm{i}}\int_0^x (x-\tilde{x})\frac{\psi' + \phi'}{c}\, d\tilde{x} - \int_0^x (x-\tilde{x})\,\delta^{\mathrm{i}}_{\mathrm{j}}\tilde{\partial}^{\mathrm{j}}(\psi + \phi)\, d\tilde{x} \\ & + 2n^{\mathrm{i}}\int_0^x (\psi + \phi)\, d\tilde{x} \end{aligned}}\, . \tag{1.60}$$

With these boxed expressions, we have managed to derive first of the three main pieces described in the beginning of the schematic layout. Note, that our main aim is to not only transform coordinates between real and redshift space, but to transform the catalog into an overdensity map in the redshift space. This requires further corrections due to volume distortions and transformations in the survey functions. Thus, we will now focus our attention on these two remaining pieces.

6. **Volume Distortion**
To transform the real-space volume element to the observed redshift space volume element, we

start with the following relation (Yoo, 2010; Schmidt and Jeong, 2012)

$$\mathrm{d}\mathcal{V}_{\mathrm{r}} = \left(\frac{\sqrt{-g\left(x_{\mathrm{r}}^{\mu}\right)}}{a_{\mathrm{r}}^{4}} \right) \epsilon_{\mu\nu\gamma\rho} \frac{u_{\mathrm{r}}^{\mu}}{a_{\mathrm{r}}} \frac{\partial x_{\mathrm{r}}^{\nu}}{\partial x^{1}} \frac{\partial x_{\mathrm{r}}^{\gamma}}{\partial x^{2}} \frac{\partial x_{\mathrm{r}}^{\rho}}{\partial x^{3}} \mathrm{d}\mathcal{V} \,. \tag{1.61}$$

In order to compute the linear order contributions from the volume transformation, we use the following perturbative expansion for the determinant B of a rank to tensor $\mathbb{B}$

$$B = B^{(0)} + B^{(1)}\mathrm{Tr}\left[\mathbb{B}^{(0)-1}\mathbb{B}^{(1)}\right] + \mathcal{O}(2), \tag{1.62}$$

where the parenthesis denote the order of the perturbation and Tr represents the trace. Applying this relation to the first term in Eq. (1.61) gives

$$\frac{\sqrt{-g\left(x_{\mathrm{r}}^{\mu}\right)}}{a_{\mathrm{r}}^{4}} = 1 + \frac{g_{\mu}^{\mu}(x^{\mu})}{a_{\mathrm{r}}^{2}}. \tag{1.63}$$

Similarly, the remaining parts can be expanded and simplified. The final result is provided by Bertacca (2015)

$$1 + \Delta V = \epsilon_{\mu\nu\gamma\rho} \frac{u_{\mathrm{r}}^{\mu}}{a_{\mathrm{r}}} \frac{\partial x_{\mathrm{r}}^{\nu}}{\partial x^{1}} \frac{\partial x_{\mathrm{r}}^{\gamma}}{\partial x^{2}} \frac{\partial x_{\mathrm{r}}^{\rho}}{\partial x^{3}} = 1 + \frac{u_{\mathrm{r}}^{0} + n_{\mathrm{i}} u_{\mathrm{r}}^{\mathrm{i}}}{c\,a} + \left(\frac{2}{x} + \partial_{\|}\right)\Delta x_{\|} - 2\kappa \,, \tag{1.64}$$

where we have use the standard definition of the gravitational weak-lensing convergence (Prat and Bacon, 2025)

$$\kappa = \frac{-1}{2}\partial_{\perp,\mathrm{i}}\,\Delta x_{\perp}^{\mathrm{i}} = \frac{1}{2}\int_{0}^{x}(x-\tilde{x})\,\frac{\tilde{x}}{x}\,\nabla_{\perp}^{2}(\psi+\phi)d\tilde{x} - v_{\perp,\mathrm{o}}. \tag{1.65}$$

We now have the relevant transformations for coordinates and volume elements. To invoke the fundamental identity expressed in Step 2, the final remaining object of interest is the galaxy number density itself.

7. **Galaxy Number Density:**
One particularly succinct way of writing an expression for galaxy number density in redshift space is to organize the equation in terms of an average number density $\bar{n}_{\mathrm{g}} \equiv n_{\mathrm{g}}(x^{0}, F)$, an evolution bias $\mathcal{E}$ and magnification bias $\mathcal{Q}$. To assemble these terms, it is helpful to first introduce Magnification $\mathcal{M}$, which is another important general relativistic effect that changes the observed flux F in cosmological surveys

$$\mathcal{M} = \frac{F_{\mathrm{r}}}{F} = \frac{1}{D_{\mathrm{L,r}}^{2}} D_{\mathrm{L}}^{2} = \left(\frac{D_{\mathrm{L,r}}^{2}}{D_{\mathrm{L}}^{2}}\right)^{-2}, \tag{1.66}$$

where $D_{L,r}$ and D_{L} are luminosity distances in real and redshift space respectively. Using the cosmic rulers prescription again, we can invert this relationship to write (Bertacca, 2015)

$$\mathcal{M}^{-1} = \frac{\sqrt{-g\left(x_{\mathrm{r}}^{\alpha}\right)}}{\left(u_{\mathrm{r},\rho}\, \mathrm{d}x_{\mathrm{r}}^{\rho}\left(x_{\mathrm{r}}\right)/\mathrm{d}x\right) a^{2}} \epsilon_{\mu\nu\rho\sigma}\, u^{\mu} \frac{\mathrm{d}x_{\mathrm{r}}^{\nu}\left(x_{\mathrm{r}}\right)}{\mathrm{d}x} \frac{\partial x_{\mathrm{r}}^{\rho}}{\partial x^{j}} \frac{\partial x_{\mathrm{r}}^{\sigma}}{\partial x^{k}} \alpha^{j} \beta^{k}, \tag{1.67}$$

where $\{\alpha^{\mathrm{i}}, n^{\mathrm{i}}, \beta^{\mathrm{i}}\}$ form a three dimensional orthonormal basis. On expanding this expression to linear order,

$$\begin{aligned} \mathcal{M}^{-1} =& 1 + \frac{1}{2a_{\mathrm{r}}^{2}} g_{\mu}^{\mu} + \frac{u_{\mathrm{r}}^{0} + n_{i} u_{\mathrm{r}}^{i} + g_{\mu 0} u_{\mathrm{r}}^{\mu} - n^{i} g_{\mu i} u_{\mathrm{r}}^{\mu}}{c} \\ &+ 2\delta \ln a + \partial_{x}\left(\Delta x^{0} + \Delta x_{\parallel}\right) + \frac{2}{x}\Delta x_{\parallel} - 2\kappa \end{aligned} \tag{1.68}$$

We can rewrite this result as

$$\begin{aligned} \mathcal{M} =& 1 + \Delta\mathcal{M} = 1 - \frac{1}{2a_{\mathrm{r}}^{2}} g_{\mu}^{\mu} - \frac{u_{\mathrm{r}}^{0} + n_{i} u_{\mathrm{r}}^{i} + g_{\mu} u_{\mathrm{r}}^{\mu} - n^{i} g_{\mu i} u_{\mathrm{r}}^{\mu}}{c} \\ &- 2\delta \ln a - \partial_{x}\left(\Delta x^{0} + n_{i}\Delta x^{i}\right) - \frac{2}{x} n_{i}\Delta x^{i} + 2\kappa \end{aligned} \tag{1.69}$$

We have already computed n^{i}, Δx^{μ}, $\delta \ln a$ and κ in the previous steps. Now, we can simply substitute all those quantities and write the magnification in conformal Newtonian gauge as

$$\mathcal{M} = 1 + 2\kappa + 2\psi_{\mathrm{e}} - 2v_{\parallel \mathrm{o}}/c - 2\left(1 - \frac{c}{\mathcal{H}x}\right)\delta \ln a - \frac{2}{x}\int_{0}^{x} (\psi + \phi)\mathrm{d}\tilde{x}. \tag{1.70}$$

The integrand to compute the total galaxy number as mentioned in Eq. (1.32) was $a_{\mathrm{r}}^{3}\,(x_{\mathrm{r}}^{0})\, n_{\mathrm{g}}(x_{\mathrm{r}}^{\mu}, F_{\mathrm{r}})$. The scale factor term can be easily linearized

$$\left(\frac{a_{\mathrm{r}}}{a}\right)^{3} = 1 + 3\,\delta \ln a. \tag{1.71}$$

For the number density term, we can expand as follows

$$\begin{aligned} n_{\mathrm{g}}\left(x_{\mathrm{r}}^{\mu}, F_{\mathrm{r}}\right) &= n_{\mathrm{g}}\left(x^{\mu} + \Delta x^{\mu}, F + F\Delta\mathcal{M}\right) \\ &= n_{\mathrm{g}}\left(x^{\mu}, F\right) + \frac{\partial n_{\mathrm{g}}\left(x^{0}, F\right)}{\partial F} F\Delta\mathcal{M} + \frac{\partial\, n_{\mathrm{g}}\left(x^{0}, F\right)}{\partial x^{0}} \Delta x^{0} \end{aligned} \tag{1.72}$$

or, alternatively, we can re-parametrize the arguments and express this result in terms of luminosity

$$n_{\mathrm{g}}\left(x_{\mathrm{r}}^{\mu}, F_{\mathrm{r}}\right) = n_{\mathrm{g}}\left(x^{\mu}, L_{\mathrm{min}}\right) - \frac{\partial\, n_{\mathrm{g}}\left(x^{0}, L_{\mathrm{min}}\right)}{\partial \ln L_{\mathrm{min}}} \Delta\mathcal{M} + \frac{\partial\, n_{\mathrm{g}}\left(x^{0}, L_{\mathrm{min}}\right)}{\partial x^{0}} \Delta x^{0}. \tag{1.73}$$

Now, we will define two biases which make the interpretation of the derivative terms easier. We begin with

$$\left.\frac{\partial \bar{n}_{\mathrm{g}}}{\partial \bar{x}^{0}}\right|_{\bar{L}=4\pi D^{2}F} = \mathcal{H}\left.\frac{\partial \bar{n}_{\mathrm{g}}}{\partial \ln \bar{a}}\right|_{\bar{L}} = -\mathcal{H}\left.\frac{\partial \ln \bar{n}_{\mathrm{g}}}{\partial \ln(1+z)}\right|_{L_{\mathrm{min}}=L_{\mathrm{lim}}(z)} = -\mathcal{H}\mathcal{E}, \tag{1.74}$$

and define an evolution bias

$$\mathcal{E}(z) \equiv -\left.\frac{\partial \bar{n}_{\mathrm{g}}}{\partial \ln(1+z)}\right|_{L_{min}=L_{\mathrm{lim}}(z)} \tag{1.75}$$

which captures the change in galaxy population due to redshift evolution. Similarly, we define another bias parameter

$$Q(z) = -\left.\frac{\partial \ \ln \bar{n}_{\mathrm{g}}}{\partial \ \ln L_{\mathrm{min}}}\right|_{L_{min}=L_{\mathrm{lim}}(z)} \tag{1.76}$$

which represents the changes in galaxy population due to change in (de)magnification. With these bias terms, we can rewrite Eq. (1.73) in a condensed manner as (Borzyszkowski, Bertacca and Porciani, 2017; Elkhashab, Porciani and Bertacca, 2021)

$$\boxed{n_{\mathrm{g}}\left(x_{\mathrm{r}}^{\mu}, F_{\mathrm{r}}\right) = \bar{n}_{\mathrm{g}}[1+\delta_{\mathrm{g}}+\mathcal{E}\,\delta \ln a - Q(\mathcal{M}-1)]} \tag{1.77}$$

1.3.3 Assembling Redshift Space Overdensity

We now have all the terms and relations to perform the last move of our derivation i.e. assembling an expression that maps a real-space catalog to the redshift space overdensity field $\delta_{g,s}$ including all the linear order relativistic effects. By definition, the density contrast can be written as

$$\delta_{g,s} = \frac{n_{\mathrm{g}}(x^{0},F) - \bar{n}_{\mathrm{g}}(x^{0},F)}{n_{\mathrm{g}}(x^{0},F)} \tag{1.78}$$

which we can expand using our previous results into

$$\begin{aligned}
\delta_{\mathrm{g,\,s}}(\boldsymbol{x}) = \delta_{\mathrm{g}} &- \frac{1}{\mathcal{H}}\frac{\partial\left(\boldsymbol{v}_{\mathrm{e}}\cdot\boldsymbol{n}\right)}{\partial x} + 2(1-Q)\kappa + \frac{2(1-Q)}{x}\int_{0}^{x}(\psi+\phi)\mathrm{d}\tilde{x} \\
&+ \left[\mathcal{E} - 2Q - \frac{\mathcal{H}'}{\mathcal{H}^{2}} - \frac{2(1-Q)c}{x\mathcal{H}}\right] \times \left[\frac{\boldsymbol{v}_{\mathrm{e}}}{c}\cdot\boldsymbol{n} - \left(\psi_{\mathrm{e}}-\psi_{\mathrm{o}}\right) - \int_{0}^{x}\frac{\left(\psi'+\phi'\right)}{c}\,\mathrm{d}\tilde{x}\right]. \\
&- 2(1-Q)\psi_{\mathrm{e}} + \phi_{\mathrm{e}} + \frac{\psi_{\mathrm{e}}'}{\mathcal{H}} + \left[2 - \mathcal{E} + \frac{\mathcal{H}'}{\mathcal{H}^{2}} + \frac{2(1-Q)c}{x\mathcal{H}}\right]\frac{\boldsymbol{v}_{\mathrm{o}}}{c}\cdot\boldsymbol{n}
\end{aligned} \tag{1.79}$$

Recall that we performed this calculation in Poisson (conformal Newtonian) gauge and that `LIGER` method uses the synchronous-comoving gauge. In Step 1, we wrote Eq. (1.21) which relates Poisson gauge with SC gauge. Now, we can finally apply this relation to Eq. (1.79) and write (Challinor and

A. Lewis, 2011; Bertacca, 2015)

$$\boxed{\begin{aligned}\delta_{\mathrm{g,\,s}}(\boldsymbol{x}) = b\delta_{\mathrm{SC}} &- \frac{1}{\mathcal{H}}\frac{\partial\left(\boldsymbol{v}_{\mathrm{e}}\cdot\boldsymbol{n}\right)}{\partial x} + 2(1-Q)\kappa \\ &+ \left[\mathcal{E} - 2Q - \frac{\mathcal{H}'}{\mathcal{H}^2} - \frac{2(1-Q)c}{x\mathcal{H}}\right] \\ &\times \left[\frac{\boldsymbol{v}_{\mathrm{e}}}{c}\cdot\boldsymbol{n} - \left(\psi_{\mathrm{e}} - \psi_{\mathrm{o}}\right) - \int_0^x \frac{\left(\psi' + \phi'\right)}{c}\,\mathrm{d}\tilde{x}\right] \\ &- 2(1-Q)\psi_{\mathrm{e}} + \phi_{\mathrm{e}} + \frac{\psi'_{\mathrm{e}}}{\mathcal{H}} + (3-\mathcal{E})\mathcal{H}\Phi_{\mathrm{v}} \\ &+ \frac{2(1-Q)}{x}\int_0^x (\psi + \phi)\mathrm{d}\tilde{x} \\ &+ \left[2 - \mathcal{E} + \frac{\mathcal{H}'}{\mathcal{H}^2} + \frac{2(1-Q)c}{x\mathcal{H}}\right]\frac{\boldsymbol{v}_{\mathrm{o}}}{c}\cdot\boldsymbol{n}\end{aligned}} \tag{1.80}$$

Interpreting Terms and Effects

Let us take a moment to appreciate how many cosmological effects of note we have recovered, without any ad-hoc effort, by giving a relativistic treatment to linear order metric perturbations.

1. **Baseline overdensity** $b\delta_{\mathrm{SC}}$: This term uses the dark-matter overdensity in synchronous comoving gauge and paints galaxy overdensity as per the standard biasing prescription. Incidentally, the idea of galaxies being biased tracers of DM overdensity also goes back to the work of Kaiser (1984) when he was investigating the structure of Abell cluster. The redshift evolution of the bias factor b was first studied systematically by Tegmark and Peebles (1998) and they found that b is generally larger at earlier epochs and at $t \longrightarrow \infty$ limit, galaxies become unbiased tracers of the DM field. Later studies by Mann, Peacock and A. F. Heavens (1998) also established that while the bias is generally scale dependent, it is only weakly correlated and approaches a constant value at large scales.

2. **Kaiser Correction** $\partial\left(\boldsymbol{v}_{\mathrm{e}}.\boldsymbol{n}\right)/\partial x$: This is the classic squashing and stretching along the line of sight. The dot product of emitter velocity and $\boldsymbol{n}$ break parity symmetry and the term captures how segments moving towards LOS contribute to the overdensity differently from the segment that are receding away. This same term appears later in the Doppler correction as well. Due to this effect, large scale overdensities with coherent inflows appear flattened like pancakes and smaller virialized structures with random velocity dispersion become elongated (as in 'Fingers-of-God'). Also, given that the in-fall velocities are sensitive to the growth rate $f(z)$, the quadrupole in LSS can give constraints on $f\sigma_8$ combination.

3. **Weak Lensing Convergence** $2(1-Q)\kappa$: Weak gravitational lensing (Prat and Bacon, 2025; Davies, Cautun and Li, 2018) slightly deflects null geodesics such that a bundle that subtends solid angle $\mathrm{d}\Omega$ at the source arrives at the telescope with $\mathrm{d}\Omega \longrightarrow (1+2\kappa)\,\mathrm{d}\Omega$. The convergence scalar[13] κ, when positive, acts like a magnifying glass. In linear theory κ is a line-of-sight

---

[13] An elementary discussion on κ kernel and its relation to the Jacobi matrix is presented in (Prat and Bacon, 2025))

integral of the Weyl potential

$$\Psi_W \equiv \frac{\psi + \phi}{2},$$

which is the gauge-invariant combination of the Newtonian potential ψ and the curvature potential ϕ. Because photons are null geodesics they only feel $\psi + \phi$, so measuring κ directly tests the relativistic Poisson equation and any modified-gravity slip between ψ and ϕ (Grimm, Bonvin and Tutusaus, 2024).

4. **Sachs-Wolfe Effect** $(\psi_\mathrm{e} - \psi_\mathrm{o})$: This term corresponds to the 'standard' Sachs-Wolfe effect (Sachs and Wolfe, 1967), caused by the difference in the local potentials around the source and the observer, which can endow or steal additional energy from the photons via gravitational redshift.

5. **Integrated Sachs-Wolfe** $-\int_0^x (\psi' + \phi')/c \, \mathrm{d}\tilde{x}$: A photon climbing in and out of a static potential well loses the same energy it gains and its redshift is unchanged. But if the potential itself evolves while the photon is in flight (because cosmic expansion makes the gravitational wells decay), then the departure and arrival energies no longer cancel. The line-of-sight integral of the time derivatives of Newtonian and curvature potentials, ψ' and ϕ', quantifies that net energy shift and therefore perturbs the inferred radial position of luminous sources. This is particularly noticeable in the temperature maps of the Cosmic Microwave background at large scales (Nishizawa, 2014).

6. **Source Potential Lensing** $-2(1 - Q)\psi_\mathrm{e}$: This term captures the magnification bias induced by the local gravitational well around the source of the emission.

7. **Gauge Shift** $(3 - \mathcal{E})\mathcal{H}\Phi_v$: This arises due to the mapping between SC and Poisson gauge (Borzyszkowski, Bertacca and Porciani, 2017).

8. **Shapiro (gravitational) time delay** $\int_0^x (\psi + \phi) \, \mathrm{d}\tilde{x}$: Every potential well or hill that a photon traverses slows or speeds its clock relative to an unperturbed light path (the same effect Shapiro (1964) proposed to test GR with radar echoes). The accumulated delay shifts the photon's emission conformal time, and hence the inferred radial position of the source, by an amount proportional to the line-of-sight integral of the Weyl potential $(\psi + \phi)$.

9. **Observer Velocity Term** $(\boldsymbol{v}_\mathrm{o}.\boldsymbol{n}/c)$: This term and the various functions in the preceding parenthesis capture the subtle effects of observer velocity on the overdensity maps in redshift space (Elkhashab, Porciani and Bertacca, 2024). In §1.4, we will isolate this effect and in the later chapters of this dissertation, subject it to various forms of statistical scrutiny.

Limiting Behavior

To estimate when these relativistic effects are relevant, we begin by noticing that they are mostly of the order of the Bardeen potentials ($\sim \phi, \psi$). Further, in ΛCDM, at linear order, these Bardeen potentials are identical to source potential φ/c^2 of the Poisson equation (Eq. (1.12)). Thus, we can assume the Bardeen potentials to be of the same order as φ in perturbed cosmology and identify at which scales φ

is comparable to real-space overdensity δ. On taking the Fourier transform of Eq. (1.12), we can write

$$k^2\tilde{\varphi}(\boldsymbol{k}) = -\frac{3H_0^2\Omega_\mathrm{m}}{2a}\tilde{\delta}(\boldsymbol{k}) \tag{1.81}$$

This can be rewritten using a physical scale $\lambda_p = a/k$ and the Hubble radius $\lambda_H = 1/H$ as

$$\tilde{\varphi}(\boldsymbol{k}) \approx -\left(\frac{\lambda_\mathrm{p}}{\lambda_\mathrm{H}}\right)^2 \tilde{\delta}(\boldsymbol{k}). \tag{1.82}$$

This expression tells us that the gravitational potential is damped by an amplitude factor of $(\lambda_p/\lambda_H)^2$ i.e. the effects which are comparable in their magnitude to φ become negligible for $\lambda_p \ll \lambda_H$. It is only when the physical scales that we are probing are comparable to the Hubble radius (i.e. the largest modes of the large scale structure), that these relativistic effects manifest themselves. Few of our current generation surveys can map some of these large scales modes and, consequently, the relativistic effects can in principle be detected in our data (Elkhashab, Porciani and Bertacca, 2021).

If we consider the sub-Hubble limit where the factors dependent on the Bardeen potentials can be ignored and we assume that light rays travel in Euclidean straight lines as opposed to null-geodesics which curve around massive objects (i.e. ignoring lensing), then the classical Kaiser effect can be recovered as follows. We start with denoting the redshift space coordinates as $\boldsymbol{x}$ and real-space coordinates $\boldsymbol{x}_\mathrm{r}$, the peculiar velocity $\boldsymbol{v}$ (in units of Hubble constant) comes into the coordinate map as

$$\boldsymbol{x} = \boldsymbol{x}_\mathrm{r}\left(1 + \frac{u(\boldsymbol{x}_\mathbf{r})}{x_\mathrm{r}}\right). \tag{1.83}$$

where we define $u \equiv \boldsymbol{v}_\mathrm{e}.\boldsymbol{n}$. Assuming the object is very distant $kx_\mathrm{r} \gg 1$, the Jacobian between the two coordinates can be written as

$$d^3\boldsymbol{x} = \left(1 + \frac{du}{dx_\mathrm{r}}\right) d^3\boldsymbol{x}_\mathrm{r} \tag{1.84}$$

where we have kept terms only to linear order in u/x_r (notice the similarity to the Kaiser term's appearance in Eq. (1.80) explained in the previous subsection). As in our primary derivation, we invoke number density conservation $\delta d^3\boldsymbol{x} = \delta_\mathrm{r} d^3\boldsymbol{x}_\mathrm{r}$ for plane-wave perturbation δ. From linear theory (Peebles, 2020), we have $\dot{\delta} = -ikv$. Now, if we define $\mu = \hat{\boldsymbol{x}}_\mathrm{r}.\hat{k}$ and $f(\Omega) \equiv d\ln\delta/d\ln a \approx \Omega^{0.6}$, then we can write

$$\begin{aligned}\frac{du}{d\mathrm{x}_\mathrm{r}} &= \mu\frac{d}{d\mathrm{x}}v \\ &= \mu(ik\mu)v \\ &= -\mu^2(-ikv) \\ &= -\mu^2 f(\Omega)\delta\end{aligned} \tag{1.85}$$

because $\dot{\delta} = f(\Omega)\delta$ in units where $H = 1$. Putting this together, we finally get the relationship between real and redshift space DM overdensities as

$$\delta_s = \delta\left(1 + f\mu^2\right). \tag{1.86}$$

This dark matter overdensity can be related to the galaxy fluctuation in our idealized limit using linear bias as

$$\delta_{g,s} = b\left(1 + f\mu^2\right)\delta. \tag{1.87}$$

The μ-dependence of the over-density (and, consequently, the correlation function) can be expanded out in Legendre polynomials. We will discuss in much greater detail when we talk of the multipoles expansion for the power spectrum in §2.1.1. For now, it suffices to notice that the redshift space overdensity field acquired via the classical Kaiser derivation has a mismatch of several terms when compared against the full general relativistic treatment. In the following section, we describe how this mismatch can be used to isolate the FOTO signal.

1.4 Isolating Finger-of-the-Observer Effect

With the general theoretical formalism in place, we can now easily isolate the FOTO signal and remark on some of its features. In this section, we restrict ourselves to the FOTO model and save the detailed discussion on the estimators to extract FOTO signal from catalogs for §3.1. We begin by grouping all the terms independent of observer velocity into one function and rewriting Eq. (1.80) as

$$\delta_{g,s}(\boldsymbol{x}) = \delta_{\mathrm{com}}(\boldsymbol{x}) + \frac{\alpha_{\mathrm{o}}(x)}{x}\frac{\boldsymbol{v}_{\mathrm{o}}.\hat{\boldsymbol{x}}}{aH} \tag{1.88}$$

where δ_{com} contains all the terms independent of v_{o} and

$$\alpha_{\mathrm{o}}(x) \equiv 2(1-Q) - \frac{xH}{c(1+z)}\mathcal{E} + \frac{xH}{c(1+z)}\left[3 - \frac{1+z}{H}\frac{\mathrm{d}H}{\mathrm{d}z}\right] \tag{1.89}$$

If we repeat the same exercise in the classical Kaiser regime (including the full-volume Jacobian, which leads to a magnification bias, but for vanishing Bardeen potentials $\phi = \psi = 0$), we find that we arrive at an expression similar to Eq. (1.88)

$$\delta^{\mathrm{c}}_{\mathrm{g,\,s}}(\boldsymbol{x}) = \delta^{\mathrm{c}}_{\mathrm{com}}(\boldsymbol{x}) + \frac{\alpha_{\mathrm{c}}(x)}{x}\frac{\boldsymbol{v}_{\mathrm{o}}\cdot\hat{\boldsymbol{x}}}{aH}, \tag{1.90}$$

where the c denotes an inclusion of only non-relativistic classical corrections. The primary difference is encoded in the distinction between $\alpha_{\mathrm{o}}(x)$ and

$$\alpha_{\mathrm{c}}(x) \equiv \frac{\mathrm{d}\ln x^2\bar{n}_{\mathrm{g,\,s}}(x)}{\mathrm{d}\ln x} + \frac{Hx}{c(1+z)}\left[1 - \frac{\mathrm{d}\ln H}{\mathrm{d}\ln(1+z)}\right]. \tag{1.91}$$

To compare the two functions more easily, we can rewrite the derivative as

$$\begin{aligned}\frac{\mathrm{d}\ln x^2\bar{n}_{\mathrm{g,\,s}}(x)}{\mathrm{d}\ln x} &= 2 + \frac{\mathrm{d}\ln\bar{n}_{\mathrm{g,\,s}}(x)}{\mathrm{d}\ln x}\\ &= 2 + \left.\frac{\partial\ln\bar{n}_{\mathrm{g}}}{\partial\ln L_{\mathrm{min}}}\right|_{L_{\mathrm{min}}=L_{\mathrm{lim}}(z)}\frac{\mathrm{d}\ln L_{\mathrm{lim}}}{\mathrm{d}\ln x} + \frac{\partial\ln\bar{n}_{\mathrm{g}}}{\partial\ln x},\end{aligned} \tag{1.92}$$

and using the definition of magnification and evolution bias,

$$\begin{aligned}\frac{\mathrm{d}\ln x^2\bar{n}_{\mathrm{g,\,s}}(x)}{\mathrm{d}\ln x} &= 2 - Q\frac{\mathrm{d}\ln L_{\mathrm{lim}}}{\mathrm{d}\ln x} + \frac{\partial\ln\bar{n}_{\mathrm{g}}}{\partial\ln(1+z)}\frac{\mathrm{d}\ln(1+z)}{\mathrm{d}\ln x}\\ &= 2 - Q\frac{\mathrm{d}\ln L_{\mathrm{lim}}}{\mathrm{d}\ln x} - \mathcal{E}\frac{Hx}{c(1+z)}\\ &= 2(1-Q) - (2Q+\mathcal{E})\frac{Hx}{c(1+z)}.\end{aligned} \tag{1.93}$$

On substituting this relation back into the definition of α_{c}, we can rewrite

$$\alpha_{\mathrm{c}}(x) = 2(1-Q) - \frac{Hx}{c(1+z)}\left[2Q + \mathcal{E} + 1 - \frac{\mathrm{d}\ln H}{\mathrm{d}\ln(1+z)}\right] \tag{1.94}$$

which differs from the relativistic treatment by

$$\Delta\alpha \equiv \alpha_c - \alpha_{\mathrm{o}} = \frac{-2rH}{c(1+z)}(Q+1) \tag{1.95}$$

This difference between the two treatments serves as the key to measuring observer velocity (or cosmological parameters) using relativistic effects on the large scale structure. Later chapters in this thesis are dedicated to exploiting the difference $\Delta\alpha$ from Eq. (1.95). In Chapter 2, we will focus on the computational aspect of the FOTO signal by introducing the statistical estimators essential for our analysis and describing the `LIGER` method in greater detail. In Chapter 3, we will present our main results on peculiar velocity constraints using FOTO effect and discuss the role of higher multipoles.

CHAPTER 2

Methods

The ‘uniqueness of the universe’, in philosophy of cosmology literature (Ellis, 2006; Ellis, 2014; Curiel, 2015), refers to a fundamental difficulty in doing cosmological research scientifically i.e. our strictly limited access to only one instantiation of possible universes, ours. We must confront the fact that our cosmological theories have a single referent, constituting a total sample size of $N = 1$. Yet, in an era shaped by the successes of ΛCDM and the astonishing precision of modern observations, it is easy to forget that, even into the 1960s, cosmology was widely considered as a branch of philosophy (Munitz, 1962; Longair, 2006; Kragh, 1999). The theoretical elegance of general relativistic models and the sensitivity of observations deserve immense credit for transforming abstract speculations about the universe into scientifically admissible claims. However, alongside these triumphs lies a less celebrated but equally essential development and that is the adoption of appropriate statistical tools capable of connecting cosmological predictions with observations. In §2.1, we will discuss these statistical tools, focusing on relativistic effects on the 1D matter power spectrum. Specifically, we develop the statistical interface that connects the perturbative treatment of general relativistic RSD (from §1.3) to Stage-IV cosmological surveys (discussed later in §3).

Another scientific domain, that of the study of living beings, grapples with a similar uniqueness problem. We are confined to studying a single evolutionary tree, branching from the only known seed of life (Blount, Lenski and Losos, 2018). This restriction mirrors the epistemological challenge faced in cosmology and, hence, the opening lines of Peebles’ chapter on n-point correlation functions (Peebles, 2020) are particularly striking:

> Two general approaches to the empirical study of the large-scale matter distribution might be called the botanical and the statistical. Reduction of phenomena to specific sorts of objects like galaxies and Abell clusters of galaxies is direct and certainly has proved profitable. But [...] the general distribution is so complicated, and the data we hope to get so schematic, that a full reduction to genera or species might not be profitable or even possible.

The statistical approach to the empirical study of the large-scale matter distribution relies on a central methodological pillar that Edwin Hubble called the ‘Fair Sample’ assumption (Hubble, 1937; Buchert and Martinez, 1993; Coles, 2002). It involves assuming the following three premises (Peebles, 2020).

1. Well separated parts of the universe can be treated as independent realizations of the same physical process.
2. There are many independent observable lumps of the universe that can be aggregated to approximate a statistical ensemble.
3. The statistical properties of this ensemble are invariant under rotations.

Given the detailed discussion of cosmic anisotropies in §1.3, one might naturally expect that our focus lies on effects that apparently violate the third premise. This anisotropic complication motivates a decomposition of observed statistics into a sum over various multipoles. For the Finger-of-the-Observer (FOTO) effect, the leading (monopole) contribution has been studied in detail by Elkhashab, Porciani and Bertacca (2024). However, as the title of this thesis suggests, our focus is on investigating the higher-order multipoles of the FOTO signal.

2.1 Two-Point Statistics

Historically, the clustering of large-scale structure has been commonly analyzed using variants of the autocorrelation function (Zwicky, 1953; Limber, 1953; Neyman, Scott and Shane, 1956). Its sustained popularity owes partly to the fact that its redshift dependence is theoretically well established and partly to the ease with which it can be scaled to analyze massive datasets (more about this in §2.1.4). Despite the abundance of alternatives—ranging from nearest neighbor methods (Bhavsar, 1978; Banerjee and Abel, 2020) to sophisticated persistent homology (Pourojaghi, Malekjani and Davari, 2024; Yip, Rouhiainen and Shiu, 2025) or information-geometric analyses (Giesel et al., 2021)—the two-point correlation function (2PCF) and its Fourier transform, the power spectrum, remain central statistical tools due to their robust constraints on matter clustering in massive redshift surveys[1].

2PCF admits a simple interpretation. It quantifies the excess probability of finding two objects located at $\mathbf{x}_1$ and $\mathbf{x}_2$ with respect to a uniform Poisson distribution (Peebles, 2020)

$$d\mathcal{P} = \bar{n}^2(z)\ [1+\xi]\ d^3x_1\, d^3x_2. \tag{2.1}$$

Assuming the symmetries of an ideal FLRW universe simplifies the correlation function substantially by removing several degrees of freedom under isotropy and homogeneity. The galaxy correlation function, as a biased tracer of the underlying dark matter field (§2.2.3), then takes the form

$$\langle \delta_g(\mathbf{x}_1, z)\, \delta_g(\mathbf{x}_2, z)\rangle = \xi_g(|\mathbf{x}_1 - \mathbf{x}_2|, z) = \xi_g(r, z) \tag{2.2}$$

where the angular brackets represent an ensemble average, ξ_g is the galaxy two-point correlation function and $\mathbf{r} = \mathbf{x}_2 - \mathbf{x}_1$ is the separation vector.

While in principle the correlation function and its Fourier conjugate (power spectrum) contain the same information, one or the other may prove more useful depending on the specific application. We can understand the power spectrum $P(k,z)$ as the autocorrelation function defined in the Fourier space,

---

[1] The allure of the 2PCF is, in-fact, so enduring that it is abundantly used in several other scientific disciplines too. For instance, the formalism developed by Ripley (1977) is now used to study patterns of species distribution in forestry data (Nuske, Sprauer and Saborowski, 2009).

$$\left\langle\tilde{\delta}(\boldsymbol{k},z)\tilde{\delta}\left(\boldsymbol{k}',z\right)\right\rangle = (2\pi)^3\delta_{\mathrm{D}}\left(\boldsymbol{k}+\boldsymbol{k}'\right)P(k,z) \tag{2.3}$$

where $\mathbf{k}$ and $\mathbf{k}'$ are the wave-vectors and a Fourier space overdensity field is defined as

$$\tilde{\delta}(\boldsymbol{k},z) = \int \delta(\boldsymbol{x},z)e^{\mathrm{i}\boldsymbol{k}\cdot\boldsymbol{x}}\,\mathrm{d}^3x. \tag{2.4}$$

From the governing equations of cosmic structure formation, the redshift evolution of the galaxy power spectrum P_g is typically modeled as

$$P_{\mathrm{g}}(k,z) = b^2(z)D_+^2(z)P(k,z=0), \tag{2.5}$$

where $b(z)$ is the linear bias and $D_+(z)$ is the growth factor.

2.1.1 Global Plane-Parallel Approximation

Due to redshift-space distortions, the symmetries of an ideal FLRW universe do not fully carry over to observational data. Translational invariance is broken (Szalay, Matsubara and Landy, 1998), spacetime coordinates become entangled along our past light cone (Bertacca, 2020), and as a result, the simplified form of the two-point correlation function in Eq. (2.2) must be generalized:

$$\langle\,\delta_g(\mathbf{x}_1,z_1)\,\delta_g(\mathbf{x}_2,z_2)\rangle\ = \xi_g(\mathbf{x}_1,\mathbf{x}_2,z_1,z_2). \tag{2.6}$$

To circumvent the full complexity, Kaiser (1987) suggested the *Global Plane Parallel* (GPP) approximation which posits that for sufficiently small sky volumes and distant observers, all lines-of-sight (LOS) are effectively parallel and can be represented by a single LOS direction $\hat{x}_c$. Under these assumptions, the correlation function can be parameterized by separation $\mathbf{r}$, line-of-sight $\hat{x}_c$ and redshift z, as given in (Hamilton, 1992; Hamilton and Culhane, 1997)

$$\xi_{\mathrm{g}}\left(r,\hat{\boldsymbol{r}}\cdot\hat{\boldsymbol{x}}_{\mathrm{c}},z\right) = \sum_{l=0,2,4}\mathcal{F}_\ell(z)D_+^2(z)b^2(z)\zeta_\ell(r)\mathcal{L}_\ell\left(\hat{\boldsymbol{r}}\cdot\hat{\boldsymbol{x}}_{\mathrm{c}}\right), \tag{2.7}$$

where

$$\zeta_\ell(r) = \frac{i^\ell}{2\pi^2}\int k^2P(k,z=0)j_\ell(kr), \tag{2.8}$$

$\mathcal{L}_\ell$ are the Legendre polynomials and j_ℓ represent the spherical Bessel functions (show in Fig. 2.1). The appearance of Legendre polynomials and Bessel functions is unsurprising since the origins of both can be traced back to early attempts at solving equations describing the celestial sphere[2,3].

---

[2] In 1784, shortly after his award-winning treatise on projectiles in resistive medium, Legendre published a paper titled '*Sur l'attraction des Sphéroïdes homogènes*' (On the Attraction of Homogeneous Spheroids) (Legendre, 1785). Here, he presented his work on the so-called Legendre polynomials and how they relate to solutions of Laplace's equation for gravitational potential.

[3] Although Friedrich Bessel was not one of the first people to work with the spherical functions now bearing his name, he did launch a thorough systematic investigation of them. One of Bessel's motivations for this was to simplify a series expansion by Lagrange to solve the transcendental Kepler equation (Dutka, 1995)

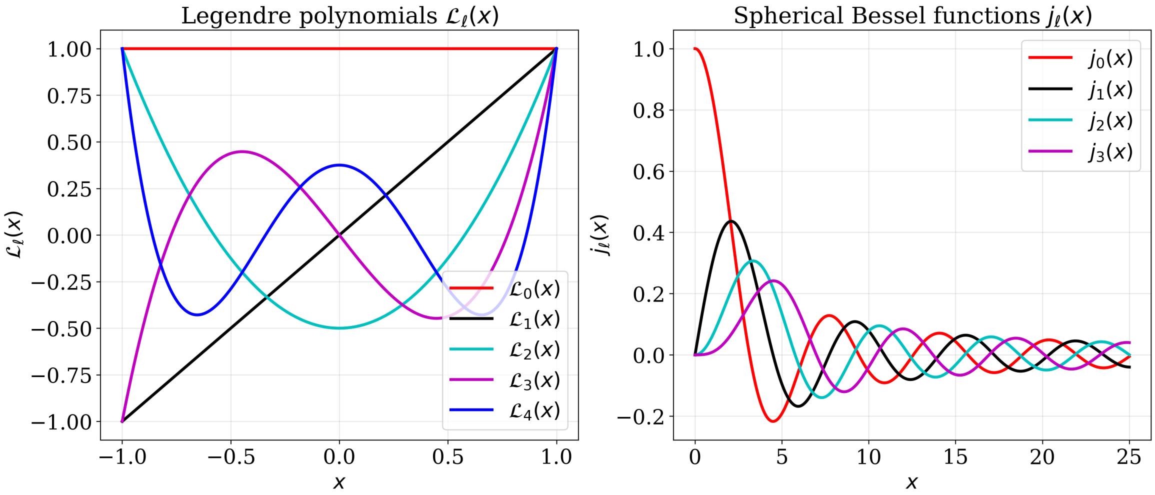

Figure 2.1: Legendre polynomials (left) and Spherical Bessel Functions (right) computed for a range of different ℓs. These functions serve as helpful basis for projecting out the multipole structure of redshift space distortions and estimating the different multipole orders of two-point statistics.

The power spectrum in redshift space, under the GPP approximation, takes an analogous multipole-decomposed form

$$P_{\mathrm{g,\,s}}(\boldsymbol{k}, z) = \sum_{l} \mathcal{F}_\ell(z) D_+^2(z) b^2(z) P(k, z=0) \mathcal{L}_\ell\left(\hat{\boldsymbol{k}} \cdot \hat{\boldsymbol{x}}_{\mathrm{c}}\right). \tag{2.9}$$

For thick redshift bins, an effective $\mathcal{F}_\ell$ parameter can be defined as

$$F_{\mathrm{eff}\,,\ell}\left(z_i, z_f\right) = \frac{\int_{z_i}^{z_f} \mathcal{F}_\ell(z) b^2(z) D_+^2(z) \bar{n}_{\mathrm{g}}^2(z) \left(\mathrm{d}V_{\mathcal{S}}/\mathrm{d}z\right) \mathrm{d}z}{\int_{z_i}^{z_f} \bar{n}_{\mathrm{g}}^2(z) \left(\mathrm{d}V_{\mathcal{S}}/\mathrm{d}z\right) \mathrm{d}z} \tag{2.10}$$

where $V_{\mathcal{S}}$ is the survey volume.

If we restrict ourselves to the classical non-relativistic redshift space distortions (as in Eq. (1.87)),then the distortion can be fully characterized by the first three even multipoles under the GPP approximation

$$\mathcal{F}_0(z) = 1 + \frac{2}{3}\beta(z) + \frac{1}{5}\beta^2(z) \tag{2.11}$$

$$\mathcal{F}_2(z) = \frac{4}{3}\beta(z) + \frac{4}{7}\beta^2(z) \tag{2.12}$$

$$\mathcal{F}_4(z) = \frac{8}{35}\beta^2(z) \tag{2.13}$$

where the linear redshift distortion parameter is defined as

$$\beta(z) = \frac{1}{b(z)} \frac{\mathrm{d}\ln D_+}{\mathrm{d}\ln a}\bigg|_{a=\frac{1}{(1+z)}}. \tag{2.14}$$

Clearly, for small β, the monopole dominates with higher order multipole contributing progressively less. Although the general relativistic effects redistribute the power into additional multipole moments, the monopole amplitude remains the dominant signal even in the relativistic treatment (discussed later in §2.1.3).

2.1.2 Yamamoto-Bianchi Estimator

To study the additional multipoles mentioned in the previous subsection, we will utilize a numerical implementation of the Yamamoto-Bianchi (YB) Estimator (Yamamoto, 2003; Bianchi et al., 2015) which is a minor modification of the famous prescription by Feldman, Kaiser and Peacock (1994). To derive the form of the YB estimator, we use the definition of the FKP field (Feldman, Kaiser and Peacock, 1994) as our starting point

$$F(\boldsymbol{x}) = \frac{w(\boldsymbol{x})}{\sqrt{A}} \left[\widehat{n}_g(\boldsymbol{x}) - \alpha \widehat{n}_r(\boldsymbol{x})\right], \tag{2.15}$$

where, within a given redshift bin, $\hat{n}_g(\boldsymbol{x})$ is the number density field of the observed galaxy catalog and $\hat{n}_r(\boldsymbol{x})$ is the number density field of the corresponding randoms catalog (which is generated such that they match the redshift distribution of the data but contain no intrinsic clustering). We will have more to say about the catalog generation in §2.2. Additionally, the standard FKP weights $w(\boldsymbol{x})$ do not affect the power spectrum estimate but are tuned to minimize variance in the measurements (Feldman, Kaiser and Peacock, 1994)

$$w(\boldsymbol{x}) = \mathcal{I}(\boldsymbol{x})\, [1 + \bar{n}_g(\boldsymbol{x})\mathcal{P}_0]^{-1}, \tag{2.16}$$

where $\mathcal{P}_0 = 2 \times 10^4\, \mathrm{Mpc}^3 h^{-3}$ and $\mathcal{I}(\boldsymbol{x})$ is an indicator function which takes the value of one inside the redshift bin and zero everywhere else. Using these weights, we can also define the standard FKP normalization parameter as

$$A \equiv \int w^2(\boldsymbol{x}) \bar{n}_g^2(\boldsymbol{x})\, d^3x. \tag{2.17}$$

Finally, the α parameter[4] accounts for the fact that the artificially generated randoms catalog often includes far more objects than the observed galaxy catalog. This means that α acts as a normalization constant which scales down the average number density of the randoms catalog to match that of the galaxy catalog,

$$\alpha = \frac{\int w(\boldsymbol{x})\widehat{n}_g(\boldsymbol{x})\mathrm{d}^3x}{\int w(\boldsymbol{x})\widehat{n}_\mathrm{r}(\boldsymbol{x})\mathrm{d}^3x}. \tag{2.18}$$

In our case, the $\alpha \approx 0.1$, indicating the inclusion of ten times as many synthetic objects in the randoms catalog compared to the observed ones in the galaxy catalog.

Once the FKP field is constructed, which involves running an interpolation routine to convert a list of particle coordinates into a density function defined on a grid (§2.1.4), the power spectrum multipoles can be estimated using the YB estimator as (Yamamoto, Nishioka and Taruya, 2000)

---

[4] This is not to be confused with α_o, α_c and $\Delta\alpha$ in §1.4. The notational clash arises from entrenched conventions in both power spectrum and FOTO studies.

$$\hat{P}_\ell(k) = (2\ell+1) \iiint \left[F\left(\boldsymbol{x}_1\right) F\left(\boldsymbol{x}_2\right) \mathcal{L}_\ell\left(\hat{\boldsymbol{k}} \cdot \hat{\boldsymbol{x}}_{\rm m}\right) e^{-i\cdot\mathbf{k}\cdot(\mathbf{x_1}-\mathbf{x_2})} d^3x_1\, d^3x_2 \frac{d\Omega_k}{4\pi} \right] - \hat{P}_\ell^{\rm SN}(k) \quad , \tag{2.19}$$

where the Poisson shot noise contribution arising due to an over counting of self-pairs is expressed as

$$\hat{P}_\ell^{\rm SN}(k) = \frac{(1+\alpha)}{A} \int w^2(\boldsymbol{x}) \widehat{n}_{\rm g}(\boldsymbol{x}) \mathcal{L}_\ell\left(\hat{\boldsymbol{k}} \cdot \hat{\boldsymbol{x}}_{\rm m}\right) d^3x. \tag{2.20}$$

Further, the unit vector $\hat{\boldsymbol{x}}_m$ refers to a choice of convention required to go beyond the GPP approximation (Yamamoto, Nakamichi et al., 2006). The extension beyond GPP is facilitated by the so-called wide-angle formalism which parametrizes the triangle subtended by a pair of galaxies onto the observer. Fig. 2.2 summarizes three distinct parametrization conventions and Reimberg, Bernardeau and Pitrou (2016) reviews of the impact of the chosen convention on the power spectrum multipoles. For instance, Reimberg, Bernardeau and Pitrou (2016) find that the end-point parameterization, owing to its inherent asymmetry, introduces spurious odd-multipoles even within the classical Kaiser framework. `LIGER` papers (Borzyszkowski, Bertacca and Porciani, 2017; Elkhashab, Porciani and Bertacca, 2021; Elkhashab, Porciani and Bertacca, 2024) adopt the mid-point parametrization for defining $\hat{\boldsymbol{x}}_m$ because this is the standard within Euclid collaboration. Thus, we define

$$\boldsymbol{r} = \boldsymbol{x_2} - \boldsymbol{x_1}, \quad \boldsymbol{x}_{\rm m} = \frac{\boldsymbol{x_2} + \boldsymbol{x_1}}{2}, \quad \mu \equiv \cos\theta = \hat{\boldsymbol{r}}.\hat{\boldsymbol{x}}_m. \tag{2.21}$$

We also note that, in Eq. (2.19), we have isolated multipole moments of the power spectrum corresponding to different values of ℓ and expressed them as a family of one-dimensional functions. This is done by first projecting the three-dimensional FKP fields onto the (orthogonal) Legendre polynomial basis $\mathcal{L}_\ell$ and, then, computing angular averages of the projected Fourier transform kernels over shells of different radii in the k-space.

Lastly, there is one more practical limitation to incorporate in our discussion of the power spectrum before deriving the expected signatures of the FOTO effect. Here, I am referring to the fact that we only observe a limited volume of the universe. Consequently, the Fourier transform introduces spurious signatures (sometimes called 'ringing') in the estimated power spectrum multipoles. To account for this, we convolve the power spectrum by modifying the expression for the FKP field (Eq. (2.15)) as (Peacock, 1991; Beutler et al., 2014; Mattia and Ruhlmann-Kleider, 2019)

$$F(\boldsymbol{x}) = W(\boldsymbol{x})\delta_{\rm g}(\boldsymbol{x}) - W(\boldsymbol{x}) \frac{\int W\left(\boldsymbol{x}'\right) \delta_{\rm g}\left(\boldsymbol{x}'\right) d^3x'}{\int W\left(\boldsymbol{x}'\right) d^3x'}, \tag{2.22}$$

where the window function is given by

$$W(\boldsymbol{x}) = \frac{w(\boldsymbol{x})\, \bar{n}_g(\boldsymbol{x})}{\sqrt{A}}. \tag{2.23}$$

with $w(\boldsymbol{x})$ being the standard FKP weights (Eq. (2.16)) and A being the FKP normalization constant (Eq. (2.17)). The first term of the modified FKP field in Eq. (2.22) corresponds to the observed overdensity field and the second term can be interpreted as an integral constraint which enforces that

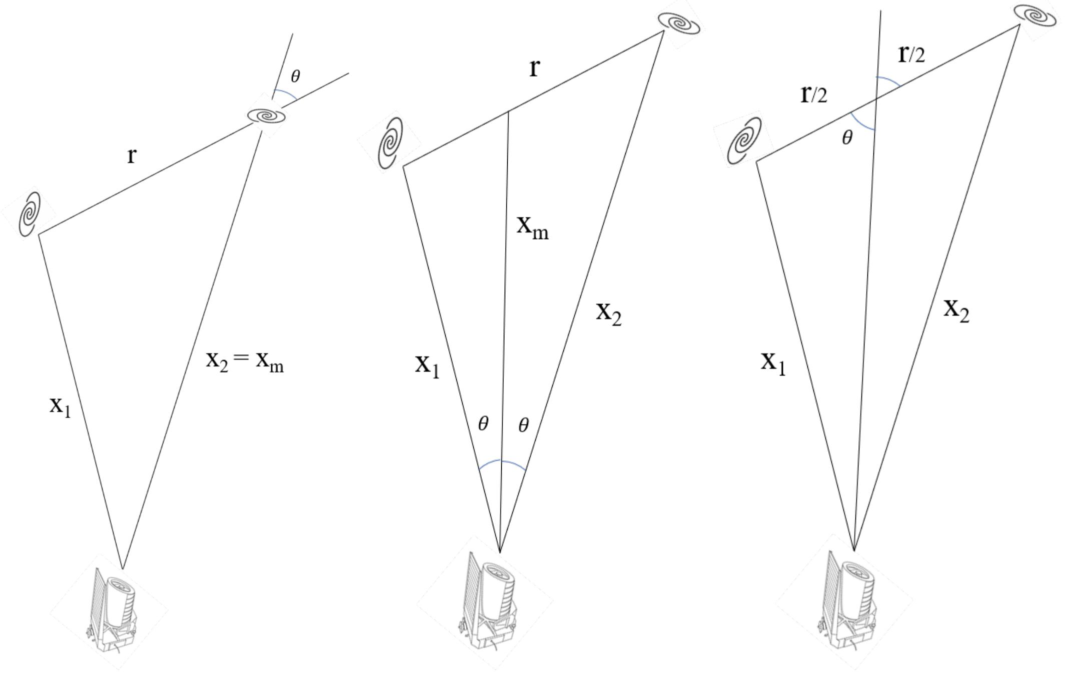

(a) End-point (b) Bisector (c) Midpoint

Figure 2.2: Illustration of three possible parameterizations available for wide-angle formalism as discussed in Reimberg, Bernardeau and Pitrou (2016). `LIGER` papers adopt the mid-point parameterization as it is the standard chosen within the Euclid collaboration. The observer is depicted by a (stable-diffusion generated) cartoon of Euclid at the bottom.

the average of $F(\boldsymbol{x})$ over the survey volume necessarily vanishes (Mattia and Ruhlmann-Kleider, 2019).

We can now write the genera expression we will use for estimating the power spectrum in terms of the true galaxy field as

$$\boxed{\begin{aligned} P_\ell(k) = \int W\left(\boldsymbol{x}_1\right) W\left(\boldsymbol{x}_2\right) \left\langle \delta_{\mathrm{g}}\left(\boldsymbol{x}_1\right) \delta_{\mathrm{g}}\left(\boldsymbol{x}_2\right)\right\rangle e^{-\mathrm{i}\boldsymbol{k}\cdot\left(\boldsymbol{x}_2-\boldsymbol{x}_1\right)} \\ \times \mathcal{L}_\ell\left(\hat{\boldsymbol{k}}\cdot\boldsymbol{x}_{\mathrm{m}}\right) \mathrm{d}^3x_1\,\mathrm{d}^3x_2 \frac{\mathrm{d}\Omega_k}{4\pi} + P_{\mathrm{IC}}, \end{aligned}} \tag{2.24}$$

where P_{IC} corresponds to the contribution from the integral constraint term and the angular brackets represent ensemble average as usual.

2.1.3 FOTO Multipole Moments

Having introduced the YB estimator, we can now finally try to assess the impact of the observer velocity term on the power spectrum multipole moments. In §1.4, we found that the observed density field can be decomposed such that the impacts of the relativistic distortions can be isolated

$$\delta_{\mathrm{obs}}(\boldsymbol{x}) = \delta_{\mathrm{com}}(\boldsymbol{x}) + \frac{\alpha_{\mathrm{o}}(x)}{x} \frac{\boldsymbol{v}_{\mathrm{o}} . \hat{\boldsymbol{x}}}{aH} \tag{2.25}$$

into a single function defined as

$$\alpha_{\mathrm{o}}(x) \equiv 2(1-Q) - \frac{xH}{c(1+z)}\mathcal{E} + \frac{xH}{c(1+z)}\left[3 - \frac{1+z}{H}\frac{\mathrm{d}H}{\mathrm{d}z}\right]. \tag{2.26}$$

We will now plug this observed density field δ_{obs} into the window-convolved Yamamoto Bianchi estimator from Eq. (2.19) (ignoring the integral constraint term) and write

$$P_\ell(k) = \int W\left(\boldsymbol{x}_1\right) W\left(\boldsymbol{x}_2\right) \left\langle \delta_{\mathrm{obs}}\left(\boldsymbol{x}_1\right) \delta_{\mathrm{obs}}\left(\boldsymbol{x}_2\right)\right\rangle e^{-i\boldsymbol{k}\cdot(\boldsymbol{x}_2-\boldsymbol{x}_1)} \mathcal{L}_\ell\left(\hat{\boldsymbol{k}} \cdot \boldsymbol{x}_{\mathrm{m}}\right) \mathrm{d}^3x_1\, \mathrm{d}^3x_2 \frac{\mathrm{d}\Omega_k}{4\pi} \tag{2.27}$$

To compute the power spectrum as prescribed by Eq. (2.19), we still need to perform pair-counting which scales poorly as $O\left(n^2\right)$ and serves as a severe computational bottleneck. If we can employ Fast-Fourier Transform (FFT) algorithms, which scale as $O(n \log n)$, we can achieve massive efficiency gains (discussed later in §2.1.4). The applicability of FFTs, however, is contingent on whether the spatial integrals in Eq. (2.19) can be separated into two distinct terms. Unfortunately, the $\mathcal{L}(\hat{\boldsymbol{k}} . \hat{\boldsymbol{x}}_{\boldsymbol{m}})$ term manifestly prevents such a splitting of the integrand. To overcome this bottleneck, numerical implementations of the YB estimator often modify the argument of the Legendre polynomial in lines with the approximation stating $\hat{\boldsymbol{x}}_m \approx \hat{\boldsymbol{x}}_{1,2}$ (Yamamoto, Nakamichi et al., 2006). This, in-effect, substitutes the mid-point LOS vector with a vector pointing towards one of the objects in the galaxy pair. Though the resulting calculation is made more convenient, it should be noted that the approximate statistic we compute is a different quantity altogether (which only reduces to Eq. (2.19) when the galaxy pairs considered remain sufficiently close).

If we ignore potential cross-correlations between δ_{com} and v_{o} by excluding the local universe ($z < 0.05$) (Nadolny et al., 2021) from our analysis, we can write the observed power spectrum $P_{\mathrm{obs},\ell}$ as a sum of contributions from comoving density field $P_{\mathrm{com},\ell}$ and kinematic dipole induced effects (Elkhashab, Porciani and Bertacca, 2024)

$$P_{\mathrm{obs},\ell}(k) = P_{\mathrm{com},\ell}(k) + P_{\mathrm{dip},\ell}(k). \tag{2.28}$$

Focusing on the dipole distortions, we find

$$P_{\mathrm{dip},\ell}(k) = \frac{2\ell+1}{A} \iiint B_1 B_2 \left(\boldsymbol{v}_{\mathrm{o}} \cdot \hat{\boldsymbol{x}}_1\right) \left(\boldsymbol{v}_{\mathrm{o}} \cdot \hat{\boldsymbol{x}}_2\right) \mathrm{e}^{i\boldsymbol{k}\cdot(\boldsymbol{x}_1-\boldsymbol{x}_2)} \mathcal{L}_\ell\left(\hat{\boldsymbol{k}} \cdot \hat{\boldsymbol{x}}_2\right) \mathrm{d}^3x_1\, \mathrm{d}^3x_2 \frac{\mathrm{d}\Omega_k}{4\pi} \tag{2.29}$$

where $B_i \equiv \bar{n}_i \alpha_{\mathrm{o,i}} / (x_i a_i H_i)$ contains the FOTO effect and the normalization constant is $A = \int \bar{n}^2(x) d^3x$. Here, we have set the weights as $w = 1$ for convenience but, as mentioned earlier, this affects only the covariance by construction (and not the features of signal itself).

We now split the integral in two parts by

$$P_{\mathrm{dip},\ell}(k) = \frac{2\ell+1}{A} \int \left[\int B_1\left(\boldsymbol{v}_{\mathrm{o}} \cdot \hat{\boldsymbol{x}}_1\right) \mathrm{e}^{i\boldsymbol{k}\cdot\boldsymbol{x}_1}\, \mathrm{d}^3 x_1 \right] \left[\int B_2\left(\boldsymbol{v}_{\mathrm{o}} \cdot \hat{\boldsymbol{x}}_2\right) \mathrm{e}^{-i\boldsymbol{k}\cdot\boldsymbol{x}_2} \mathcal{L}_\ell\left(\hat{\boldsymbol{k}} \cdot \hat{\boldsymbol{x}}_2\right) \mathrm{d}^3 x_2 \right] \frac{\mathrm{d}\Omega_k}{4\pi}. \tag{2.30}$$

To make progress with simplifying this expression further, we will require four mathematical identities that we shall now introduce.

1. **Plane-Wave Expansion** describes planar waves as a superposition of spherical waves

$$\mathrm{e}^{\mathrm{i}\boldsymbol{k}\cdot\boldsymbol{x}} = \sum_\ell (2\ell+1)\mathrm{i}^\ell j_\ell(kx)\mathcal{L}_\ell(\hat{\boldsymbol{k}} \cdot \hat{\boldsymbol{x}}). \tag{2.31}$$

   It was famously used to describe sound waves by Strutt (1877) (better known as the third Baron of Rayleigh), and then, by Sommerfeld (1896) to describe electrodynamic diffraction[5]. The plane wave expansion is still ubiquitously found in the study of nuclear scattering (Mehrem, 2011). Using this identity introduces radial integrals of spherical Bessel functions $j_l(kr)$ in our calculations.

2. **Orthogonality of Legendre Polynomials on the Sphere** can be stated as

$$\int \mathcal{L}_\ell(\hat{\boldsymbol{q}} \cdot \hat{\boldsymbol{x}})\mathcal{L}_{\ell'}(\hat{\boldsymbol{k}} \cdot \hat{\boldsymbol{x}})\mathrm{d}\Omega_x = \frac{4\pi}{2\ell'+1}\mathcal{L}_{\ell'}(\hat{\boldsymbol{q}} \cdot \hat{\boldsymbol{k}})\delta^{\mathrm{K}}_{\ell\ell'}. \tag{2.32}$$

   This ensures that integrating the product of two Legendre polynomials over all directions on a two-sphere cancels out to zero — unless, the two have the same multipole index ℓ.

3. **Product-to-Sum Identity** states that the product of two multipole moments at any given location on the two-sphere can be written re-expressed as a weighted sum of finitely many Legendre polynomials,

$$\mathcal{L}_\ell(\hat{\boldsymbol{q}} \cdot \hat{\boldsymbol{x}})\mathcal{L}_{\ell'}(\hat{\boldsymbol{q}} \cdot \hat{\boldsymbol{x}}) = \sum_{n=\ell-\ell'}^{\ell+\ell'} \begin{pmatrix} \ell & \ell' & n \\ 0 & 0 & 0 \end{pmatrix}^2 (2n+1)\mathcal{L}_n(\hat{\boldsymbol{q}} \cdot \hat{\boldsymbol{x}}). \tag{2.33}$$

   Interestingly, the weights corresponding to the different polynomial orders n features a Wigner-3j matrix (Wigner, 1993), which is otherwise famous among physicists as a (nicer) alternative to Clebsch-Gordan Coefficients. The 3j matrix is a mathematical object with rich symmetries, recursion relations and vanishing criteria (Pain, 2020; Hopersky, Nadolinsky and Koneev, 2025), which abstracts away some underlying complexity of dealing with the multipole structure.

4. **Radial Moment** of a basis projection is defined as

$$I_n \equiv \int x^2 B_1 j_n(kx)\mathrm{d}x, \tag{2.34}$$

---

[5] Coincidentally, in the field of optics, the Rayleigh-Sommerfeld Diffraction is also popularly abbreviated as RSD.

and it describes how efficiently the FOTO signal (by which I mean $\alpha_{\rm o}$ inside B_1) couples to a a spherical Bessel basis of order n (Elkhashab, 2024).

For the actual solution, we begin by focusing on the integrand in the first square bracket of Eq. (2.30) (Elkhashab, 2024)

$$\begin{aligned}\int B_1\left(\boldsymbol{v}_{\rm o}\cdot\hat{\boldsymbol{x}}\right)\mathrm{e}^{\mathrm{i}\boldsymbol{k}\cdot\boldsymbol{x}}\,\mathrm{d}^3x &= \sum_{\ell'}\left(2\ell'+1\right)\mathrm{i}^{\ell'}\int A\left(\boldsymbol{v}_{\rm o}\cdot\hat{\boldsymbol{x}}\right)j_{\ell'}(kx)\mathcal{L}_{\ell'}(\hat{\boldsymbol{k}}\cdot\hat{\boldsymbol{x}})\mathrm{d}\Omega_x\,\mathrm{d}x\\ &= v_{\rm o}\sum_{\ell'}\left(2\ell'+1\right)\mathrm{i}^{\ell'}I_{\ell'}\frac{4\pi}{2\ell'+1}\mathcal{L}_{\ell'}\left(\hat{\boldsymbol{v}}_o\cdot\hat{\boldsymbol{k}}\right)\delta^{\rm D}_{\ell'1}\\ &= 4\pi\mathrm{i}v_{\rm o}I_1\mathcal{L}_1\left(\hat{\boldsymbol{v}}_o\cdot\hat{\boldsymbol{k}}\right).\end{aligned}\tag{2.35}$$

And, for the second square bracket containing the Legendre polynomial term, we write

$$\begin{aligned}&\int B_2\left(\boldsymbol{v}_{\rm o}\cdot\hat{\boldsymbol{x}}\right)\mathrm{e}^{-\mathrm{i}\boldsymbol{k}\cdot\boldsymbol{x}}\mathcal{L}_\ell(\hat{\boldsymbol{k}}\cdot\hat{\boldsymbol{x}})\mathrm{d}^3x =\\ &\quad\sum_{\ell'}\left(2\ell'+1\right)(-\mathrm{i})^{\ell'}I_{\ell'}\int\left(\hat{\boldsymbol{v}}_o\cdot\hat{\boldsymbol{x}}\right)\mathcal{L}_{\ell'}(\hat{\boldsymbol{k}}\cdot\hat{\boldsymbol{x}})\mathcal{L}_l(\hat{\boldsymbol{k}}\cdot\hat{\boldsymbol{x}})\mathrm{d}\Omega_x\\ &=v_{\rm o}\sum_{\ell'}\left(2\ell'+1\right)(-\mathrm{i})^{\ell'}I_{\ell'}\int\left(\hat{\boldsymbol{v}}_o\cdot\hat{\boldsymbol{x}}\right)\sum_{n=\ell-\ell'}^{\ell+\ell'}\begin{pmatrix}\ell & \ell' & n\\ 0 & 0 & 0\end{pmatrix}^2(2n+1)\mathcal{L}_n(\hat{\boldsymbol{k}}\cdot\hat{\boldsymbol{x}})\mathrm{d}\Omega_x\\ &=v_{\rm o}\sum_{\ell'}\sum_{n=\ell-\ell'}^{\ell+\ell'}\begin{pmatrix}\ell & \ell' & n\\ 0 & 0 & 0\end{pmatrix}^2\left(2\ell'+1\right)(2n+1)(-\mathrm{i})^{\ell'}I_{\ell'}\int\mathcal{L}_1\left(\hat{\boldsymbol{v}}_o\cdot\hat{\boldsymbol{x}}\right)\mathcal{L}_n(\hat{\boldsymbol{k}}\cdot\hat{\boldsymbol{x}})\mathrm{d}\Omega_x\\ &=v_{\rm o}\sum_{\ell'}\sum_{n=\ell-\ell'}^{\ell+\ell'}\begin{pmatrix}\ell & \ell' & n\\ 0 & 0 & 0\end{pmatrix}^2\left(2\ell'+1\right)(2n+1)(-\mathrm{i})^{\ell'}I_{\ell'}\left[\frac{4\pi}{2n+1}\mathcal{L}_n\left(\hat{\boldsymbol{v}}_o\cdot\hat{\boldsymbol{k}}\right)\delta^{\rm D}_{n1}\right]\\ &=4\pi v_{\rm o}\sum_{\ell'}\begin{pmatrix}\ell & \ell' & 1\\ 0 & 0 & 0\end{pmatrix}^2\left(2\ell'+1\right)(-\mathrm{i})^{\ell'}I_{\ell'}\mathcal{L}_1\left(\hat{\boldsymbol{v}}_o\cdot\hat{\boldsymbol{k}}\right).\end{aligned}\tag{2.36}$$

On substituting Eq. (2.35)-2.36 back into Eq. (2.30), we get our final result as -

$$\boxed{\begin{aligned}P_{\ell,\rm dip}(k) = \frac{2\ell+1}{N}\frac{v_0^2}{H_0^2}\int&\left[4\pi iI_\ell\mathcal{L}_1(\hat{\mathbf{v}}_o\cdot\hat{\mathbf{k}})\right]\times\\ &\left[4\pi\sum_{\ell'=0}^{\infty}\begin{pmatrix}\ell & \ell' & 1\\ 0 & 0 & 0\end{pmatrix}^2(2\ell'+1)(-i)^{\ell'}I_{\ell'}\mathcal{L}_1(\hat{\mathbf{v}}_o\cdot\hat{\mathbf{k}})\right]\frac{d^2\Omega_k}{4\pi}\\ &=\frac{16\pi^2(2\ell+1)}{3}\frac{v_0^2}{H_0^2}\frac{I_1}{N}\sum_{\ell'=0}^{\infty}\begin{pmatrix}\ell & \ell' & 1\\ 0 & 0 & 0\end{pmatrix}^2(2\ell'+1)(-1)^{\ell'}(i)^{\ell'+1}I_{\ell'}.\end{aligned}}\tag{2.37}$$

The first few multipoles were given by Elkhashab, Porciani and Bertacca (2024) as

$$P_{0,\mathrm{dip}}(k) = \frac{16\pi^2}{3}\frac{v_0^2}{H_0^2}\frac{I_1^2(k)}{N}, \tag{2.38}$$

$$P_{1,\mathrm{dip}}(k) = \frac{16\pi^2 i}{3}\frac{v_0^2}{H_0^2}\frac{I_1(k)[I_0(k)-2I_2(k)]}{N}, \tag{2.39}$$

$$P_{2,\mathrm{dip}}(k) = -\frac{16\pi^2}{5}\frac{v_0^2}{H_0^2}\frac{I_1(k)[2I_1(k)+3I_3(k)]}{N}, \tag{2.40}$$

$$P_{3,\mathrm{dip}}(k) = \frac{16\pi^2 i}{7}\frac{v_0^2}{H_0^2}\frac{I_1(k)[-3I_2(k)+4I_4(k)]}{N}, \tag{2.41}$$

$$P_{4,\mathrm{dip}}(k) = -\frac{16\pi^2}{9}\frac{v_0^2}{H_0^2}\frac{I_1(k)[4I_3(k)+5I_5(k)]}{N}. \tag{2.42}$$

The odd-multipoles in our results come out to be imaginary as a consequence of the inherent asymmetry in our estimator. Although the first square bracket term is symmetric under reflections $\boldsymbol{k} \to -\boldsymbol{k}$, the second square bracket is symmetric only for even multipoles and anti-symmetric for odd multipoles. Consequently, Eq. (2.37) has real and imaginary components which average out to zero for odd and even multipoles respectively (Elkhashab, Porciani and Bertacca, 2024).

To visualize these contributions, Fig. 2.3 shows the power spectrum multipoles estimated with the Yamamoto–Bianchi estimator under different assumptions (real-space, Kaiser limit, relativistic effects, and observer velocity). While the example here is for a Euclid-like survey mock, the figure's purpose at this stage is pedagogical: to illustrate how redshift-space distortions redistribute power across multipoles. A detailed discussion about the generation of these Euclid like mocks will follow in §2.2 and the statistical inferences from these signal measurements in 3.1. A clearer view of the analytic predictions about the FOTO signal in such Euclid-like mocks is presented in Fig. 2.4.

2.1.4 FFT Implementations

The theoretical FOTO multipoles derived in the previous subsection contain no stochasticity. However, to test these predictions against real or mock data, we must estimate the FOTO signal from discretely sampled galaxy catalogs. For this, we rely on Fast Fourier Transforms (Heideman, D. H. Johnson and Burrus, 1985), which offer computational efficiency and, consequently, scale well for large survey catalogs.

Before running FFT-based estimators, objects in survey data must first be situated on a regular grid to produce a discretized density field. One convenient method to achieve this is the Cloud-in-Cell (CIC) algorithm (Hockney and Eastwood, 2021) which spreads the contribution of each particle's mass across a small cubic 'cloud' centered around it (i.e. on adjacent grid points). CIC can be neatly expressed as a convolution of particle positions with a window function that linearly interpolates particle mass at $\boldsymbol{x}_p$ to the grid vertices $\boldsymbol{x}_g$

$$\rho(\boldsymbol{x}_g) = \sum_p m_p\, W_{\mathrm{CIC}}(\boldsymbol{x}_g - \boldsymbol{x}_p), \quad \text{with} \quad W_{\mathrm{CIC}}(\boldsymbol{r}) = \prod_{i=x,y,z} w_{\mathrm{CIC}}(r_i), \tag{2.43}$$

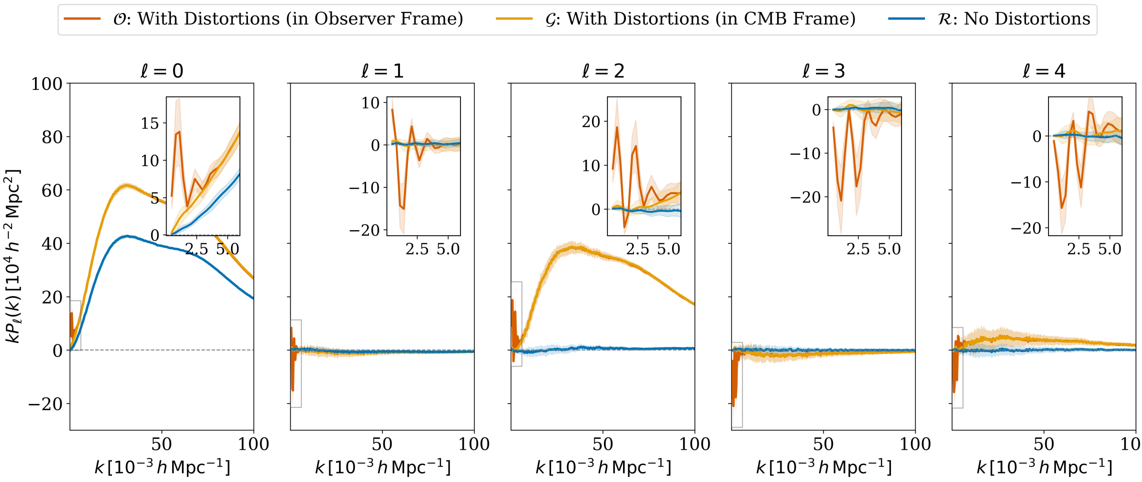

Figure 2.3: Power spectrum multipoles estimated for a Euclid like survey using a Yamamoto-Bianchi estimator. The different curves represent estimates for different catalogs $\mathcal{R}$ (real-space with no distortions), $\mathcal{G}$ (all relativistic effects in CMB rest frame) and $\mathcal{O}$ (all relativistic effects with peculiar velocity). In real-space, only the monopole is non-zero. Peculiar velocity of galaxies introduce power in $\ell = 2$ and $\ell = 4$ (Eq. 2.13) and observer peculiar velocity leaves an imprint across all multipoles on the largest scales (Eq. (2.37)). The inset figures zoom into the bandwidth relevant for the FOTO signal. Barring the FOTO signal, monopole term remains the dominant contribution to the total power. Note that $kP(k)$ is plotted (instead of $P(k)$) and, hence, the shape of the curves is artificially lifted for larger values of k.

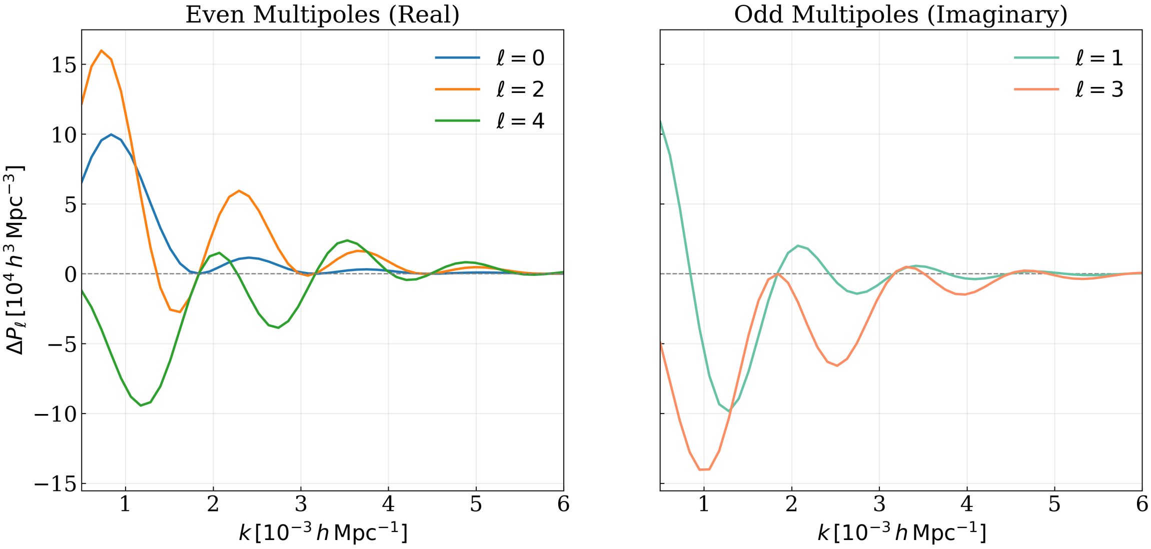

Figure 2.4: Theoretical expectations for FOTO effect computed for a Euclid-like survey in a redshift bin of $z \in [0.9, 1.8]$, assuming an observer velocity of $v_o = 369$km/s. The even multipoles appear with a real part while for the odd multipoles only the imaginary component survives. However, this only reflects the anti-symmetry of our estimator. We can easily choose a different convention which leads to imaginary even multipoles and real odd multipoles. The theoretical expectations for the FOTO signal are compared with measurements of simulated mocks in §3.

where the 1D CIC kernel is

$$w_{\mathrm{CIC}}(x) = \frac{1}{\Delta x} \begin{cases} 1, & |x| < \frac{1}{2}\Delta x \\ 0, & \text{otherwise} \end{cases} \tag{2.44}$$

and Δx is the grid spacing. The final density field is then obtained by summing contributions from all particles.

Compared to the simpler Nearest Grid Point (NGP) method in which each particle assigns its entire mass to the nearest grid point, CIC scheme provides a smoother interpolation and reduces aliasing effects. Aliasing arises when discretely sampled data are used to approximate a continuous field, particularly when structures vary on scales smaller than the sampling frequency. This can introduce spurious low-frequency features not present in the original signal. A familiar example from image data processing is the occurrence of Moiré patterns[6]. Higher-order interpolation schemes also exist, such as the Triangular Shaped Cloud (TSC) kernel and Piecewise Cubic Spline (PCS) methods (Hockney and Eastwood, 2021). These alternatives suppress numerical artifacts even more effectively, particularly at small scales. However, the improvement in accuracy at larger scales (relevant for relativistic effects) is marginal. Thus, CIC offers an optimal balance between computational efficiency and interpolation fidelity for our purposes.

We apply the CIC technique on the particle positions listed in galaxy and randoms catalogs to estimate the number density fields $\hat{n}_g$ and $\hat{n}_r$. This allows us to define the FKP field from Eq. (2.15) at all points on a discretized coordinate grid. Now, finally, we can use an FFT algorithm on the FKP field to get its Fourier conjugate in the k-space. This resulting k-space field is the three-dimensional power spectrum monopole $F_0(\boldsymbol{k})$. To make the inference calculations in Chapter 3 more manageable, we summarize the field statistics into a one-dimensional power-spectrum by calculating weighted averages along spherical shells of varying radii in the k-space as follows (Scoccimarro, 2015)

$$\widehat{P}_0(k) = \frac{1}{A}\left[\int \frac{d\Omega_k}{4\pi} \left|F_0(\mathbf{k})\right|^2 - \widehat{P}_0^{\mathrm{SN}}\right] \tag{2.45}$$

where A is the standard normalization constant and N_0 is the shot noise obtained by self-pairs in the first term.

The method described above was introduced by Scoccimarro (2015) but a slightly different FFT implementation to compute power spectrum multipoles was proposed by Hand et al. (2017). They report in their analysis (Hand et al., 2017) that by expanding every Legendre polynomial into its spherical harmonic basis, we can avoid some redundant computations. This brings down the number of FFTs required for computing the ℓ^{th} multipole from $(\ell+1)(\ell+2)/2$ (as in Cartesian decomposition of Scoccimarro (2015) and Bianchi et al. (2015)) to $2\ell+1$. At higher multipole moments, this difference can become substantial. For example, in computing nine even multipoles ($\ell_{\max} = 16$), the algorithm by Hand et al. (2017) offers a factor of $525/153 \approx 3.4$ improvement. In this dissertation, we restrict our analysis to $\ell_{\max} = 4$ and, hence, do not describe the alternate approach in greater detail. We do note, however, that several standard libraries for computing power spectrum multipoles (like `pypower`[7] and `nbodykit`[8]) utilize the more efficient FFT implementation using spherical harmonic decompositions.

---

[6] For further discussion in the context of rendering and sampling theory, see Pharr and Humphreys (2010)

[7] See `pypower` documentation: github.com/cosmodesi/pypower

[8] See `nbodykit` documentation: nbodykit.readthedocs.io

2.2 Generating Relativistic Mocks

Simulations play a doubly special role in cosmology, more so than in most other branches of physics. The first role, familiar across computational physics, is to help in understanding the macroscopic effects of analytically intractable micro-dynamics. It is practically impossible to capture the seemingly immeasurable complexities of billions of particles interacting gravitationally (even with electromagnetism and gas-dynamics absent from the mix). This forward-modeling of theoretical predictions is common in many domains of astrophysics. Unlike, however, the study of pulsars or accretion disks, cosmology has an extra role for simulations i.e. instantiating many realizations of the same underlying physics. Since we observe only one universe, we rely on a simulated ensemble to supplement predictions with a quantization of the corresponding covariance. We will have more to say about covariance later in Chapter 3 but, for now, we note the following trade-off. The more sophisticated a simulation is, i.e. the more of our theoretical machinery it attempts to forward model, the more computationally demanding it tends to become. Conversely, the more simulations we can generate, the better our understanding of the covariance becomes. This means, for finite computational resources (or, in AI industry slang *compute*), we must find a balance between the number of simulations and their fidelity.

The workflow adopted in this project for studying FOTO multipoles is based on the `LIGER` method, which strikes a pragmatic middle ground. The synthetic universes we construct *in silico* are detailed enough to capture the key relativistic effect (FOTO), yet far less resource-intensive than state-of-the-art multi-physics simulations. In fact, as I will explain, our pipeline bypasses the need for any full simulations at all (let alone general relativistic ones). This is achieved through a three-step procedure that circumvents reliance on resource intensive numerical solvers.

1. Generating non-general-relativistic initial conditions for N-body simulations using Einstein-Boltzmann solvers at different values of redshift (§2.2.1). This is done using `MonophonIC`[9] code (Hahn, Michaux et al., 2020) and it by-passes the need to perform N-body computations.

2. Adding relativistic shifts to the otherwise Newtonian particle positions with `LIGER` (§2.2.2). This substitutes the need for numerically solving Einstein field equations with the much simpler perturbative corrections derived in §1.3.3.

3. Painting luminous tracers with a biasing relation onto the dark matter distribution with `Buildcone` (§2.2.3). This avoids the need to work with hydro-simulations of baryonic matter.

We will now go through each of these three steps in more detail.

2.2.1 MonophonIC (`MUSIC2`) Newtonian Snapshots

At the heart of any initial condition generation code is the cosmological transfer function. A transfer function is the product of growth functions of different structures and the primordial time-independent

---

[9] Hahn and Abel (2011) originally developed a code called `MUSIC` which provided MUlti-Scale Initial Conditions used in galaxy formation studies. Overtime, the community moved towards using second and third order in linear perturbation theory while solving the Einstein-Boltzmann equations for structure formation seeds. So, Hahn, Michaux et al. (2020) created a sequel to the original code called `MUSIC2` but, since the intended use case then was cosmology studies (as opposed to galaxies), they chose to skip on the multi-scale feature. This explains the 'mono' in the alternate name of `MUSIC2` i.e. `MonophonIC`.

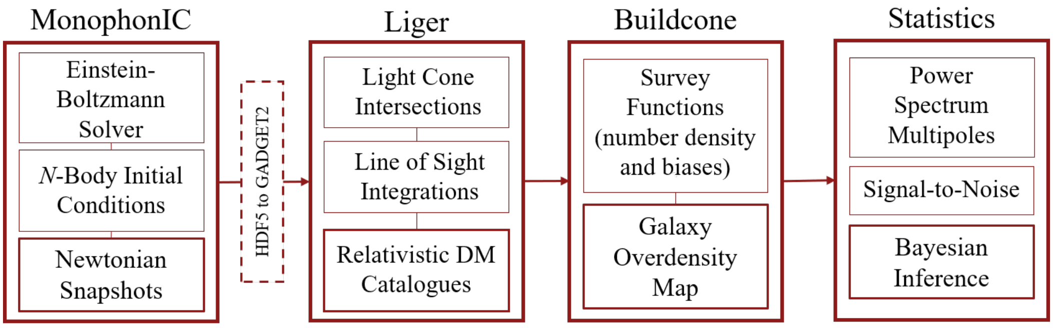
MonophonIC
Einstein-Boltzmann Solver
N-Body Initial Conditions
Newtonian Snapshots
HDF5 to GADGET2
Liger
Light Cone Intersections
Line of Sight Integrations
Relativistic DM Catalogues
Buildcone
Survey Functions (number density and biases)
Galaxy Overdensity Map
Statistics
Power Spectrum Multipoles
Signal-to-Noise
Bayesian Inference

Figure 2.5: LIGER method workflow used in this thesis. MonophonIC generates Newtonian N-body snapshots from Einstein–Boltzmann-consistent initial conditions; after conversion to Gadget-2 format these snapshots are processed by *LIGER*, which finds light-cone intersections and performs line-of-sight integrations to build fully relativistic dark-matter catalogs. *Buildcone* performs baryon painting based on survey functions to obtain a galaxy-overdensity map, which feeds the *Statistics* step (i.e. computing power-spectrum multipoles, signal-to-noise ratio of the FOTO signal, Bayesian inference for observer velocity, etc.).

master function around recombination. This can be computed at various redshifts by solving the underlying Einstein-Boltzmann equations and the specialized routines which can quickly integrate such equations for a given cosmological model are, naturally, called Einstein-Boltzmann Solvers. Some standard solvers currently in use by the community are `CAMB` (A. Lewis, Challinor and Lasenby, 2000), `CLASS` (Lesgourgues, 2011) and `DISCO-DJ` (Hahn, List and Porqueres, 2024) (along with their many EFT and modified gravity variants (Hu et al., 2014; Wang, 2024)). Other EB solvers, which are now out-dated and no longer maintained, include `CMBFAST` (Seljak and Zaldarriaga, 1999) and `CMBEASY` (Doran, 2005).

For studying the FOTO multipoles, we save 15 transfer function files corresponding to 15 redshift snapshots binned equidistantly in the scale factor ($a = 1/(1+z)$). The redshifts range from 0.0 to 1.8. These are then provided to `MonophonIC` which we configure to generate random particle positions in a box of length 7.5 Gpc/h tiled with 650^3 grid cells (thereby providing a grid resolution of 11.5 Mpc/h). Using the transfer function and a common seed for pseudorandom-number generation, `MonophonIC` instantiates 15 different catalogs of dark matter particle positions and velocities at each of the desired redshifts. These catalogs are saved in `.hdf5` files, which we convert to `GADGET2`-styled `.dat` binaries (Springel, 2005) using a python program for compatibility with `LIGER`'s I/O capability. This process is repeated using different random number seeds to generate 125 realizations of Newtonian cosmological evolution. The next step is to create a past-lightcone for an observer in the box and introduce relativistic distortions.

2.2.2 Light Cones in General Relativity (`LIGER`)

The LIghtcones with GEneral Relativity (`LIGER`)[10] method takes the progressive Newtonian snapshots from the previous step and stitches them together to form the past light cone of an observer. In this subsection, we present a brief sketch of the main computations that `LIGER` performs.

The first step is to translate the quantities defined in the N-body data to quantities required in the computation of the shift equations. Choosing to derive our analytic results in §1.4 in Poisson gauge really considerably simplifies the interpretation of the N-body output, which is generally presented in the synchronous comoving gauge. Quantities like position, velocity and potential can be directly equated between the two gauge choices and, hence, the Poisson equation can be written as

---

[10] See `LIGER` documentation: gitlab.com/cosmology-aifa/ligerv2

$$\nabla^2\varphi = \frac{3H_0^2\Omega_\mathrm{m}}{2a}\delta_\mathrm{SC}. \tag{2.46}$$

To compute the relativistic corrections, we need to know the value of potential and its first and second (spatial and temporal) derivatives everywhere in our simulation box. These are calculated by first computing overdensity fields using the CIC technique described in §2.1.4. Numerically, it involves (Elkhashab, Porciani and Bertacca, 2024)

$$\delta_\mathrm{sim}\left(\boldsymbol{x}_j, z_m\right) = \frac{1}{\bar{n}_\mathrm{sim}}\sum_i W_\mathrm{CIC}\left(\boldsymbol{x}_j - \boldsymbol{r}_i^m\right) - 1, \tag{2.47}$$

where $\bar{n}_\mathrm{sim} = N_\mathrm{sim}/V_\mathrm{sim}$ is the average particle density of the input simulation, the m in superscript and subscript indicates an association with the m^th snapshot and the discrete position vectors $\boldsymbol{x}_j$ represent grid cell coordinates. The Poisson equation is solved using the Faster Fourier Transform in the West[11] (FFTW) algorithm (Frigo and S. G. Johnson, 2005) . The spatial derivatives of the potential can also be solved in the Fourier space using spectral differentiation (Canuto, 2007) and the temporal derivatives are computed using standard Finite Difference Method. This provides us with all the terms required to compute the shifts as per Eq. (1.60).

While computing the coordinate transformations, we also need to integrate certain terms along the path of the photon to account for effects like late-time ISW and gravitational lensing. One could explicitly ray-trace photon geodesics from the source to the observer for every object on the light-cone but doing so would be wasteful. For two-point statistics, a demonstrably sufficient alternative to ray-tracing is the Born approximation (Ferlito et al., 2024). Accordingly, we compute the line-of-sight integrals along straight lines (as opposed the lensed null-geodesics) using the Fast Voxel Traverse (FVT) algorithm (Amanatides and Woo, 2023) that detects the cells in the simulation grid which are intersected by a particular LOS and sums up contributions to potential and its derivatives from those cells.

Another caveat in computing the line-of-sight integrals is that the limit of the integral is supposed to be the redshift space-position which is unknown prior to the computation of the shifts. This leads to a circularity[12]. Such problems arise often in computational physics and can generally be resolved by writing a code which relaxes the solution iteratively until convergence. In practice, one performs the following steps.

1. Compute the redshift position using *only* the local terms in the shift equations
2. Evaluate integral terms up-to the local-term shifted position from Step 1.
3. Apply integral shifts to the particle position

---

[11] See `FFTW` documentation: www.fftw.org

[12] This situation would constitute a ‘Catch-22’ in Joseph Heller’s sense, where each precondition blocks the other. In our case, one needs the redshift space position to compute the integrals but to compute the integrals one needs the redshift space positions

4. Repeat until convergence

Borzyszkowski, Bertacca and Porciani (2017) report that subsequent relaxation iterations do not lead to any significant change in the particle positions and that performing the aforementioned steps twice is sufficient. The integrals are only performed for those particles that have world-lines intersecting the past lightcone of a chosen observer in the simulation box. This ensures we compute shifts for only those particles which are visible to a given observer in the celestial sphere. Since we have a low resolution along the redshift axis (only 12 snapshots), `LIGER` uses a cubic interpolation to determine the value of the calculated quantities at the intersection point of the photon world-line and the observer lightcone.

The configuration file for `LIGER` in this study resembles the configuration used for `MUSIC2` i.e. a box size of 7500 Mpc/h with 650^3 grid cells. The observer is situated at the center of the box and has a peculiar velocity of $v_o = 369\,\mathrm{km\,s^{-1}}$ which is calibrated to the Planck measurement of the CMB dipole (Planck Collaboration et al., 2020). For each set of `MUSIC2` realization (i.e. snapshots sharing the same random seed but varying only in their redshifts), `LIGER` generates the following kinds of output catalogs (listed below with two naming conventions corresponding to the code and the formalism) with various effects 'switched on' progressively –

1. `real-space` ($\mathcal{R}$): No redshift space distortions are computed. The output only stitches together snapshots at various redshifts to detect which objects lie on an observer's past lightcone and should be visible in a hypothetical survey.

2. `vRSD` ($\mathcal{V}$): Only redshift space distortions arising from radial peculiar velocity components are computed and the particles on the past lightcone are shifted accordingly.

3. `vRSD_obs`: Same as `vRSD` but observer's motion is also considered while calculating the Doppler shifts.

4. `GRRSD` ($\mathcal{G}$): The entire suite of general relativistic redshift space distortions are computed including effects arising from lensing and ISW. However, the observer is considered to be at rest with respect to the CMB frame.

5. `GRRSD_obs` ($\mathcal{O}$): The complete suite of general relativistic redshift space distortions for an arbitrarily moving observer. This is the closest representative of the observed galactic over-density at linear order.

In later sections, we will occasionally use the calligraphy letters $\mathcal{G}$ and $\mathcal{O}$ to represent `GRRSD` and `GRRSD_obs` catalogs respectively. For example, $P^{\mathcal{G}}$ and $P^{\mathcal{O}}$ can represent the power spectrum for cosmic rest frame and observer rest frame respectively (with $\Delta P \equiv P^{\mathcal{O}} - P^{\mathcal{G}}$ representing the FOTO signal).

2.2.3 `Buildcone` Routine

It is both a convenient and an inconvenient feature of the ΛCDM model that baryons (the ordinary matter, well understood from gauge theoretic perspective) contribute only a small amount to the large scale gravitational dynamics of the universe. It is convenient because the regions where baryonic effects become relevant, we need to involve further sophistication in our models, taking into account multi-physics effects arising from the complex feedback of thermal and chemical dynamics (Vogelsberger, Marinacci et al., 2019; Vogelsberger, Genel et al., 2014; Schaye et al., 2023). A negligible baryonic contribution on the LSS affords us the liberty to ignore these additional complications and focus primarily on the dynamics of a gravitating but otherwise non-interacting component i.e. Dark Matter. It is inconvenient, however, because the dominant matter component in cosmological physics is currently impenetrable to direct observational or experimental probing. The galaxy biasing procedures (Desjacques, Jeong and Schmidt, 2018) aim to model and understand the connection that allows inferences to travel from observations of luminous baryonic tracers to the underlying dark matter distribution — not entirely unlike the usage of polystyrene beads to image velocity fields of surface waves in liquids (Roux, Meunier and Mari, 2023).

To perform ‘Baryon Painting’ (i.e. post-processing DM data to capture the net effects of baryons), we use the `Buildcone` (BC) routine (Borzyszkowski, Bertacca and Porciani, 2017). To understand this procedure, we re-write Eq. (1.80) as

$$\delta_{\mathrm{g,\,s}} = (b-1)\delta_{\mathrm{SC}} + \delta_{\mathrm{s}} + \mathcal{E}\delta\ln a + \mathcal{Q}(\mathcal{M}-1) \tag{2.48}$$

where δ_{SC} is the overdensity in the simulation gauge (i.e. `MUSIC2` output) and we define

$$\begin{aligned}\delta_{\mathrm{s}} \equiv \delta_{\mathrm{SC}} &+ \left(\frac{\partial_0\mathcal{H}}{\mathcal{H}^2} + \frac{2c}{x\mathcal{H}}\right)\delta\ln a + \phi_{\mathrm{e}} - 2\psi_{\mathrm{e}} + \frac{(\partial_0\phi)_{\mathrm{e}}}{\mathcal{H}} + 3\mathcal{H}\phi_v \\ &- \frac{1}{\mathcal{H}}\left[n^i\partial_i\left(n^j v_j\right)\right]_{\mathrm{e}} + \frac{2}{x}\int_0^x(\phi+\psi)\mathrm{d}\tilde{x} - 2\kappa.\end{aligned} \tag{2.49}$$

We assume that the redshift dependence of linear bias b, magnification bias $\mathcal{Q}$ and evolution bias $\mathcal{E}$ are defined by the survey and, henceforth, collectively refer to them as *survey functions*. The remaining terms in the Eq. (2.48) (δ_{SC}, δ_{s}, $\delta\ln a$ and $\mathcal{M}$), can be constructed from the `LIGER` and `MUSIC2` output. The next step, then, is to compute a galaxy number density field that enforces the overdensity from Eq. (2.48) at each cell center by evaluating

$$n_{\mathrm{g},s}\left(\boldsymbol{x}_j\right) = \bar{n}_{\mathrm{g,\,s}}\left(\boldsymbol{x}_j\right)\left[1 + \delta_{\mathrm{g},s}\left(\boldsymbol{x}_j\right)\right], \tag{2.50}$$

where $\bar{n}_{\mathrm{g,s}}$ is the average background comoving number density of the survey. Finally, when we estimate the power spectra, we randomly scatter as many objects around each grid point inside the associated cell, as prescribed by Eq. (2.50) to subdue the artificial grid-like structure of our output data.

Survey Functions

In this study, we utilize survey functions for two different kinds of surveys. First, we consider the futuristic Square Kilometer Array Observatory (called SKAO2) that uses HI as its primary baryonic tracer. Second, we consider a Euclid-like survey for deeper redshift bins using Hα tracers. These survey functions are adopted from Maartens et al. (2021) and plotted in Fig. 2.6.

The predicted survey functions for Euclid Wide Spectroscopic Survey come from Model 3 of Pozzetti et al. (2016) where a population of Hα tracers is characterized by a redshift dependent

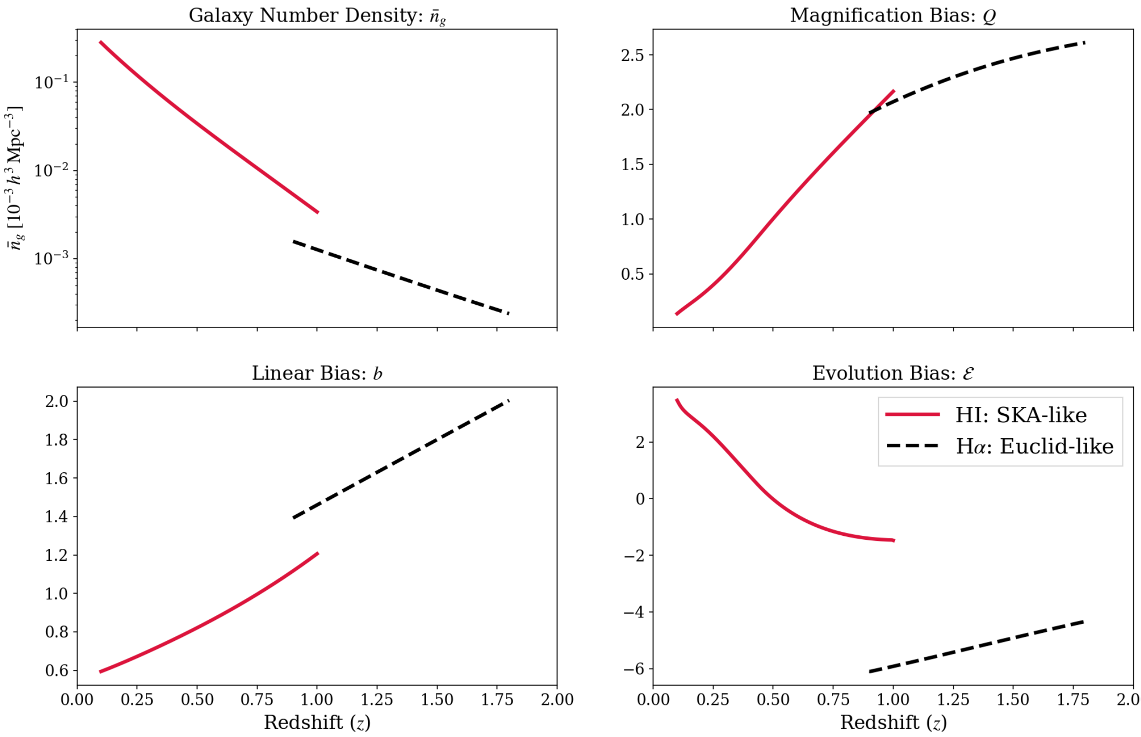

Figure 2.6: Survey functions for SKAO2-like and Euclid-like surveys plotted according to the prescription by Maartens et al. (2021). These functions, with the exception of the evolution bias $\mathcal{E}$ for HI tracers, are used to create mock galaxy catalogs. The evolution bias for HI tracers fails self-consistency test and, hence, a differently calibrated function is utilized for the final mocks.

luminosity function

$$\Theta(L,z)\,dL = 10^{-2.7}\left(\frac{L}{L_*}\right)^{-1.4}\exp\left[-\frac{L}{L_*(z)}\right]\frac{dL}{L_*(z)} \tag{2.51}$$

where

$$\log_{10}\left[\frac{L_*(z)}{42.6}\right] = -c(z-2.2)^2. \tag{2.52}$$

Thus, the average number density of tracers for a flux-limited survey becomes

$$\bar{n}_{g,s}(x) = \int_{L_{\mathrm{min}}(x)}^{\infty}\Theta(x,L)\,\mathrm{d}L, \tag{2.53}$$

with $L_{\mathrm{min}}(x) = 4\pi D_L^2(x)F_{\mathrm{lim}}$ and $F_{\mathrm{lim}} = 2\times10^{16}$ erg cm^{-2} s^{-1}. The magnification bias and evolution bias can be computed using their definitions

$$Q(z) = -\frac{L_{\mathrm{min}}}{\bar{n}_g(z)}\left.\frac{\partial\bar{n}_g}{\partial L_{\mathrm{min}}}\right|_{L_{\mathrm{min}}=L_{\mathrm{lim}}(z)} = \frac{L_{\mathrm{lim}}(z)\,\Theta(L_{\mathrm{lim}}(z),z)}{\bar{n}_g(z)} \tag{2.54}$$

and

$$\begin{aligned}\mathcal{E}(z) &= -\frac{\partial \ln \int_{L_{\rm min}}^{\infty} \Theta(L,z)\, dL}{\partial \ln(1+z)}\bigg|_{L_{\rm min}=L_{\rm lim}(z)} \\ &= -\frac{1}{\bar{n}_g(z)} \int_{L_{\rm lim}(z)}^{\infty} \frac{\partial \Theta(L,z)}{\partial \ln(1+z)}\, dL\,.\end{aligned} \tag{2.55}$$

Finally, for linear bias, we use

$$b(z) = 1.46 + 0.68(z-1). \tag{2.56}$$

In case of an SKA-like survey, with HI tracers, we begin by modeling the noise associated with a flux density measurement of an interferometer (Maartens et al., 2021)

$$S_{\rm rms}(\nu) = \frac{2 k_B T_{\rm sys}(\nu)}{A_{\rm eff} N_d \sqrt{2 t_p(\nu)\, \delta\nu}}, \tag{2.57}$$

where $\nu = \nu_{21}/(1+z)$ with $\nu_{21} = 1420$ MHz, $N_d = 70,000$ is the number of dishes, system temperature $T_{\rm sys}$ (instrument + sky) is modeled as

$$T_{\rm sys} = T_{\rm rec} + 60 \left(\frac{\nu}{300\ \rm MHz}\right)^{-2.5}\ \rm K \tag{2.58}$$

with $T_{\rm rec} = 15$ K, $A_{\rm eff} = 0.8 \times (\pi/4) D_d^2$ is the effective area (with 0.8 representing aperture efficiency), and $\delta\nu = 10^3$ Hz is the system channel width. The time per pointing,

$$t_p = t_{\rm tot} \frac{\theta_b^2}{\Omega_{\rm sky}}, \tag{2.59}$$

depends on the total integration time $t_{\rm tot} = 3.6 \times 10^7$ s, the total survey area $\Omega_{\rm sky} = 30000\ \rm deg^2$ and the effective primary beam (field of view) from the mosaicked sky (Santos et al., 2015)

$$\theta_b^2 = \frac{\pi}{8} \left[1.3 \times \frac{\lambda_{21}(1+z)}{D_d}\right]^2, \tag{2.60}$$

where $D_d = 3.1$ m is the dish diameter and $\lambda_{21} = 21$ cm is the rest frame wavelength of the target transition. With these quantities defined, we can write the detection limit as

$$S_c(z) = S_{\rm rms}(z) \frac{N_{\rm cut}}{10} \tag{2.61}$$

where $N_{\rm cut}\sigma$ represents a detection threshold with the parameter set to $N_{\rm cut} = 10$ for futuristic SKAO2 like survey. This allows us to compute the total number count of objects that are expected to be detected which Yahya et al. (2015) present as a fitting formula,

$$n_g(z, S_c) = 10^{c_1(S_c)} z^{c_2(S_c)} \exp(-c_3(S_c) z)\ \rm deg^{-2} \tag{2.62}$$

with coefficients c_i given in Table 3 of (Yahya et al., 2015). This number density is provided in per

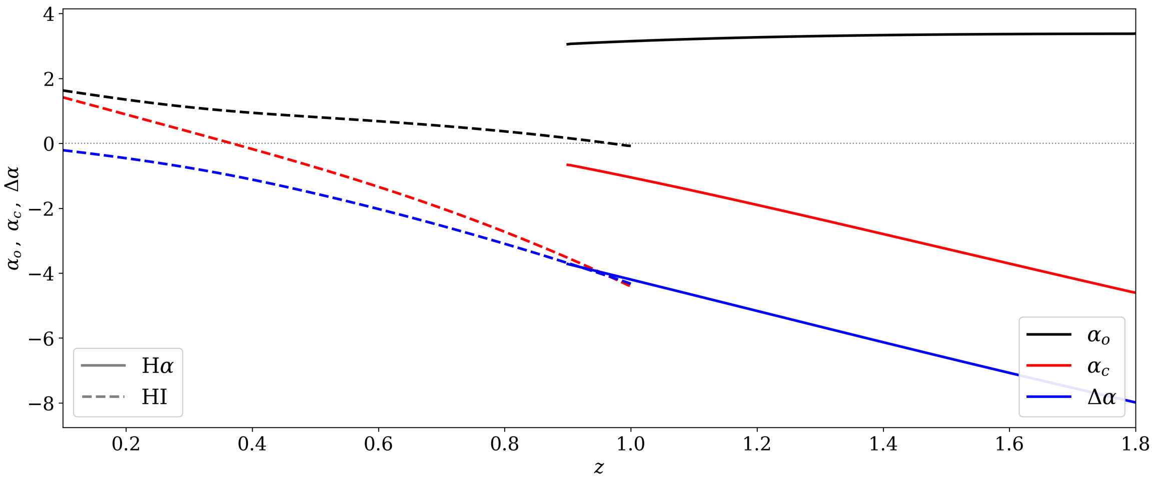

Figure 2.7: The classical and observed values of α computed for Euclid-like and SKA-like survey functions over a range of redshifts. This figure suggests that the amplitude of the FOTO signal should be higher for Euclid like mocks. This observation is verified in the results discussed in the next chapter.

degree squared and can easily be converted into per cubic mega parsec. Based on this number density of tracers, we can again compute evolution and magnification bias via the derivatives discussed earlier. Lastly, for linear bias of SKAO2, we use a function of the form

$$b(z) = c_4(S_{\rm rms}(z)) \times \exp\left(z c_5(S_{\rm rms}(z)\right) \tag{2.63}$$

with the coefficients from the same Table 3 of Yahya et al. (2015) as earlier. Fig. 2.6 provides a summary of all the survey functions for Hα and HI survey types.

Using these sets of survey functions, we can also evaluate the redshift evolution of $\alpha_{\rm c}$, $\alpha_{\rm o}$ and $\Delta\alpha$ (introduced in §1.4) that regulate the amplitude of the FOTO fluctuations. On the basis of Eq. (1.89), Eq. (1.91) and Eq. (1.95), we have computed the evolution of alpha for both Euclid-like and SKA-like survey functions. These results are presented in Fig. 2.7, on the basis of which we anticipate a greater FOTO amplitude for Euclid-like mocks with a less steep redshift dependence compared to SKA-like mocks. These predictions would be validated by the measurements in §3.1.

Consistency Check

Before performing any measurements or forecasts, it is important to consider the internal self-consistency of these survey functions. From the definition of the evolution and magnification bias, we can write (Maartens et al., 2021)

$$\begin{aligned}\frac{\mathrm{d}\ln \bar{n}_g(z)}{\mathrm{d}\ln(1+z)} &= \frac{1}{\bar{n}_g(z)}\frac{\mathrm{d}\bar{n}_g(z)}{\mathrm{d}\ln(1+z)} \\ &= 2Q(z)\left[\frac{\mathrm{d}\ln L_{\rm lim}}{\mathrm{d}\ln(1+z)}\right] + \mathcal{E}(z) \\ &= 2Q(z)\left[1 + \frac{c(1+z)}{H(z)x(z)}\right] + \mathcal{E}(z).\end{aligned} \tag{2.64}$$

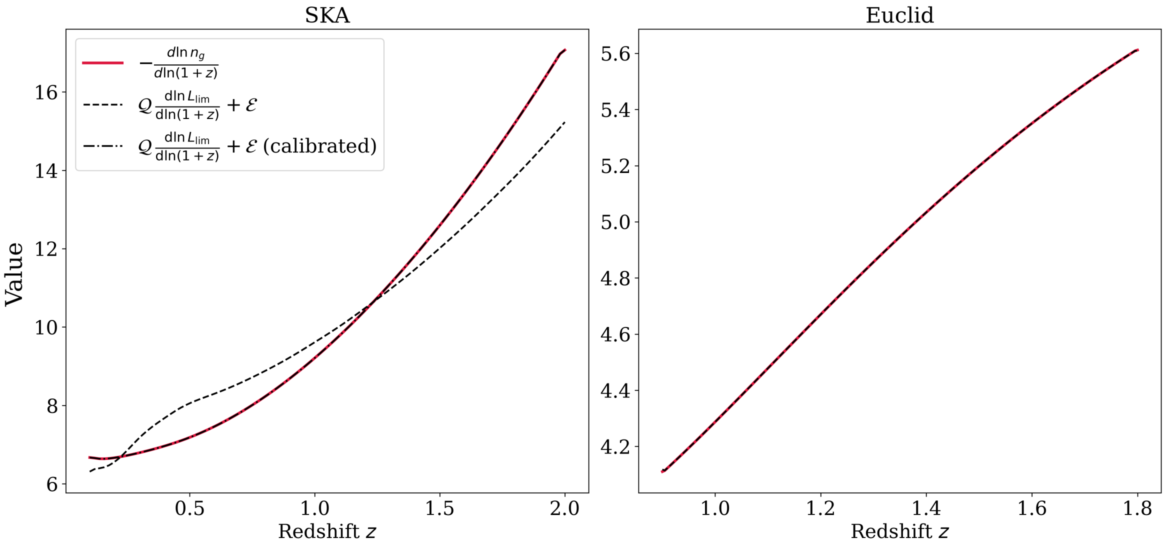

Figure 2.8: Testing the self-consistency of the survey functions prescribed by (Maartens et al., 2021) based on the Eq. (2.64). While the Euclid survey functions are self-consistent, the SKAO2 survey functions fail to satisfy this consistency check. Thus, we modify the evolution bias by calibrating it with respect to the LHS of Eq. (2.64) for our further analysis.

We can compute the LHS and RHS of Eq. (2.64) independently using the survey functions. Ideally, the results from the two methods should coincide. However, on testing for this self-consistency condition, we find that Euclid survey functions pass the consistency test but the SKA survey function described in (Maartens et al., 2021) fails to satisfy this condition. Thus, for our later analysis, we implement a prescription of (Maartens et al., 2021) only after altering the evolution bias for SKA such that it satisfies the consistency condition in Eq. (2.64) is satisfied (see Fig. 2.8). [13]

Next, we also check for the cross-consistency of the number density provided to `Buildcone` via the survey functions and the number density of the sources in `Buildcone`'s output. This consistency check is displayed in Fig. 2.9 for the two sets of survey functions mentioned in this work. As we see, `Buildcone` faithfully implements the provided input number density for our choice of runtime configuration.

The workflow described in this section — of generating Newtonian snapshots using Boltzmann solvers, adding relativistic corrections using perturbative shifts and painting baryons on dark matter distribution — yield the mock skies on which our Yamamoto-Bianchi estimator from §2.1.2 can be applied and using which the FOTO multipole results of §. 2.1.3 can be studied. The verdict on the detectability of the multipoles in various surveys is quantified in the forms of likelihoods and covariances in §3.1.

---

[13] It is important to note here that predicting survey functions is a delicate and challenging affair, over which the best practice is to exercise cautious uncertainty. We shall discuss this again in §3.3.2.

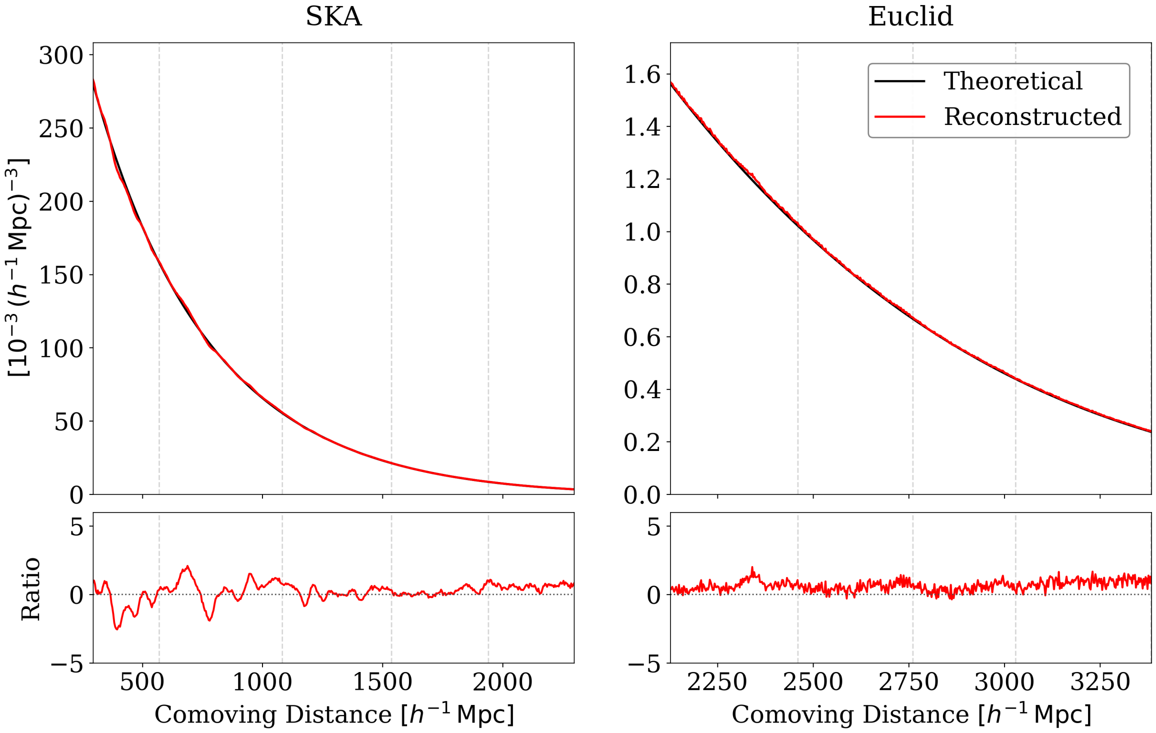

Figure 2.9: Comparing the number density provided to `Buildcone` via input survey functions with the number density reconstructed from the output catalogs. For both survey types, our baryon painting procedure faithfully reproduces the theoretical inputs. Vertical gray lines in the figure represent the tomographic redshift bins considered in Fig. 3.1 and Fig. 3.2. The reason why the fluctuations appear to have higher frequency for Hα is that the redshift histograms were binned in equal sizes of redshift but are plotted in units of comoving distance.

CHAPTER 3

Results

3.1 Comparing FOTO Measurements

Through Chapters 1 and 2, we assembled the formalism which facilitates both the modeling and estimation of the multipole of FOTO signal. Let us now discuss the results of such an exercise. Beyond checking for internal consistency of the code, these measurements would also convey useful statistical information in the form of Frequentist signal-to-noise ratios (§3.1.1) and Bayesian inference posteriors (§3.1.2).

First, we measure the FOTO signal across various tomographic redshift bins. During power spectra estimation, we embed the catalog objects in a box of size $L_{\rm FFT} = 2 \times 10^4$ Mpc/h. This is to ensure that the fundamental mode of the box, which determines the largest measurable scales, remain small enough for our use case i.e. $k_f = 2\pi/L_{\rm FFT} = 0.3 \times 10^{-3}\, h\,{\rm Mpc}^{-1}$. The results of FOTO measurements for these bins for HI and Hα survey are shown in Fig. 3.1 and Fig. 3.2 respectively. In both images, the solid red line corresponds to the mean measurement across all realizations and the black dotted curve represents the analytic model for FOTO signal. The noticeable agreement between mean and model curves confirm that the analytic predictions match very well with the mock estimates for both surveys, across all redshift bins and multipole orders. While the FOTO amplitude drops sharply for HI survey type at higher redshifts, Hα tracers carry a clear signal even in that farther redshift bins. We also note that for Hα tracers the higher multipoles maintain noticeable oscillations at smaller length scales (i.e. larger values of k) even though the monopole signal is sharply suppressed on those scales.

From looking at the form of Eq. (1.4), we can see that the FOTO amplitude is integrated over the redshift range (as opposed to being averaged over it). Thus, insofar as α remains positive, the signal would be more pronounced for wider redshift bins. Having shown the detectability of the FOTO signal across these tomographic bins, we now define a wide bin over the entire of range of the survey functions. From Fig. 2.7, we see that Euclid-like survey functions yield a consistently higher α (and, consequently, higher FOTO amplitude) compared to SKA-like survey functions, despite the latter survey type having a tracer number density that is orders of magnitude higher than the former. Furthermore, a higher particle count can substantially bottleneck the power spectra estimation pipeline during the density mesh creation and, especially, in the random catalog generation. Therefore, SKA measurements, for our purpose, are both weaker and more resource demanding. Noting the distinct advantage in doing the following, for the remainder of our analysis, we shall restrict our attention to the FOTO estimation in the widest redshift bin of $z \in (0.9, 1.8)$ of Euclid-like mocks. The results

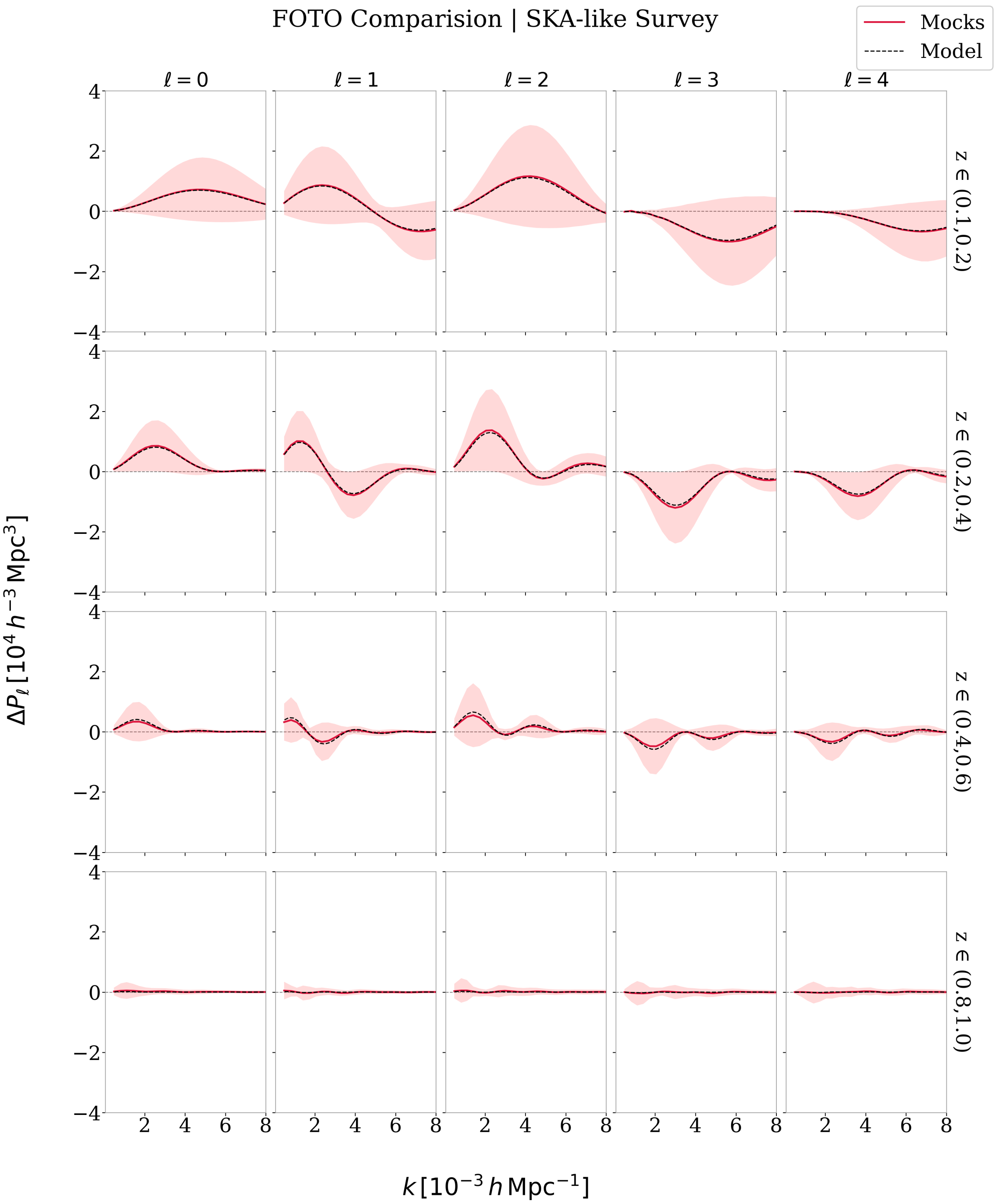

Figure 3.1: Finger-of-the-Observer effect across various redshift bins and multipole orders for an HI type redshift survey. The various panels demonstrate that the mean of mock measurements agree very well with the model predictions. For this specific choice of survey functions, the FOTO signal decays quickly with increasing redshift. The red shaded region represents 1σ scatter of the FOTO measurement across different realizations.

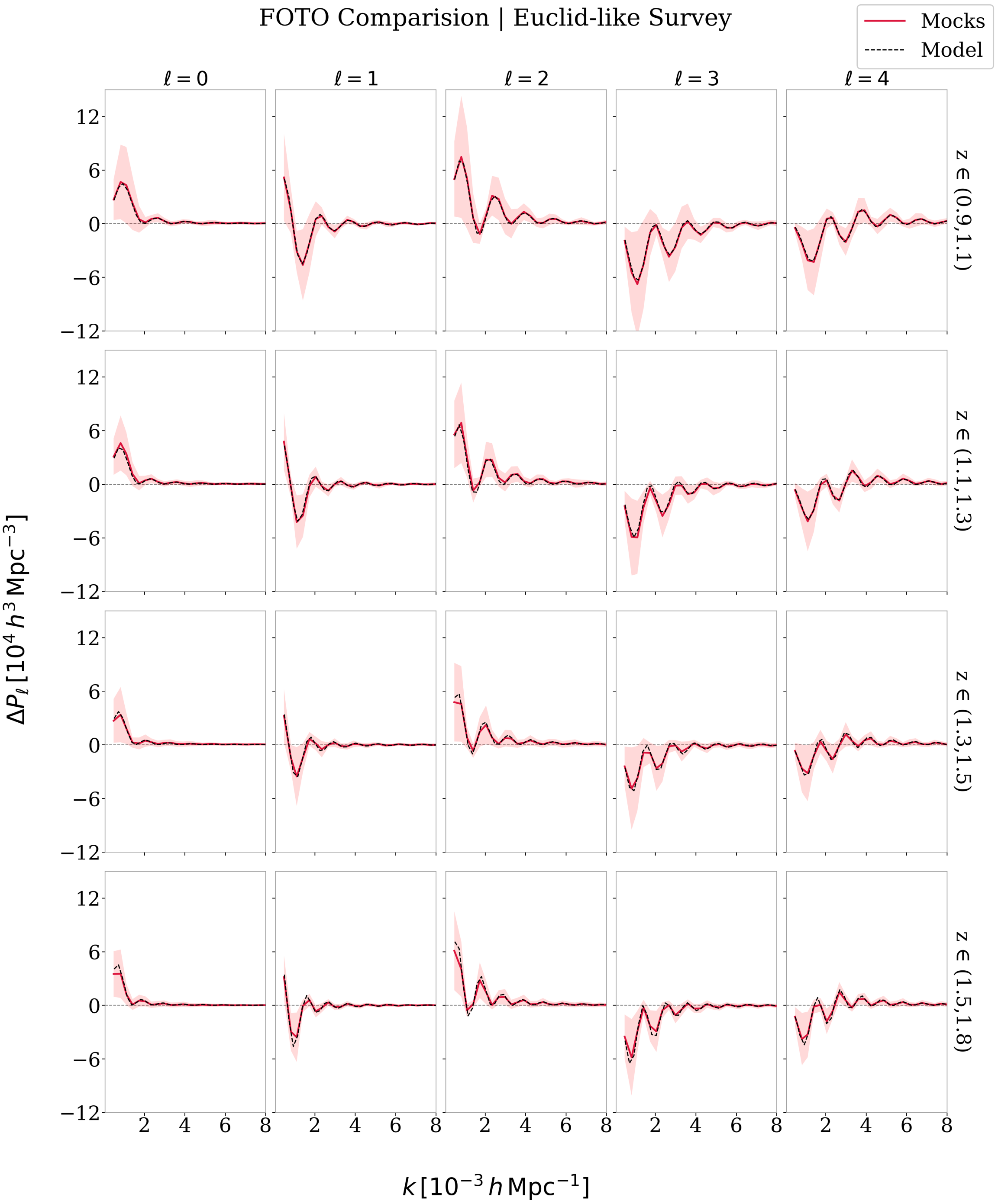

Figure 3.2: Similar to Fig. 3.1 but for Hα survey type. Here, again, the measurements provide excellent agreement with the model. Notably, the FOTO amplitude is higher than HI survey functions and remains noticeable even in farther redshift bins. The oscillations happen at a higher frequency and higher multipoles survive even at smaller scales where the monopole signal is dampened.

of these measurements are shown in Fig. 3.3. We conclude this section by re-emphasizing that our results in this section clearly demonstrate that the multipoles of FOTO signal can be satisfactorily modelled and measured in the considered mock skies.

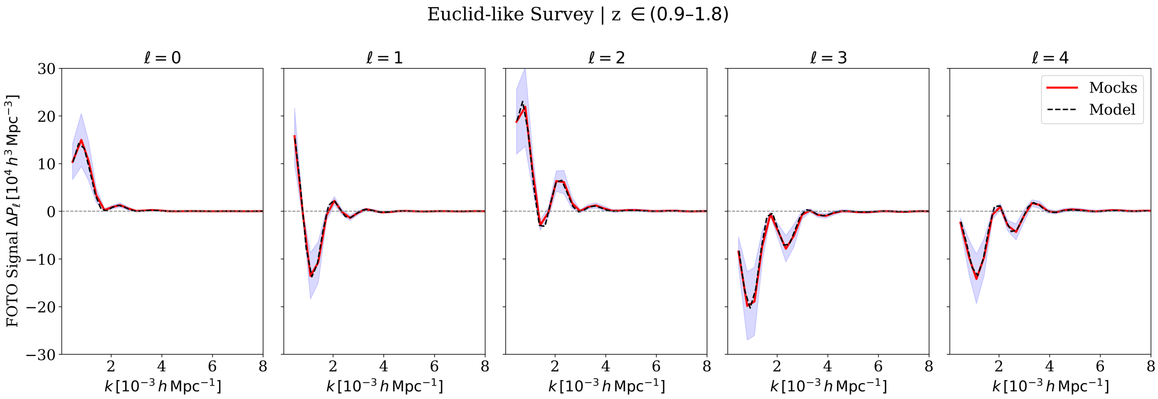

Figure 3.3: FOTO multipole measurements for widest Euclid bin allowed by our survey functions i.e. $z \in (0.9, 1.8)$. This is the highest amplitude for the FOTO signal that we can achieve with the smallest scatter across various configurations. Thus, for the remainder of our statistical analysis, we will use the power spectrum measurements of this redshift bin.

3.1.1 Signal-to-Noise Ratio

Given our measurements of the power spectrum in the relativistic mocks, we can try to quantify whether the presence of the FOTO oscillations can in-principle be distinguished from a null-hypothesis positing random fluctuations. One way of doing so would be to compute the ‘size’ of the FOTO effect, called the signal-to-noise ratio (SNR), which is the first of the five MAGIC[1] criteria for a statistically principled argument (Abelson, 1995). Before moving towards a discussion of the FOTO signal in a Bayesian framework and its role in velocity inference, let us study the impact of the higher multipoles from a Frequentist framework and compute the SNR using systematically enumerated combinations of FOTO multipoles.

A powerful method for estimating the SNR originates from Neyman-Pearson lemma[2], that demonstrates that a ratio of likelihoods can be the most powerful statistical test in certain contexts. If we want to distinguish between a null hypothesis H_0 (no FOTO contribution to the power spectrum) and an alternative H_1 (FOTO contribution present in the signal), then an optimal test statistic to compute SNR is the ratio λ of their likelihoods,

$$\lambda_i = 2 \ln \frac{\mathcal{L}(M_{\mathcal{G}} | \boldsymbol{D_i}^{O})}{\mathcal{L}(M_O | \boldsymbol{D_i}^{O})}, \tag{3.1}$$

---

[1] MAGIC is an acronym that stands for the criteria for making a compelling case with statistics that Robert Abelson proposed in his book *Statistics as Principled Arguments* (Abelson, 1995). The various letters in MAGIC stand for – Magnitude (how big is the effect), Articulation (how specific is the effect), Generality (how generally it applies), Interestingness (can the effect change people’s beliefs on something important) and Credibility (what evidence is cited).

[2] Interestingly, Jerzy Splawa Neyman (the former of the Neyman-Pearson pair) was a Polish statistician whose writings introduced and popularized the modern concept of a confidence interval (Neyman, Scott and Shane, 1956).

where the function $\mathcal{L}$ represents the likelihood of a model $M_{\mathcal{G}}$ (the prediction of a clustering statistic for an observer at rest with CMB) and a model $M_{\mathcal{O}}$ (prediction of a clustering statistic for an observer moving with our peculiar velocity), given the n-dimensional data vector containing a single measurement of the clustering statistic of choice (i.e. the multipoles of the Yamamoto-Bianchi estimator of the late universe 1D power spectrum). The likelihoods can be computed using the mean signal $\boldsymbol{\mu}$ and covariance matrix $\boldsymbol{C}$ of the power spectrum measurements of catalogs $\mathcal{O}$ and $\mathcal{G}$. These statistics are defined in their usual form,

$$\boldsymbol{\mu}_a = \mathbb{E}[\boldsymbol{D}_i^a], \tag{3.2}$$

$$\boldsymbol{C}_a = \mathbb{E}[(\boldsymbol{D}_i^a - \boldsymbol{\mu}_a)(\boldsymbol{D}_i^a - \boldsymbol{\mu}_a)^T], \tag{3.3}$$

for $a = \mathcal{G}$ or $a = \mathcal{O}$. Assuming Gaussian errors, the likelihood of the dataset $\boldsymbol{D}$ being drawn from model M with a signal $\boldsymbol{\mu}$ can be written as

$$\mathcal{L}(M_a\,|\boldsymbol{D}_i^{\mathcal{O}}) \propto \frac{\exp\left\{\left(-\frac{1}{2}(\boldsymbol{D}_i^{\mathcal{O}} - \boldsymbol{\mu}_a\right)^T \boldsymbol{C}_a^{-1}\left(\boldsymbol{D}_i^{\mathcal{O}} - \boldsymbol{\mu}_a\right)\right\}}{(2\pi)^{n/2}\sqrt{\det(\boldsymbol{C}_a)}}. \tag{3.4}$$

Note that the likelihood defined for computing the Frequentist SNR is subtly different in its form from the likelihood we will define during the Bayesian inference in Eq. (3.5). At this stage, we are neither computing any analytic predictions for the models of $M_{\mathcal{G}}$ or $M_{\mathcal{O}}$ nor fitting for any model parameters $\boldsymbol{\theta}$. Instead, the model here is simply an ensemble of measurements of the clustering statistic S estimated using mocks which all share a fixed value of cosmological parameters (including observer velocity) and are characterized by their mean and covariance.

When we compute the distribution of likelihood ratios for the null and alternate hypothesis we get two distributions $P(\lambda\,|H_0)$ and $P(\lambda\,|H_1)$ respectively and the distance between the peaks of these distributions corresponds to signal-to-noise of the FOTO effect on the 1D matter power spectrum. These distributions have been displayed in Fig. 3.4 for monopole-only and all-multipole cases[3]. We now fit Gaussian curves to the distributions of these likelihood ratios to estimate the locations of and distance between the two peaks. It is customary to express this distance in the units of the standard deviation of the distributions in order to express the SNR in more data-motivated units. This, however, presents us with a few options in how we wish to interpret the SNR of our clustering statistics.

In a highly idealized setting, one can posit that the standard deviation of $P_\ell^{\mathcal{O}}$ and $P_\ell^{\mathcal{G}}$ are similarly sized and, thus, the distance between the peaks of $P(\lambda\,|H_0)$ and $P(\lambda\,|H_1)$ can be expressed in terms of either $\sigma_{\mathcal{O}}$ or $\sigma_{\mathcal{G}}$ without any major difference. For instance, Elkhashab, Bertacca et al. (2024) find this to be the case in their analysis of the correlation function for $\mathcal{O}$ and $\mathcal{G}$ type mocks. However, in our study we find that the power spectrum multipoles for $\mathcal{O}$ type mocks display a much larger scatter than power spectrum of $\mathcal{G}$ type mocks. Consequently, the scatter of likelihood ratios substantially differ for null and alternate hypothesis. In such a case, the formal prescription is to use a combination of the estimates of both standard deviations $\sqrt{\sigma_{\mathcal{O}}^2 + \sigma_{\mathcal{G}}^2}$. An alternate approach towards expressing the SNR could instead be to assert that in practice we would only observe clustering statistics of $\mathcal{O}$

---

[3] We already note that the distribution of $\lambda_{\mathcal{G}}$ for the monopole-only case and the distribution of $\lambda_{\mathcal{O}}$ in all multipoles case are not very Gaussian. In the absence of particular systematics, increasing the number of realizations should enhance the Gaussianity of these likelihood ratio distributions.

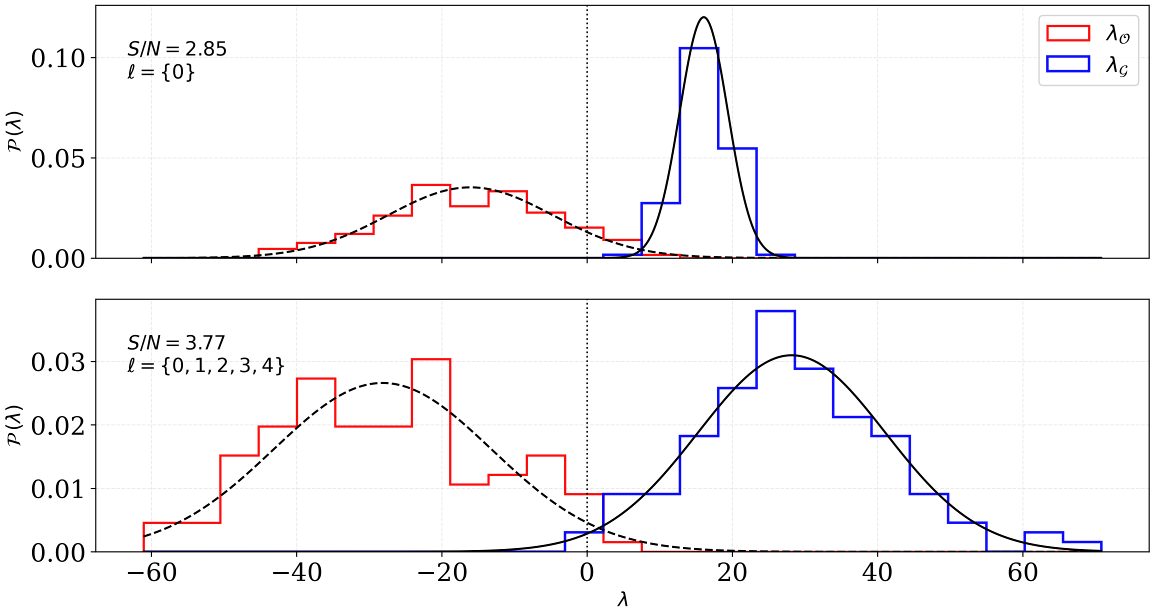

Figure 3.4: Comparing the likelihood ratios for the null hypothesis (Blue) of being at rest with the CMB frame and the alternate hypothesis of observing FOTO effect (red) as computed for monopole-only and all-multipoles cases. The figure suggests an increase in the SNR when higher multipole orders are considered for the null test. The distance between the peaks of the histogram is expressed in terms of the standard deviation of $\lambda_{\mathcal{O}}$.

type mocks (because we cannot turn-off the observer velocity relativistic effects in our data) and, thus, the statistical information we compute should primarily be on the basis of $\boldsymbol{C}_{\mathcal{O}}$ and $\sigma_{\mathcal{O}}$. For both our Frequentist and Bayesian analysis, we will follow this principle and use only $\boldsymbol{C}_{\mathcal{O}}$ to compute the likelihood. In this section, however, we present the results using all three conventions for defining the distance between peaks of likelihood ratios i.e. using $\sigma_{\mathcal{O}}, \sigma_{\mathcal{G}}$ and $\sqrt{\sigma_{\mathcal{O}}^2 + \sigma_{\mathcal{G}}^2}$. The reason for presenting results from all three cases in Fig. 3.5 is to highlight the difference that choosing particular conventions can lead to in terms of interpreting which combinations of the multipoles contain the least and the highest SNR. When using only $\sigma_{\mathcal{O}}$, the SNR is highest when we use all multipoles together and enhances the monopole-only case of SNR = 2.8 to an SNR = 3.8 (yielding an improvement of over 30%, which is what we would observe while studying the posterior widths in §3.1.2 and Fig. 3.7). Since the scatter in the clustering statistics of $\mathcal{G}$ type mocks is lower, using $\sigma_{\mathcal{G}}$ yields higher numerical values for SNR but the trend reverses in comparison with the previous case. This could be because, in absence of the FOTO signal, concatenating higher power spectrum multipoles for $\mathcal{G}$ may only serve to increase the scatter. Lastly, notice that the top performing configuration changes from the all-multipoles case for units of $\sigma_{\mathcal{O}}$ to a particular triple when using the units of $\sqrt{\sigma_{\mathcal{O}}^2 + \sigma_{\mathcal{G}}^2}$.

3.1.2 Bayesian Inference

While SNR is an indicative statistic, the dependence of the SNR-maximising combination on the convention of which σ we use to define it indicates a limitation of the Frequentist approach for our use case. A more decisive test for a signal's usefulness is the extent to which it allows an inference

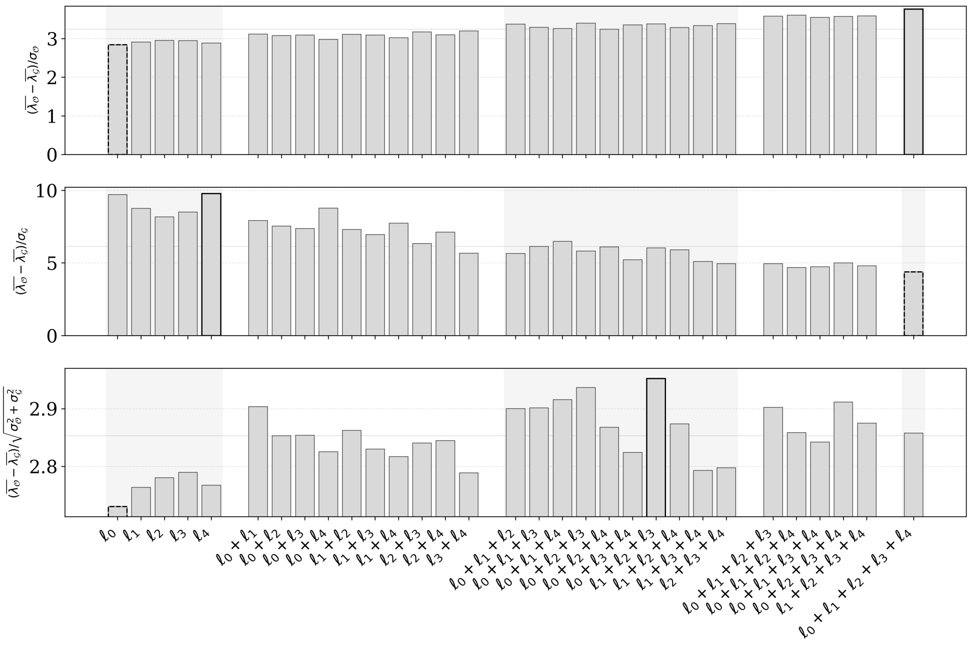

Figure 3.5: Comparing SNR computed using all combinations of the first five power spectrum multipoles of the null hypothesis (CMB rest frame) and the alternate hypothesis (peculiar velocity's FOTO signal). Different conventions for defining the distance between the peaks of the likelihood ratio distributions lead to different choices for the top-performing multipole combination. The solid and dashed frames represent the highest and lowest signal-to-noise achieved within each convention.

of constraints on model parameter. A common practice for performing such inference, not just in cosmology but across sciences in general, is to employ the Bayesian framework of conditional probabilities (Toussaint, 2011).

Bayesian formalism, broadly speaking, prescribes a grammar for quantifying how prior beliefs concerning a claim must be updated in light of some evidence. In Bayesian formalism, one speaks of the constraining power of a given data likelihood $\mathcal{P}(\boldsymbol{d} \mid \boldsymbol{\theta})$ to describe how much it can shift and squeeze the *a priori* probability distribution $\mathcal{P}(\boldsymbol{\theta})$ over a parameter space into an *a posteriori* distribution $\mathcal{P}(\boldsymbol{\theta} \mid \boldsymbol{d})$ over the same parameter space. Assuming gaussian errors, the data likelihood can be computed as

$$\mathcal{P}(\boldsymbol{d} \mid \boldsymbol{\theta}) \propto \frac{\exp\left\{-\frac{1}{2}[\boldsymbol{d} - \boldsymbol{m}(\boldsymbol{\theta})]^T \boldsymbol{C}^{-1} [\boldsymbol{d} - \boldsymbol{m}(\boldsymbol{\theta})]\right\}}{(2\pi)^{n/2}\sqrt{\det \boldsymbol{C}}} \tag{3.5}$$

where $\boldsymbol{d}$ is a n-dimensional data vector, $\boldsymbol{m}$ is a model dependent on a set of parameters $\boldsymbol{\theta}$ and $\boldsymbol{C}$ is the covariance matrix. For our likelihood calculation, we use $\boldsymbol{d} \equiv P_O - \bar{P}_G$ as our data vector and the covariance matrix is $\mathbf{C}_O$. The reason for this choice, as described earlier, is that in practice we can only ever observe the data vector for O type catalogs. We do not have empirical access to what the large scale structure would look like if some of the relativistic effects were 'turned off'. To use the higher multipoles of the power spectrum for inference, we simply concatenate the various multipoles into a single one-dimensional data vector and use that to compute the likelihood.

The likelihood, posterior and prior distributions are related to each other via the Bayesian formula of conditional probabilities

$$\mathcal{P}(\boldsymbol{\theta} \mid \boldsymbol{d}) = \frac{\mathcal{P}(\boldsymbol{d} \mid \boldsymbol{\theta})\mathcal{P}(\boldsymbol{\theta})}{\mathcal{P}(\boldsymbol{d})} \tag{3.6}$$

were $\mathcal{P}(\boldsymbol{d})$ can be ignored because it is a normalization factor common across all choices of parameters and can be easily marginalized over.

To compute the posterior distribution, we must integrate the likelihood over the relevant span of the parameter space. In practice, however, integrating over the parameter space can become extremely resource demanding (especially for high dimensional parameter spaces). Thus, a standard optimization technique is to efficiently sample points from those regions of the parameter space which contribute the most to the posterior. To do so, an array of Monte-Carlo walkers can be setup to explore the parameter space stochastically but nudged by an underling Markov chain process that rewards steps in directions that improve the fit (Brooks et al., 2011). In our analysis, we use a library called `emcee`[4] (Foreman-Mackey et al., 2013) for handling the Monte Carlo Markov Chains (MCMC) and it is based on a family of MCMC methods invariant under affine transformations (Goodman and Weare, 2010).

The choice of priors can often become a contentious topic but, insofar as it can be shown that reasonable changes to priors leave the posterior undisturbed, the prior distribution does not matter much. Nevertheless, numerical simulations of ΛCDM show that dark matter halos with fixed mass and local environment densities follow a Maxwellian velocity distribution(Dam, G. F. Lewis and Brewer, 2023; Sheth and Diaferio, 2001),

$$\mathcal{P}(v_\odot) = \sqrt{\frac{2}{\pi}}\frac{v_\odot^2}{\sigma^3}\exp\left(-\frac{v_\odot^2}{2\sigma^2}\right), \tag{3.7}$$

here we set $\sigma = 300\,\mathrm{km\,s^{-1}}$. For velocity inference using the FOTO signal, in our testing we found that choosing a different value of σ or an even less informative (or less prejudiced) uniform prior distribution induces not much of a difference in the posterior (see Appendix B of (Elkhashab, Porciani and Bertacca, 2024)). This suggests that the posterior is dominated by the data likelihood and priors contribute only a minimal amount.

Fig. 3.6 show the posterior distribution calculated for FOTO measurements for one realization using just the monopole, only even multipoles, only odd multipoles and all multipoles combined (using 12 data-points per multipole). It clearly shows that the fiducial velocity used to generate the mocks lies within the 68-percentile region in all the four cases. Furthermore, a shrinkage in the Highest Posterior Density Interval (HPDI) can be observed when information from higher multipoles is also utilized.

The posterior distributions displayed in Fig. 3.6 can demonstrate a sensitivity to the FOTO signal of the specific realizations. The shaded region in Fig. 3.2 illustrates that the FOTO signal can have a noticeable scatter around the model prediction and, hence, the velocity inference too would reflect the down-stream effects of this scatter. To ensure that the HPDI shown in Fig. 3.6 is neither intentional cherry-picking nor an unlikely fluke, we perform the MCMC analysis for each one of our 125 realizations. The results of this exercise are shown as bar plots in Fig. 3.7, where the star represents the median of one MCMC chain and the error bars are 1σ intervals. The horizontal line represents the fiducial observer velocity used to generate the mocks and the histograms on the right column display the scatter of our posterior maximizing parameter inference across different

---

[4] See `emcee` docs: emcee.readthedocs.io/

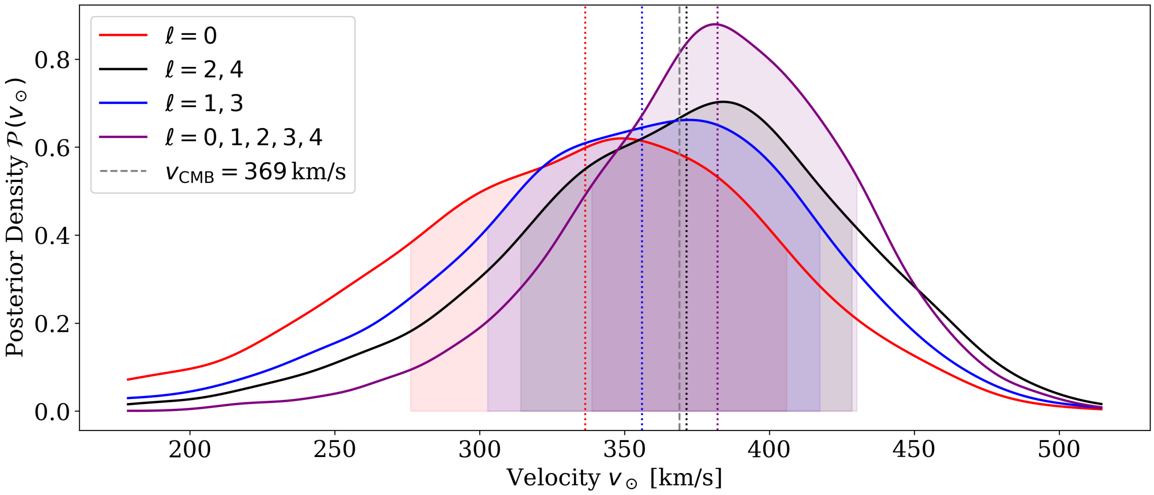

Figure 3.6: Comparing the posterior distributions for a single realization inferred using likelihood with only monopole, only even multipoles, only odd multipoles and all multipoles of the FOTO signal. Shaded regions represent the 68% confidence intervals. Colored vertical lines represent the median velocity of the corresponding distribution and the gray dashed line represents the fiducial velocity. A generalization of these results across all realizations is shown in Fig. 3.7.

realizations. If we average the HPDI intervals across all realizations to get an estimate of the mean uncertainty on our measurements, we find that $\bar{\Delta}\mathrm{HPDI}_{\ell=0} = 63.6$ and $\bar{\Delta}\mathrm{HPDI}_{\ell=0,1,2,3} = 49.5$. This suggests $\approx 28.5\%$ tighter constraints on velocity while using all multipoles as opposed to monopole only. The standard deviation of the histograms on the right column of Fig. 3.8 are in approximate agreement with the average HPDIs, confirming that the uncertainties are not substantially under or over-estimated. Furthermore, the bias $(\bar{X} - X)/\sigma$ remains less than 0.05 in all four cases as well.

Finite Sample Correction to Covariance

Although these results represented by the dotted curves in Fig. 3.8 appear promising, they do not account for an important statistical fact. While estimating the covariance matrix C from N realizations of a data vector of length p, the covariance follows a Wishart Distribution (a generalization of Γ distribution to multiple dimensions) (Wishart, 1928; Bekker, Niekerk and Arashi, 2017). When working with a small number of samples, the inverse covariance matrix (called the 'precision matrix') and, consequently, the likelihood of the evidence can become highly biased. The expectation value of the inverse covariance $\langle C^{-1} \rangle$ deviates from the true precision matrix Σ and instead becomes (Hartlap, Simon and Schneider, 2007)

$$\langle C^{-1} \rangle = \frac{N - p - 2}{N - 1} \Sigma^{-1} \equiv \alpha_h \Sigma^{-1}. \tag{3.8}$$

To de-bias this estimate we apply a finite-sample correction to the inverse covariance. While this statistical fact has been known for a few decades (Tam, 1985), cosmologists often call this the 'Hartlap correction' in reference to Hartlap, Simon and Schneider, 2007 who argued for its relevance in cosmological parameter estimation.

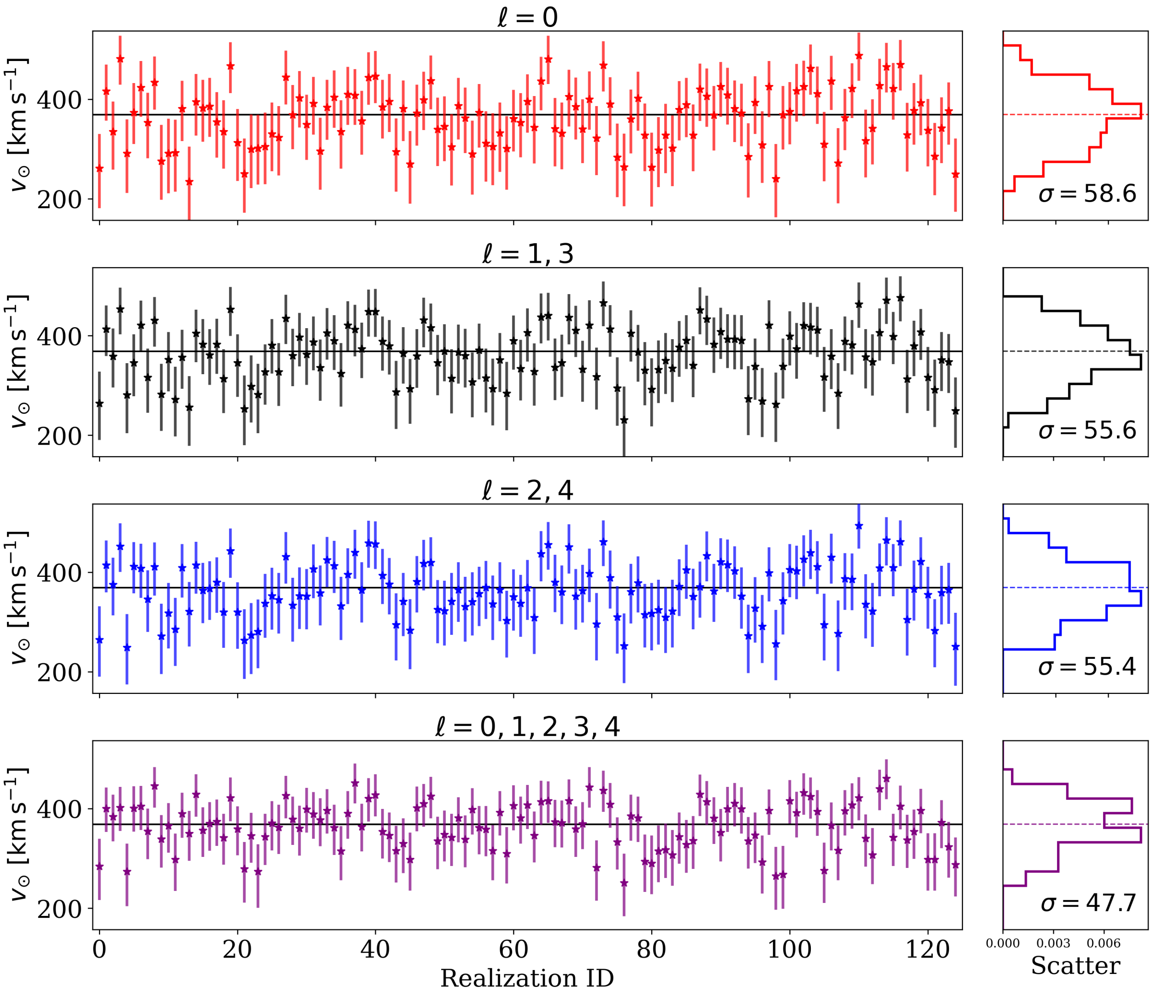

Figure 3.7: Posteriors for $v_\odot$ in $z \in (0.9, 1.8)$ for monopole, even, odd, and all multipoles (12 bins per multipole with $\delta k = 0.34 \times 10^{-3}\,h\,\mathrm{Mpc}^{-1}$). Horizontal lines represent the fiducial $v_\odot$. Average half-width highest posterior density intervals are $\bar{\Delta}\mathrm{HPDI}_{\ell=0} = 63.6$ and $\bar{\Delta}\mathrm{HPDI}_{\ell=0,1,2,3} = 49.5$. Histograms in the right columns represent the scatter of median velocity in the MCMC chains across realizations.

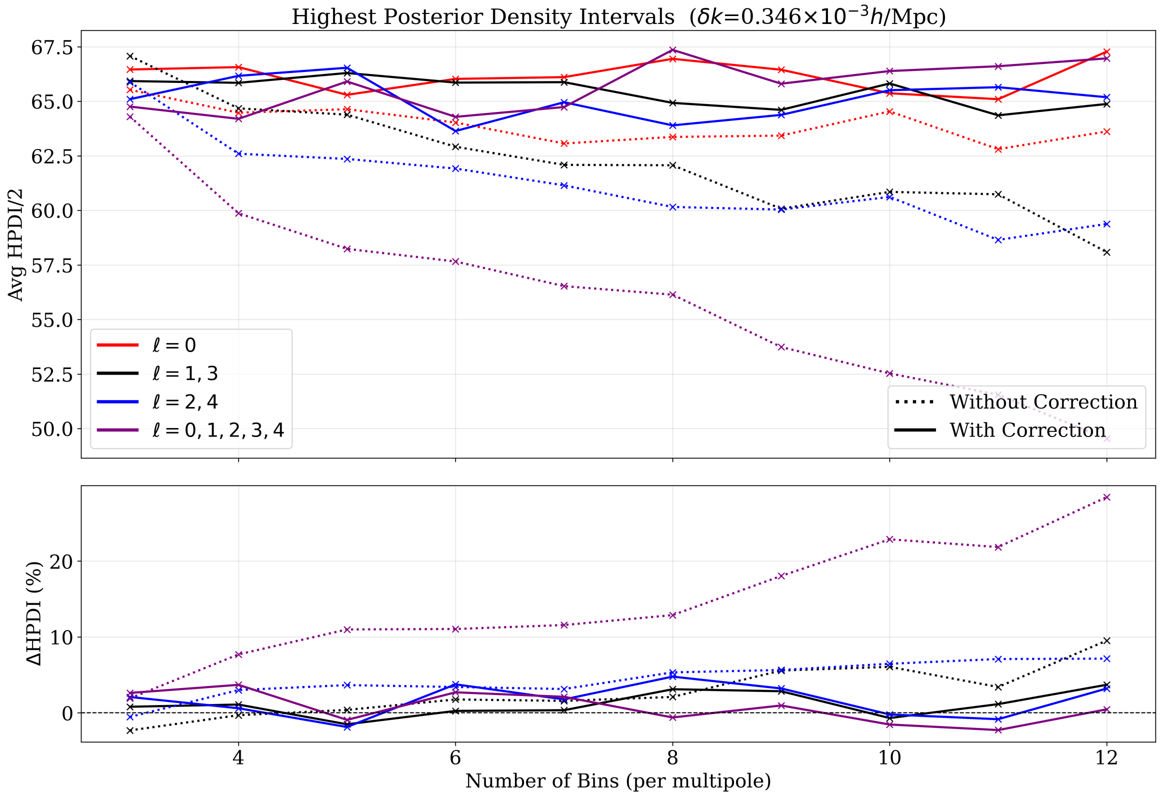

Figure 3.8: Effect of number of bins considered (per multipole; $\delta k = 0.346 \times 10^{-3}$ h/Mpc) on the half-width of the HPDI with (solid) and without (dashed) applying finite-sample correction to the covariance during inference of $v_\odot$. The different line colors depict inference results using different sets of power spectra multipoles. Without the Hartlap correction, preparing data vectors with concatenated multipoles can provide up to 30% tighter constraints on velocity. The correction inflates confidence intervals and the advantage in using longer data vectors is substantially subdued.

This multiplicative correction remains close to 1 when $N >> p$, such as when considering 12 bins of the monopole ($1 - \alpha_h \approx 11\%$). However, when we include the higher multipoles the length of the data vector becomes five times larger and the correction factor shrinks considerably (for 12 bins ×5 multipoles, $1 - \alpha_h \approx 50\%$). Thus, the data vector of concatenated multipoles is 'punished' by the finite-sample correction for its length and the constraining power competes against this penalty. This is seen in the solid lines of Fig. 3.8 which remain generally above the dashed lines in the top panel (representing wider HPDI) and below the dashed lines in the bottom panel (representing lower fractional gains).

To lessen the impact of the Hartlap correction, one can investigate what might happen if the covariance matrix is estimated with a much greater number of realizations (effectively, making the finite sample correction smaller). For instance, if we had 1250 realizations then the finite sample correction would only differ by ≈ 3% on using 12 bins per multipoles in monopole-only and all-multipoles case. Consistent with this, in the Hartlap corrected case, we find that even though the average HPDI sees no noticeable gain, the scatter of the best-fit $v_\odot$ across mocks is much tighter when additional multipoles are included. In fact, Fig. 3.9 shows that the scatter drops from

$\sigma_{\ell=0} = 57.6\,\mathrm{km\,s^{-1}}$ to $\sigma_{\ell=0,1,2,3,4} = 44.6\,\mathrm{km\,s^{-1}}$ (an approximately 20% improvement). This suggests that the Hartlap-corrected error bars are over-estimated (and, possibly, over-cautious). However, there is no guarantee that reducing the Hartlap factor would lead to substantially higher gains. Instead, the gain depends on the physics and statistics of the extra multipoles and whether they carry independent information rather than correlated noise. Moreover, generating hundreds of relativistically correct mock skies could be highly resource intensive[5] The alternative strategy to recover potential benefits in using higher multipoles of FOTO could be to compress information into shorter data vectors. Such a compression can be attempted at varying levels of sophistication.

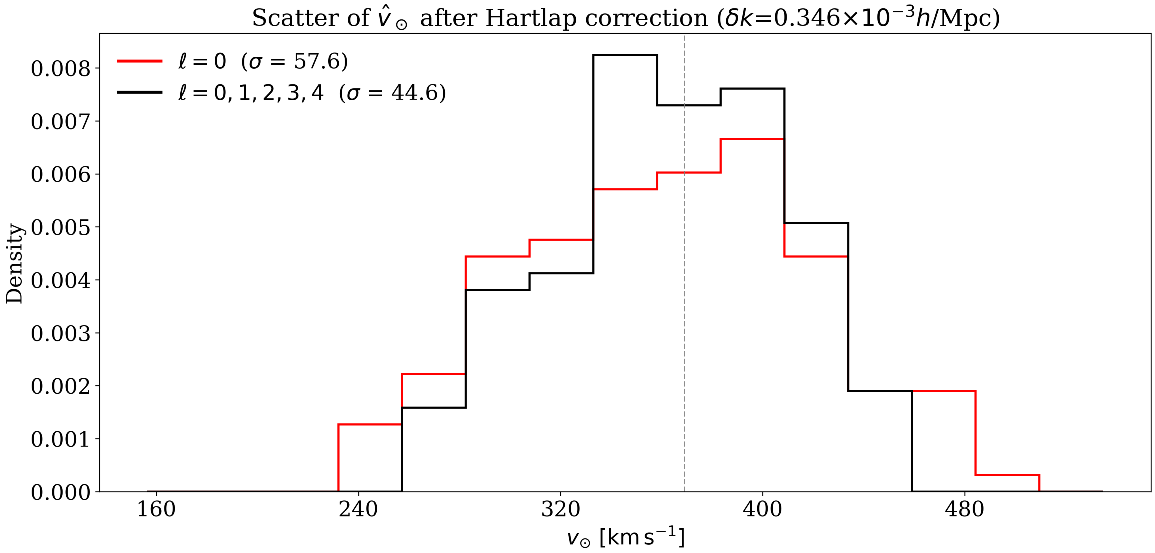

Figure 3.9: Distribution of best-fit $v_\odot$ over 125 mocks using Hartlap-corrected covariances for Bayesian inference. The scatter of best fits tightens from $\sigma = 57.6\,\mathrm{km\,s^{-1}}$ to $\sigma = 44.6\,\mathrm{km\,s^{-1}}$ (≈ 23% reduction), hinting at extra information in higher multipoles. However, the average 68% HPDI does not shrink case due to a higher finite-sample correction to the precision matrix (see Fig. 3.8), motivating compression.

Re-Binning to Broader Bandwidths

The simplest strategy to compress data and lessen the impact of Hartlap correction is to re-bin the data into fewer points containing wider band-powers. In doing so, adjacent elements that carry highly correlated information collapse into one number. For instance, instead of one bin representing a power spectrum interval over $\delta k = 0.34 \times 10^{-3}\,h\,\mathrm{Mpc^{-1}}$, we generate wider bins[6] of $\delta k = 1.14 \times 10^{-3}\,h\,\mathrm{Mpc^{-1}}$. With this binning, we can span a similar range of approximately $k \in (0.35 \times 10^{-3}, 4.00 \times 10^{-3})\,h\,\mathrm{Mpc^{-1}}$ in six bins instead of twelve. Fig. 3.11 illustrates the correlation matrix for the data vector P^O before and after re-binning the power into wider bands. It shows that re-binning into wider bins can effectively compress highly correlated nearby points into a single bin but the correlations across multipoles (which manifest as off-diagonal banded structures in the left panel of Fig. 3.11) still survive after re-binning. To further eliminate these correlations would require more careful compression techniques which will discuss later in §3.1.2.

---

[5] Although, the presence of a large suite of such mock skies (assuming an appropriate runtime configuration) can be mined for various studies of linear order relativistic effects. There is, thus, at least some argument justifying this resource consumption.

[6] The re-binning transformation is, essentially, an average weighted with the number modes in an interval.

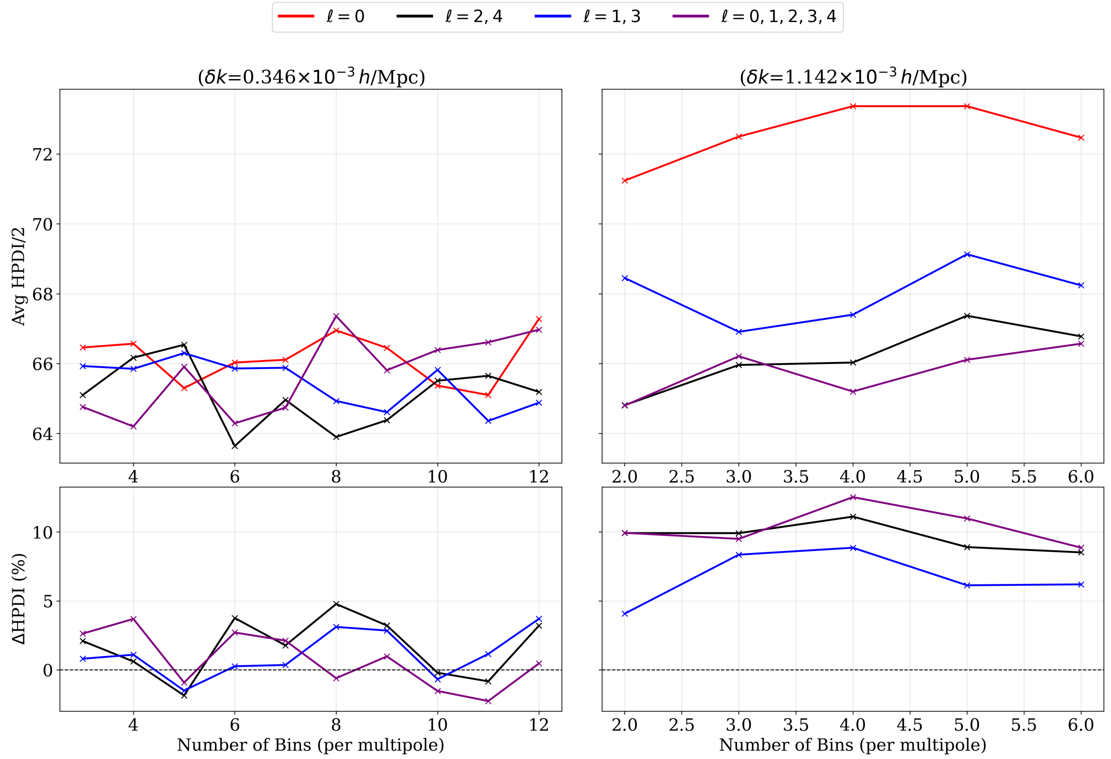

Figure 3.10: This figure compares the average half-width HPDI for Hartlap-corrected inference chains before (left) and after (right) re-binning to wider bandwidths. Looking at the bottom panels, one notices that by re-binning, the competing influences of higher multipoles and precision matrix debiasing can be neatly disentangled. The curves in bottom right column stay consistently above zero (reaching almost 12.5%) indicating a clear (albeit small) advantage in using higher multipoles. However, the top panels reveal that this relative gain arises not because re-binning genuinely shrinks the HPDI but because the signal in the monopole is washed out and it’s constraining power is diluted.

Fig. 3.10 shows a ≈ 12.5% fractional gain in the re-binned data vector (in the optimal case of using all multipoles and 4 bins per multipole) clearly wins over the finite-sample penalty. However, re-binning coarse grains the resolution and the oscillatory features can get partially washed out. In the monopole, for example, the second peak’s small amplitude is averaged with neighboring noisy bins, weakening its constraining power. As a consequence of this, the constraining power of the monopole goes down and the half-width HPDI widens to over 70 $\mathrm{km\,s^{-1}}$. When we compare HPDI across the best-case configurations of two bandwidths (narrow: 6 bins/multipole using even multipoles; broad: 2 bins/multipole using all multipoles), the minimum HPDI is similar ≈ 65 $\mathrm{km\,s^{-1}}$. This is partly explained by the fact that re-binning reduces the data dimension but leaves significant cross-ℓ correlations, so the extra bins do not translate into additional independent information (see off-diagonal banded structures in right panel of Fig. 3.11).

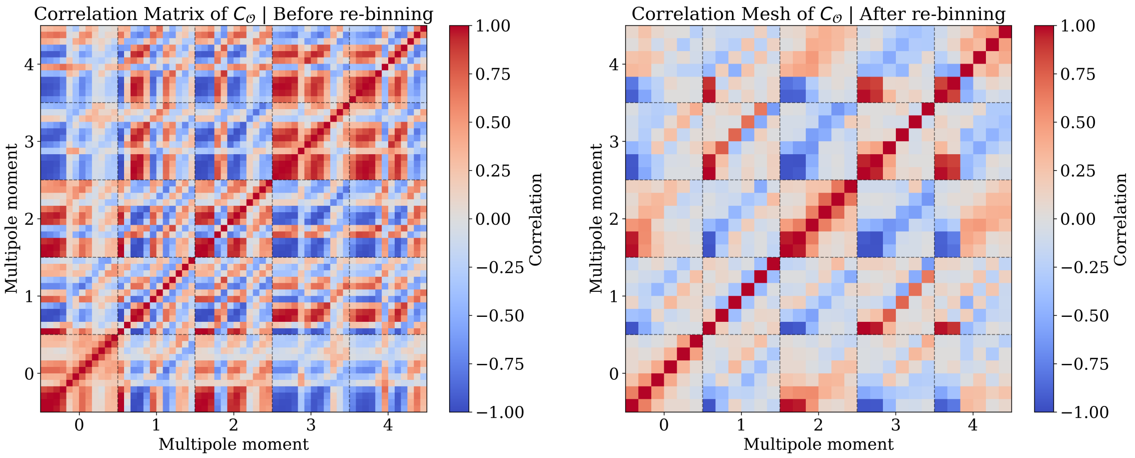

Figure 3.11: Heatmap illustrating the magnitude of terms in the correlation matrix for power spectra multipoles of $\mathcal{O}$. The left and right panels compare the correlations before and after re-binning from $\delta k = 0.34 \times 10^{-3}\, h\,\mathrm{Mpc}^{-1}$ to $\delta k = 1.14 \times 10^{-3}\, h\,\mathrm{Mpc}^{-1}$. Even after re-binning, the cross-multipole correlations survive (as seen in the off-diagonal banded structures on the left) and eliminating these require different compression techniques.

Projection on principal components

Since re-binning did not yield genuinely tighter posteriors, we now turn towards more sophisticated compression algorithms that transform the data into a small set of uncorrelated modes and retains essential information while keeping the effective dimensionality of the data (and therefore the Hartlap penalty) small. Looking at Fig. 3.11, one can notice that the amplitudes of a large fraction of bins move coherently and are, hence, correlated. If we could identify the correct representation of this quantity that drives similar changes in the amplitude across power spectrum multipoles, we would be able to leverage that representation to compress very effectively. One common method for identifying the hierarchy of relevance ranked features in the data is to perform a principal components analysis (which is closely related to, or is otherwise called, Singular Value Decomposition (G. W. Stewart, 1992) or Karhunen-Loeve Transform (Tegmark, Taylor and A. Heavens, 1997)). It can be shown that the directions in a high dimensional space which maximizes the projections of a distribution are simply the eigenvectors of its covariance matrix. These eigen-vectors, also called principal components, are associated with their respective eigenvalues λ (not to be confused with the likelihood ratio from earlier) that represent the relative contribution to the total covariance. For p dimensional data, the symmetric covariance matrix has $p \times p$ entries and p eigenvectors.

Fig. 3.12 represents the eigen decomposition of the two covariance matrices – $C_{\mathcal{O}}$ and $C_{\mathcal{G}}$. First, we note that in eigenvalues of in the covariance of the FOTO signal drops sharply beyond the first few points. This explains the strong correlations and low gain in constraining power with additional bins. If we consider all bins across all multipoles and project the distribution along the eigenvectors of C, we will find that using only three of the most important directions would suffice to approximate the total covariance faithfully up to 95% of its original magnitude (see the red curves in the right column of Fig. 3.12). Data compression with PCA, therefore, can help us in avoiding high finite-sample corrections due to the dimensionality of the data vector. Thus, we can confidently report that the most gain which including higher multipoles can provide against the best constraint using monopole only, in our testing, was found to be less than 5%.

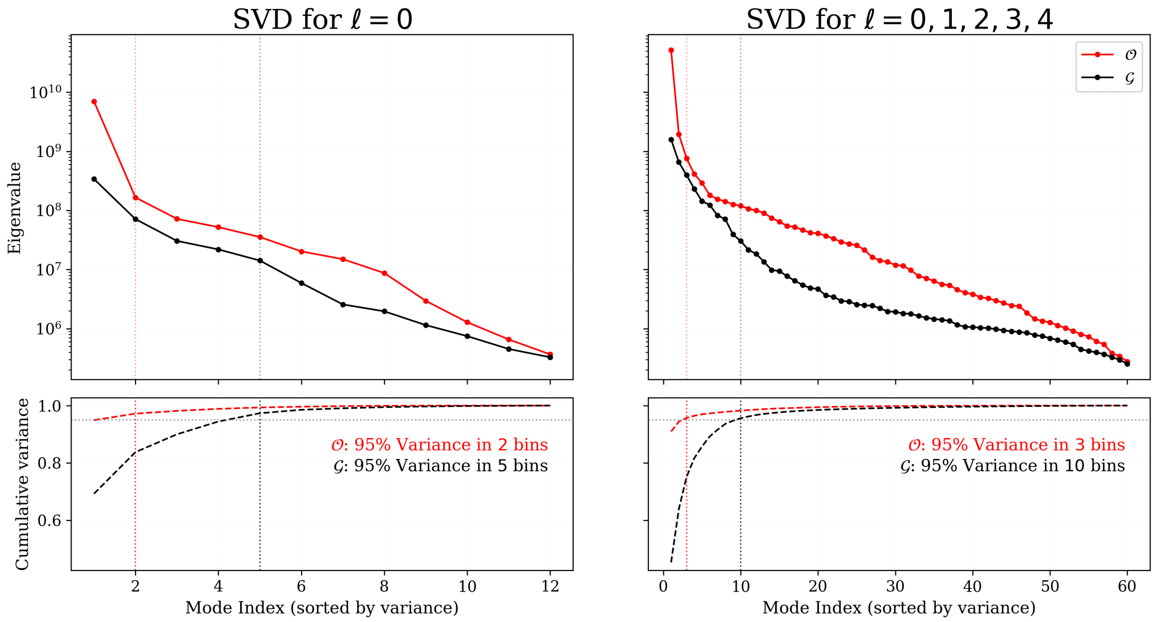

Figure 3.12: Eigenvalue spectra (top) and cumulative variance (bottom) for covariance of power spectra measurements of $\mathcal{O}$ and $\mathcal{G}$. The left and right columns compare the cases of considering only monopole against considering higher multipoles before performing PCA. In both cases, the spectra falls sharply in the presence of FOTO signal and most of the covariance can be reconstructed with projections along only a few eigenvectors.

A summary of the findings related to Bayesian inference of velocity inference is presented in Table. 3.1. There are other compression methods that can out-perform PCA (such as MOPED) but, given our current results, we may not expect drastic improvements from the higher multipoles by switching to a different compression scheme. Instead, we now focus our attention to investigating the origin and implications of the fact that our estimate of the covariance of power spectrum, over a certain bandwidth with all relativistic effects included, can be very well approximated by a very low-rank tensor.

3.2 Discussion

In this section, we discuss the reason behind why the FOTO signal can be compressed into very few PCA bins and the related question of why the various multipole orders of the FOTO signal carry largely redundant information. To do so, we consider the multipole expansion of a different summary statistic for capturing the relativistic distortion due to the observer velocity effect. Under the full-sky assumption, if we compute the angular power spectrum C_ℓ of the difference between the overdensity fields for an observer at rest in the CMB frame (i.e. $\mathcal{G}$ type mocks) and an observer moving with our peculiar velocity (i.e. $\mathcal{O}$ type mocks), we find that the field displays a clear planar symmetry aligned with the dipole of the observer velocity. Fig. 3.13(a) is an illustration of the planar symmetry in the difference between the two aforementioned overdensity fields (for the same configurations as the bottom right panel of Fig. 3.13(a)).

Euclid Collaboration et al. (2025) estimate the angular power spectrum of this field using the same

Table 3.1: Summary of inference results and their sensitivity to binning and compression choices. The average half-width HPDI are reported for the best configurations found for each case. The last column reports the relative gain in constraining power of a particular combination of multipoles over the posteriors inferred using the monopole only.

Case	ℓ	**Bins**		**Statistics** [km/s]			**Gain %**
		N_{bins}	δk ($h\,\text{Mpc}^{-1}$)	$\hat{v}_\odot$	$\overline{\text{HPDI}}/2$	σ	
No Hartlap	0	11	0.3×10^{-3}	369.0	62.8	57.6	-
	2, 4	11	0.3×10^{-3}	369.3	60.7	55.3	3
	1, 3	12	0.3×10^{-3}	369.3	58.1	54.1	8
	0, 1, 2, 3, 4	12	0.3×10^{-3}	369.4	49.5	45.8	28
Hartlap-corrected	0	11	0.3×10^{-3}	369.4	65.1	57.1	-
	2, 4	6	0.3×10^{-3}	369.6	63.6	55.8	2
	1, 3	11	0.3×10^{-3}	369.5	64.4	53.4	1
	0, 1, 2, 3, 4	4	0.3×10^{-3}	369.2	64.2	53.0	1
PCA-compressed	0	6	0.3×10^{-3}	369.1	62.4	64.8	-
	2, 4	5	0.3×10^{-3}	369.4	62.1	57.1	0
	1, 3	3	0.3×10^{-3}	369.4	62.1	57.5	0
	0, 1, 2, 3, 4	5	0.3×10^{-3}	368.9	61.6	58.1	1

survey functions utilized in this project and with a similar application of LIGER method that this study employed. Fig. 3.13(b) has been reproduced from their study and it demonstrates how all of the overdensity difference that drives the amplitude of the FOTO signal in the 1D power spectrum can be encapsulated in a single multipole order of the angular power spectrum i.e the angular dipole $C_{\ell=1}$. It is clear from Fig. 3.13(b) that performing velocity inference using higher orders of $C_{\ell\,\geq\,1}$ would not lead to a substantial increase in the constraining power of the signal because the signal resides only in one of the multipole expansion orders.

In measuring the observer velocity effect using the 1D matter power spectrum, we project a distortion of the density field that is naturally suited for a spherical geometry based statistic onto a cartesian basis. It is for this reason that a complete representation of the effect becomes more complicated, requiring several terms of the multipole expansion with similar amplitudes. However, at a fundamental level, it is the same signal from the dipole of the angular power spectrum that drives the FOTO oscillations through the projections on various spherical Bessel integrals. In other words, the amplitude of oscillations across k-bins and multipole orders moved coherently (either as strong correlations or anti-correlations) because all those data points were largely determined by the strength of the signal in a single term of the angular power spectrum.

To confirm that this result about effective compression into a few bins is not Euclid specific, we computed the principal components and their relative important for SKA-like mocks as well. Since the number density of tracers for SKA-like mocks is orders of magnitude higher, it takes substantially more memory and time to perform the CIC interpolation before estimating the power spectrum. Thus, we only analysed the principal components of the FOTO multipoles for tomographic redshift bins of SKA-like mocks (as shown in Fig. 3.1). The results of this exercise validate our observation because, for SKA-like mocks too, more than 95% of the covariance can be approximated by a small number of principal components (as shown in Table. 3.2). The only notable exception is the last redshift bin (0.8, 1.0) which seems to require more PCA modes than other bins. However, this can be easily explained by the fact that the FOTO signal itself vanishes in the last bin and, thus, PCA analyses only captures modes of noise-like directions. This also highlights an important limitation of PCA by showing that the principal components are only optimized for capturing most of the covariance and not necessarily prioritizing those features of the data that contain the highest SNR.

Table 3.2: A summary of the number of principal components required to capture 95% of the covariance across tomographic redshift bins of SKA-like mocks.

Redshift bin	Modes containing 95% covariance	
	$\ell = 0$	$\ell = 0, 1, 2, 3, 4$
(0.1, 0.2)	1	1
(0.2, 0.4)	2	2
(0.4, 0.6)	1	2
(0.8, 1.0)	4	6

An upshot of this work has been to show that although the 1D power spectrum is not the tool that is the most naturally suited (geometrically speaking) for measuring anisotropies on the celestial sphere, leading to various non-zero terms in the multipole expansion required for a faithful representation of the planar symmetry, individual terms of the expansion can independently carry most of the signal's constraining power. Consequently, if we extend our work to a thousand or more mocks in the future, by restricting ourselves to lower order multipoles we can place similar sized constraints that we get using higher multipoles, while having to perform tens of thousands of fewer FFTs in the process. This is possible because the results of our investigation into the higher multipoles have established that the FOTO signal is a low-rank quantity and an early truncation of the multipole expansion can carry a large fraction of the signal's constraining power.

3.3 Outlook

3.3.1 Anisotropic Cosmological Models

A statistically significant misalignment between the CMB and matter dipoles would point either to unaccounted systematics or to new cosmological physics. Having discussed the concrete and scrutable statistics, for the sake of completeness, we shall now make a brief interlude to review some theoretical perspectives on the issue of cosmic anisotropies. For the purposes of this section, then, let us suppose that future observations contain a reluctant dipole anomaly which refuses to yield to systematic corrections. There already exists an entire landscape of theoretical models designed to accommodate such a deviation between early- and late-universe dipoles.

If the early and late universe dipoles are misaligned, then there could be at least three possible categories of resolutions — modifying symmetries at the FLRW metric's level, introducing bulk

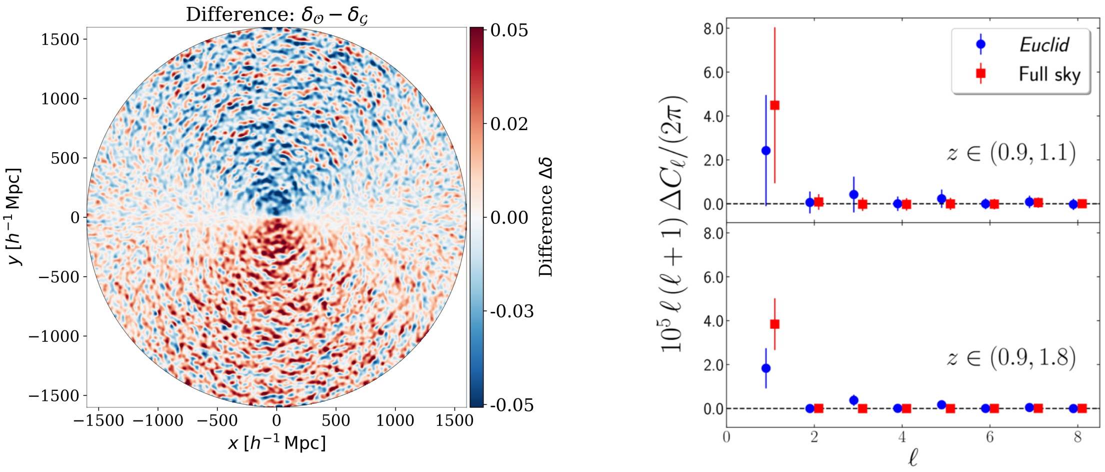

(a) (b)

Figure 3.13: (Left) Relativistic distortion to a slice of overdensity field contributed by the observer velocity term. In 2D, the gradient demonstrates a planar symmetry that is a projection of a dipole in the angular power spectrum. See the caption of Fig. 3.13(a) for details on the production of this illustration. (Right) Figure reproduced from Euclid Collaboration et al. (2025) showing angular power spectrum measurement of the FOTO signal's contribution to the overdensity field in a Euclid-like survey. In the C_ℓ representation, we find that the entire signal resides in the dipole term for full-sky and only leaks into higher multipoles when convoluted with a window function.

matter flow through primordial perturbations or decoupling rest frames of matter and radiation[7]. In fact within each of these parent categories, there can be two different kinds of models – ones with a fixed anisotropy and others with a dynamically evolving one. For the second class of models, one can show via dynamical systems view of cosmology, that even highly anisotropic cosmological models can show local and transient patches of high degrees of isotropization.

The first family of theories where the kinematic interpretation of the CMB dipole may not suffice could be universes with anisotropic expansion i.e. cosmological models where the spacetime expansion rates differ with directions. A well-studied example of this kind would be a Bianchi type universe. Such models remain highly popular among physicists because their symmetries allow a reduction of the Einstein Field Equations from PDEs to ODEs, making analytic investigations more tractable. However, among cosmologists, it is widely considered that non-zero anisotropic shear is ruled out by constraints from Planck data (Pontzen, 2016). For instance, analysis by Saadeh et al. (2016) shows that anisotropic expansion is strongly disfavored by CMB data at the odds of 121,000:1. As mentioned earlier, however, Bianchi type universes can isotropize (Wainwright et al., 1998; Coley, 2003) such they can resemble FLRW-like symmetries locally. De et al. (2022) show one such mechanism of isotropization for the case of locally rotationally symmetric Bianchi Type-I universes in an $f(Q)$ extension of symmetric teleparallel gravity (i.e. gravity based on coupling non-metricity with stress-energy momentum, as opposed to curvature). In contrast to mechanisms for isotropization, there are als mechanisms for generating anisotropies. Consider, for example, Campanelli (2009) who provide a model for anisotropization by showing how a particular kind of Lorentz invariance violation can cause super-adiabatic fluctuations of magnetic field that can possess planar symmetry on cosmological scales.

---

[7] Arguably, the boundaries between these 'types' of theoretical modifications are not completely rigid (in that any one of them may also insinuate another)

Another way a misalignment may originate could be through a coherent bulk flow of matter in the CMB frame. The simplest explanation along these lines could be the existence of super-structures farther away than the Great Attractor. Existence of such super-structures is contingent on having the right seeds for structure formation. Turner (1991) claim that if inflation lasted ≈ 10 e-folds longer than needed to solve the horizon problem, then the pre-inflationary super-Hubble perturbations could create dipole-anisotropies that 'give the illusion of a tilted universe' (Turner, 1991). Later studies of tilted universe proposals have determined that only isocurvature modes of super-horizon perturbations can induce a leading-order intrinsic dipole in the CMB (Domènech et al., 2022; Erickcek, 2008). A mechanism suggested to generate a spectral continuum of such super-horizon isocurvature perturbations is via the Axion model of cold dark matter (Adams et al., 2023). Axions are hypothetical particles which were, originally, introduced to resolve the strong CP problem of quantum chromodynamics. These particles are generated by the spontaneous breaking of Peccei-Quinn symmetry and, if they are generated during the inflationary epoch, they can induce large isocurvature perturbation modes (Erickcek, 2008).

Finally, a third class of explanations for a misalignment between early and late universe dipoles could be that radiation and matter no longer share a co-moving rest frame. This, however, raises the question that if matter and radiation were strongly coupled in the early universe, how come their rest-frames have acquired a relative velocity with respect to each other now. Jimenez and Maroto (2009) propose that this can be achieved if dark energy was moving with respect to primordial plasma in the early universe. They argue that if dark energy is modeled as a perfect fluid which has always remained uncoupled from matter and radiation contents of the universe, then there is no *a priori* justification for assuming that DE shares the same rest frame as the other two. If one accepts this, then the relative dark energy velocity v_{DE} would have to be treated as an independent cosmological parameter on the same footing as Ω_{m} or w_{DE} (Jimenez and Maroto, 2009).

3.3.2 Challenges and Prospects

In this work, we introduced a power-spectrum based method to measure an observer's peculiar velocity using the FOTO signal. Then, we demonstrated the possible improvements in the constraining power of the FOTO signal in Bayesian inferences of peculiar velocity. We computed the posterior HPDI in the case of a full-sky Euclid-like survey to be $\pm 60\,\mathrm{km\,s^{-1}}$. Although, in going from a full-sky geometry to a survey with a partial-sky coverage (and/or a galaxy mask), the Signal-to-Noise would be expected to drop (as shown in the case of monopole by Elkhashab, Porciani and Bertacca, 2024). Partial sky masks lead to a leakage from the dipole of the angular power spectrum to higher multipoles due to a convolution with the window function. When the signal starts looking more complicated in the angular geometry based statistics (i.e. its most natural representation), then the question of higher multipoles of 1D power spectrum become relevant again. This is because the different orders of C_ℓ may couple with different orders of P_ℓ in non-trivial ways. The study of partial sky masks will require accounting for mode-mixing of higher multipoles and deriving new analytical results. Doing so is left for future work.

Besides the impact of sky-fraction on the FOTO signal, another large systematic that was idealized in our work were the uncertainties on survey functions. Determining these survey functions is a

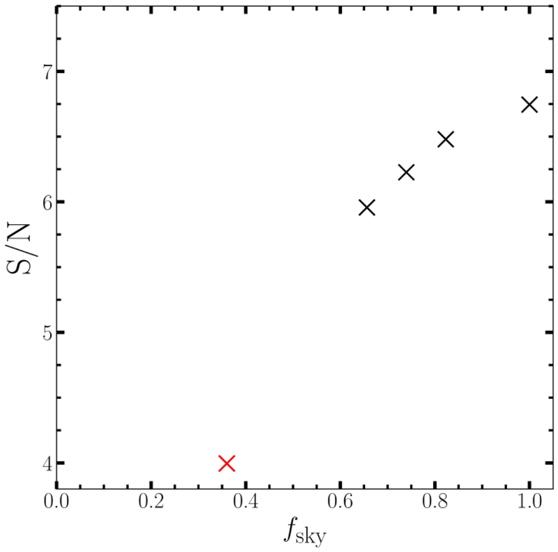

Figure 3.14: Figure reproduced from (Elkhashab, Porciani and Bertacca, 2024) summarizing the variation of signal-to-noise for FOTO monopole-only measurements in Hα widest bin with respect to sky coverage fraction. The red-cross is indicative of a realistic Euclid-like survey footprint with approximately one-third sky fraction. The impact of partial sky-coverage on inference with higher-multipoles remains to be seen.

difficult task. Instead, the impact of uncertainties in survey functions can be incorporated together as errors in the determination of α. Elkhashab, Porciani and Bertacca, 2024 report (for monopole only inference) that assuming (1%, 10%) errors on α results in widening the HPDI to $\bar{\Delta v} = (62, 71)\,\mathrm{km\,s^{-1}}$. According to Wang, 2024, the measurements of $\mathcal{Q}$ and $\mathcal{E}$ in eBOSS suggests that α_o for Hα surveys can be determined to 2% precision.

Elkhashab, Porciani and Bertacca (2024) also present a transformation for boosting the signal-to-noise of the FOTO effect and getting tighter constraints from the same mock skies. The core principle behind the Boosted-Finger of the Observer (B-FOTO) effect is that we choose an arbitrary velocity vector $\boldsymbol{v}_B$ and transform the redshifts of all galaxies to the rest frame of a fictitious observer moving with the peculiar velocity of $\boldsymbol{v}_B + \boldsymbol{v}_\odot$. On doing so, and accounting for the boosts appropriately in our theoretical models, we will find that the mismatch between the radial and angular relativistic effects further exaggerates the amplitudes of the FOTO fluctuations. Using the B-FOTO signal, Elkhashab, Porciani and Bertacca (2024) report constraints as low as $39\,\mathrm{km\,s^{-1}}$ for full-sky, widest-bin, Euclid-like measurements. Furthermore, the B-FOTO signal also enables us to measure the direction of the dipole due to a dot-product between $\boldsymbol{v}_B$ and $\boldsymbol{v}_\odot$ that appears in the analytic model. For our purposes, it is important to highlight that our claims concerning the higher multipole structure of the FOTO signal cannot be extrapolated to the multipoles of the B-FOTO effect. The nature of the overdensity field that determines the B-FOTO signal is sufficiently distinct from the nature of the overdensities that drive the FOTO signal. Therefore, another open problem left for future work is the following. Do higher multipoles of B-FOTO contain uncorrelated information or are they, too, like in the case of FOTO, largely redundant for estimating velocity constraints. Fig. 3.15 illustrates how potential measurement of the FOTO signal and the B-FOTO signal could compare against the other techniques for measuring peculiar velocity[8].

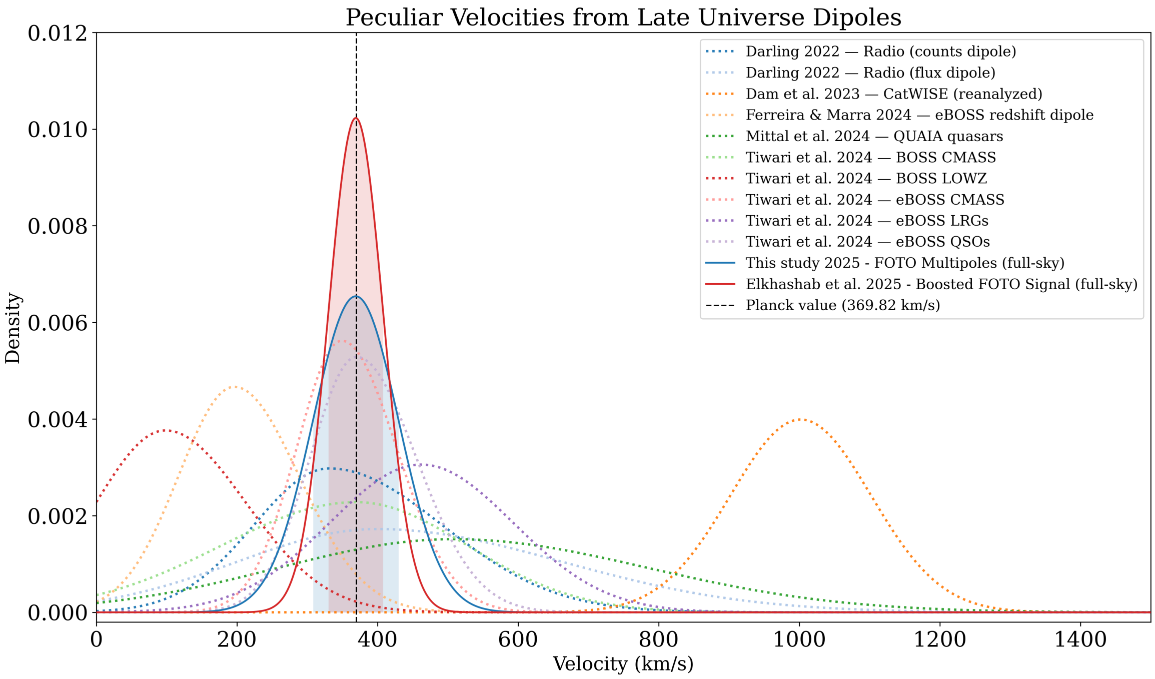

Figure 3.15: A recreation of Fig. 1.1 to highlight the potential constraining power of the PCA compressed multipoles of the FOTO signal (for one specific realization). An important caveat in this comparison is that other measurements come from partial sky footprints and the FOTO projections are presented assuming full-sky coverage. Applying realistic survey masks would lead to a drop in the FOTO amplitude as shown in Fig. 3.14. Measurements are quoted from Darling (2022), Dam, G. F. Lewis and Brewer (2023), P. d. S. Ferreira and Marra (2024), Mittal, Oayda and G. F. Lewis (2023), Tiwari et al. (2024) and Planck Collaboration et al. (2020). Gaussian errors are assumed for ease of illustration.

In our entire discussion, we have assumed a cosmology and tried to measure the dipole velocity. We could also, instead, fix the dipole magnitude and try to determine the cosmology. In particular, the FOTO signal is sensitive to the structure formation history and, hence, carries information about the matter density parameter Ω_m and the dark-energy equation of state. Elkhashab, Porciani and Bertacca (2024) demonstrate the feasibility of putting constraints on Ω_m using inferences from the FOTO signal. While these constraints may appear competitive at face value compared to other ways of estimating the density parameter (Schindler, 2002), it is important to remember that these have been computed assuming highly idealized settings (full-sky survey, perfect knowledge of survey functions, etc.). Extracting information about dark energy EOS is an even more futuristic goal and requires further more optimistic scenarios (because constraining the DE EOS tends to involve more number of parameters).

Further prospects of future work could involve trying to apply the FOTO technique on observations by the DESI collaboration, which is soon going to announce its third data-release. Doing so would require further careful study of the systematics specific to the survey. On the computational side, LIGER could be modified to account for wide-angle effects which become prominent on the same scales as the relativistic effects. Finally, extending LIGER's computations to beyond the first order in perturbation theory would also enable us to capture relativistic effects on higher-order statistics like the cosmic bi-spectrum and (its Fourier conjugate) 3-point correlation function (3PCF). It is now well known that the modern surveys can carry high fidelity information about these higher order statistics and their careful modeling would be essential towards fully utilizing this newly unlocked observational prowess.

---

[8] Note that the comparison is only illustrative because all the catalogs use partial skies and the FOTO-related work makes full-sky assumption.

3.4 Summary

We now present a brief summary of the main findings of this study. We started with motivating a need for a new measurement method for constraining our peculiar velocity in order to verify the kinematic interpretation of the CMB dipole. More specifically, we presented a puzzling array of claims on the compatibility between early- and late-universe dipoles which would benefit greatly from a novel measurement technique that avoids the systematics affecting Ellis and Baldwin style measurements (i.e. detecting a dipole in the number counts of flux-limited surveys). We then proposed using observer velocity induced general relativistic redshift space distortions as a probe for peculiar velocity. In particular, we computed the linear order corrections to the overdensity field in a perturbed FLRW universe and interpreted the various terms as contributions from well-known relativistic effects, such as the Kaiser effect, gravitational lensing, and integrated Sachs–Wolfe. Among these contributions, we isolated the Finger-of-the-Observer (FOTO) effect which we showed to be a redshift space distortion that depends on the square of the observer velocity and some survey dependent functions (number density of tracers, linear bias, magnification bias and evolution bias).

Moving from modeling the overdensity field to estimators for two-point statistics, we computed the effect of the observer velocity term on the multipoles of the 1D matter power spectrum. For a full-sky geometry, using local plane-parallel (LPP) approximation, we derived the general form of the FOTO effect represented as a multipole expansion using integrals of the spherical Bessel function as a basis and the Wigner-3j matrix to impose selection rules. We also showed the particular solutions for the first five multipoles of the FOTO effect. To move beyond theoretical expectations, we implemented a pipeline capable of generating mock skies containing the FOTO signal. Newtonian snapshots at various moments of cosmological structure formation history were generated using `CLASS` and `MUSIC2`, which were then stitched into relativistic light-cones using the `LIGER` method. Besides detecting which objects of the simulation box lay on an observer's past light-cone, `LIGER` also applies linear-order metric perturbations computed using local terms as well as line-of-sight integrals. We then performed baryon-painting by incorporating semi-analytic survey functions to model Euclid- and SKA-like galaxy overdensity fields, thereby bridging theoretical predictions with observationally relevant data. This forward-modeling step was crucial in allowing us to extract mock measurements of the FOTO signal under controlled conditions.

Using PyPower's implementation of the Yamamoto-Bianchi estimator, we measured the FOTO signal across 125 realizations based on randomly generated seeds for structure formation. Across tomographic redshift bins, we confirmed that the FOTO oscillations predicted by linear theory are robustly recovered using the Yamamoto-Bianchi estimator in monopole as well as higher order multipoles. We also found that the amplitude of the FOTO signal is sensitive to survey depth, with the widest-bin measurements for Euclid-like configurations yielding the strongest signal strength.

We then applied Bayesian inference, combining theoretical predictions with mock measurements in order to constrain the observer's peculiar velocity. Initially, these tests suggested that incorporating higher multipoles beyond the monopole can shrink posterior widths by up to $\approx 30\%$. However, we also showed that this apparent improvement is strongly diminished once finite-sample corrections to the precision matrix (Hartlap correction) are applied. With our limited number of realizations (125), lengthening the data vector by concatenating higher multipoles substantially inflated the covariance and erased the gain in constraining power that we observed earlier.

To mitigate this issue, we explored data compression techniques such as re-binning and principal component analysis. Re-binning successfully reduced redundant correlations in the data vector and allowed modest shrinkage in HPDI using multipole information. In practice, however, the improvement stemmed from degrading the monopole signal rather than multipoles providing genuinely tighter constraints. PCA offered a more systematic route to compression and its implementation revealed that upwards of 95% of the covariance across the k-bins and multipole orders of the FOTO signal could be compressed into 3 of the most significant principal components. This indicated that the FOTO signal is a low-rank effect which can be efficiently compressed because the fluctuations across the data-points show strong correlations (or anti-correlations) and carry redundant information.

To explain the origin of these correlations, we referred to the angular power spectrum of the observer velocity distortion to the overdensity field. We highlighted that, in the spherical geometry FOTO effect manifests as a non-zero contribution exclusively to the dipole $C_{\ell=1}$ but projecting this anisotropy of the celestial sphere on a cartesian basis leads to the many non-zero terms in the multipole expansion of the 1D power spectrum. The strong correlations across FOTO multipoles were traced back to their amplitudes being driven by a single mode of the angular power-spectrum.

As the most natural extensions of this study, we proposed investigating the effects of partial sky masks (i.e. emulating realistic survey footprints) on the constraining power of FOTO multipoles. We also proposed extending the study of higher order multipoles to the Boosted FOTO method, as the nature of the overdensity distortions driving B-FOTO amplitude could vary in non-trivial ways compared to the overdensity distortions that underlie the standard FOTO method.

In conclusion, this work answers a hitherto open question – what is the role of higher order multipoles of the FOTO signal in providing velocity constraints? The answer we provide is that future work employing the FOTO technique can confidently truncate their multipole expansions because the lower order terms can carry most of the constraining power that one recovers by gathering combinations with higher order terms. More importantly we highlight that, even though the 1D matter power spectrum is not the most geometrically simplified description of dipole anisotropies on celestial sphere, Finger-of-the-Observer effect can provide useful constraints on our peculiar velocity in the future and it remains a highly promising probe for understanding the deviation from ideal Hubble flow exhibited by the slow march our cosmic neighborhood.

Bibliography

Abelson, R. P. (1995), *Statistics as principled argument*, eng, OCLC: 45727995, Hillsdale, N.J.: L. Erlbaum Associates, ISBN: 978-0-585-17659-8 (cit. on p. 54).

Adamek, J., D. Daverio, R. Durrer and M. Kunz (2013), *General relativistic N -body simulations in the weak field limit*, en, Physical Review D **88** 103527, ISSN: 1550-7998, 1550-2368, URL: `https://link.aps.org/doi/10.1103/PhysRevD.88.103527` (visited on 23/06/2025) (cit. on p. 9).

– (2016), *General relativity and cosmic structure formation*, en, Nature Physics **12** 346, ISSN: 1745-2473, 1745-2481, URL: `https://www.nature.com/articles/nphys3673` (visited on 23/06/2025) (cit. on p. 9).

Adams, C. B. et al. (2023), *Axion Dark Matter*, arXiv:2203.14923 [hep-ex], URL: `http://arxiv.org/abs/2203.14923` (visited on 27/09/2025) (cit. on p. 69).

Aharonian, F. et al. (2013), *Pathway to the Square Kilometre Array - The German White Paper -*, arXiv:1301.4124 [astro-ph], URL: `http://arxiv.org/abs/1301.4124` (visited on 23/06/2025) (cit. on p. 1).

Amanatides, J. and A. Woo (2023), *A Fast Voxel Traversal Algorithm for Ray Tracing*, en, (cit. on p. 42).

Banerjee, A. and T. Abel (2020), *Nearest Neighbor distributions: new statistical measures for cosmological clustering*, Monthly Notices of the Royal Astronomical Society **500** 5479, arXiv:2007.13342 [astro-ph], ISSN: 0035-8711, 1365-2966, URL: `http://arxiv.org/abs/2007.13342` (visited on 07/07/2025) (cit. on p. 28).

Bardeen, J. M. (1980), *Gauge-invariant cosmological perturbations*, en, Physical Review D **22** 1882, ISSN: 0556-2821, URL: `https://link.aps.org/doi/10.1103/PhysRevD.22.1882` (visited on 23/06/2025) (cit. on p. 11).

Bartolo, N., S. Matarrese, O. Pantano and A. Riotto (2010), *Second-order matter perturbations in a CDM cosmology and non-Gaussianity*, Classical and Quantum Gravity **27** 124009, ISSN: 0264-9381, 1361-6382, URL: `https://iopscience.iop.org/article/10.1088/0264-9381/27/12/124009` (visited on 23/06/2025) (cit. on p. 10).

Bekker, A., J. van Niekerk and M. Arashi (2017), *Wishart distributions: Advances in theory with Bayesian application*, Journal of Multivariate Analysis **155** 272, ISSN: 0047-259X, URL: `https://www.sciencedirect.com/science/article/pii/S0047259X16302317` (visited on 28/09/2025) (cit. on p. 59).

Bertacca, D. (2015), *Observed galaxy number counts on the light cone up to second order: III. Magnification bias*, Classical and Quantum Gravity **32** 195011, ISSN: 0264-9381, 1361-6382, URL:

https://iopscience.iop.org/article/10.1088/0264-9381/32/19/195011 (visited on 23/06/2025) (cit. on pp. 9, 16, 18, 19, 21).

Bertacca, D. (2020), *Generalization of the Kaiser Rocket effect in general relativity in the wide-angle galaxy 2-point correlation function*, en, International Journal of Modern Physics D **29** 2050085, ISSN: 0218-2718, 1793-6594, URL: https://www.worldscientific.com/doi/abs/10.1142/S0218271820500856 (visited on 07/07/2025) (cit. on p. 29).

Beutler, F. et al. (2014), *The clustering of galaxies in the SDSS-III Baryon Oscillation Spectroscopic Survey: testing gravity with redshift space distortions using the power spectrum multipoles*, Monthly Notices of the Royal Astronomical Society **443** 1065, Publisher: OUP ADS Bibcode: 2014MNRAS.443.1065B, ISSN: 0035-8711, URL: https://ui.adsabs.harvard.edu/abs/2014MNRAS.443.1065B (visited on 07/07/2025) (cit. on p. 32).

Bhavsar, S. P. (1978), *Inhomogeneities in the universe - an observed power law relating mass fraction to density enhancement*, en, The Astrophysical Journal **222** 412, ISSN: 0004-637X, 1538-4357, URL: http://adsabs.harvard.edu/doi/10.1086/156155 (visited on 07/07/2025) (cit. on p. 28).

Bianchi, D., H. Gil-Marín, R. Ruggeri and W. J. Percival (2015), *Measuring line-of-sight dependent Fourier-space clustering using FFTs*, Monthly Notices of the Royal Astronomical Society: Letters **453** L11, ISSN: 1745-3933, 1745-3925, arXiv: 1505.05341[astro-ph], URL: http://arxiv.org/abs/1505.05341 (visited on 10/03/2025) (cit. on pp. 31, 39).

Blake, C. and J. Wall (2002), *A velocity dipole in the distribution of radio galaxies*, en, Nature **416** 150, ISSN: 0028-0836, 1476-4687, URL: https://www.nature.com/articles/416150a (visited on 23/06/2025) (cit. on p. 2).

Blount, Z. D., R. E. Lenski and J. B. Losos (2018), *Contingency and determinism in evolution: Replaying life's tape*, en, Science **362** eaam5979, ISSN: 0036-8075, 1095-9203, URL: https://www.science.org/doi/10.1126/science.aam5979 (visited on 07/07/2025) (cit. on p. 27).

Borzyszkowski, M., D. Bertacca and C. Porciani (2017), *LIGER: mock relativistic light-cones from Newtonian simulations*, arXiv: 1703.03407, URL: http://arxiv.org/abs/1703.03407 (visited on 06/11/2024) (cit. on pp. 9, 20, 22, 32, 43, 44).

Bradley, J. (1728), *A Letter from the Reverend Mr. James Bradley Savilian Professor of Astronomy at Oxford, to Dr. Edmond Halley, Astronomer Royal, concerning an Apparent Motion observed in some of the Fixed Stars*, Philosophical Transactions of the Royal Society of London **35** 637 (cit. on p. 4).

Brooks, S., A. Gelman, G. Jones and X.-L. Meng, eds. (2011), *Handbook of Markov Chain Monte Carlo*, New York: Chapman and Hall/CRC, ISBN: 978-0-429-13850-8 (cit. on p. 58).

Bruni, M., J. C. Hidalgo, N. Meures and D. Wands (2014), *NON-GAUSSIAN INITIAL CONDITIONS IN CDM: NEWTONIAN, RELATIVISTIC, AND PRIMORDIAL CONTRIBUTIONS*, The Astrophysical Journal **785** 2, ISSN: 0004-637X, 1538-4357, URL: https://iopscience.iop.org/article/10.1088/0004-637X/785/1/2 (visited on 23/06/2025) (cit. on p. 10).

Buchert, T. and V. J. Martinez (1993), "What is a Fair Sample?", vol. 51 72, URL: https://ui.adsabs.harvard.edu/abs/1993ASPC...51...72B/abstract (visited on 07/07/2025) (cit. on p. 27).

Campanelli, L. (2009), *Model of universe anisotropization*, en, Physical Review D **80** 063006, ISSN: 1550-7998, 1550-2368, URL: https://link.aps.org/doi/10.1103/PhysRevD.80.063006 (visited on 27/09/2025) (cit. on p. 68).

Canuto, C., ed. (2007), *Spectral methods: evolution to complex geometries and applications to fluid dynamics*, Scientific computation, Berlin ; New York: Springer, ISBN: 978-3-540-30727-3 (cit. on p. 42).

Challinor, A. and A. Lewis (2011), *The linear power spectrum of observed source number counts*, Physical Review D **84** 043516, ISSN: 1550-7998, 1550-2368, arXiv: `1105.5292[astro-ph]`, URL: `http://arxiv.org/abs/1105.5292` (visited on 17/04/2025) (cit. on pp. 3, 12, 20).

Chisari, N. E. and M. Zaldarriaga (2011), *Connection between Newtonian simulations and general relativity*, en, Physical Review D **83** 123505, ISSN: 1550-7998, 1550-2368, URL: `https://link.aps.org/doi/10.1103/PhysRevD.83.123505` (visited on 23/06/2025) (cit. on p. 12).

Clifton, T., P. G. Ferreira, A. Padilla and C. Skordis (2012), *Modified Gravity and Cosmology*, arXiv:1106.2476, URL: `http://arxiv.org/abs/1106.2476` (visited on 25/11/2024) (cit. on p. 5).

Clifton, T., C. S. Gallagher, S. Goldberg and K. A. Malik (2020), *Viable Gauge Choices in Cosmologies with Non-Linear Structures*, Physical Review D **101** 063530, arXiv:2001.00394 [gr-qc], ISSN: 2470-0010, 2470-0029, URL: `http://arxiv.org/abs/2001.00394` (visited on 23/06/2025) (cit. on p. 10).

Cole, S., S. Hatton, D. H. Weinberg and C. S. Frenk (1998), *Mock 2dF and SDSS galaxy redshift surveys*, Monthly Notices of the Royal Astronomical Society **300** 945 (cit. on pp. 6, 87).

Coles, P. (2002), *Statistical Properties of Cosmological Fluctuations*, arXiv:astro-ph/0209590, URL: `http://arxiv.org/abs/astro-ph/0209590` (visited on 07/07/2025) (cit. on p. 27).

Coley, A. A. (2003), *Dynamical Systems and Cosmology*, en, Google-Books-ID: 0AZCcW8Au3kC, Springer Science & Business Media, ISBN: 978-1-4020-1403-1 (cit. on p. 68).

Curiel, E. (2015), *Measure, Topology and Probabilistic Reasoning in Cosmology*, arXiv:1509.01878 [gr-qc], URL: `http://arxiv.org/abs/1509.01878` (visited on 22/09/2025) (cit. on p. 27).

Dam, L., G. F. Lewis and B. J. Brewer (2023), *Testing the cosmological principle with CatWISE quasars: a bayesian analysis of the number-count dipole*, en, Monthly Notices of the Royal Astronomical Society **525** 231, ISSN: 0035-8711, 1365-2966, URL: `https://academic.oup.com/mnras/article/525/1/231/7235095` (visited on 23/06/2025) (cit. on pp. 2, 3, 58, 71, 87, 91).

Darling, J. (2022), *The Universe is Brighter in the Direction of Our Motion: Galaxy Counts and Fluxes are Consistent with the CMB Dipole*, The Astrophysical Journal Letters **931** L14, ISSN: 2041-8205, 2041-8213, URL: `https://iopscience.iop.org/article/10.3847/2041-8213/ac6f08` (visited on 23/06/2025) (cit. on pp. 2, 3, 71, 87, 91).

Davies, C. T., M. Cautun and B. Li (2018), *Weak lensing by voids in weak lensing maps*, arXiv: `1803.08717`, URL: `http://arxiv.org/abs/1803.08717` (visited on 25/11/2024) (cit. on p. 21).

Davis, M., G. Efstathiou, C. S. Frenk and S. D. M. White (1985), *The evolution of large-scale structure in a universe dominated by cold dark matter*, The Astrophysical Journal **292** 371, Publisher: IOP ADS Bibcode: 1985ApJ...292..371D, ISSN: 0004-637X, URL: `https://ui.adsabs.harvard.edu/abs/1985ApJ...292..371D` (visited on 15/04/2025) (cit. on p. 5).

De, A., S. Mandal, J. T. Beh, T.-H. Loo and P. K. Sahoo (2022), *Isotropization of locally rotationally symmetric Bianchi-I universe in $f(Q)$-gravity*, The European Physical Journal C **82** 72, arXiv:2201.05036 [gr-qc], ISSN: 1434-6044, 1434-6052, URL: `http://arxiv.org/abs/2201.05036` (visited on 27/09/2025) (cit. on p. 68).

DESI Collaboration et al. (2016), *The DESI Experiment Part I: Science,Targeting, and Survey Design*, arXiv:1611.00036 [astro-ph], URL: `http://arxiv.org/abs/1611.00036` (visited on 23/06/2025) (cit. on pp. 5, 6, 87).

Desjacques, V., D. Jeong and F. Schmidt (2018), *Large-Scale Galaxy Bias*, Physics Reports **733** 1, arXiv:1611.09787 [astro-ph], ISSN: 03701573, URL: `http://arxiv.org/abs/1611.09787` (visited on 07/07/2025) (cit. on p. 44).

Desjacques, V. and U. Seljak (2010), *Primordial Non-Gaussianity in the Large-Scale Structure of the Universe*, en, Advances in Astronomy **2010** 908640, ed. by D. Huterer, ISSN: 1687-7969, 1687-7977, URL: `https://onlinelibrary.wiley.com/doi/10.1155/2010/908640` (visited on 23/06/2025) (cit. on p. 5).

Domènech, G., R. Mohayaee, S. P. Patil and S. Sarkar (2022), *Galaxy number-count dipole and superhorizon fluctuations*, en, Journal of Cosmology and Astroparticle Physics **2022** 019, Publisher: IOP Publishing, ISSN: 1475-7516, URL: `https://doi.org/10.1088/1475-7516/2022/10/019` (visited on 27/09/2025) (cit. on p. 69).

Doran, M. (2005), *CMBEASY:: an Object Oriented Code for the Cosmic Microwave Background*, Journal of Cosmology and Astroparticle Physics **2005** 011, arXiv:astro-ph/0302138, ISSN: 1475-7516, URL: `http://arxiv.org/abs/astro-ph/0302138` (visited on 07/07/2025) (cit. on p. 41).

Dutka, J. (1995), *On the Early History of Bessel Functions*, Archive for History of Exact Sciences **49** 105, Publisher: Springer, ISSN: 0003-9519, URL: `https://www.jstor.org/stable/41134001` (visited on 07/07/2025) (cit. on p. 29).

Eisenhardt, P. R. M. et al. (2020), *The CatWISE Preliminary Catalog: Motions from WISE and NEOWISE Data*, The Astrophysical Journal Supplement Series **247** 69, ISSN: 0067-0049, 1538-4365, URL: `https://iopscience.iop.org/article/10.3847/1538-4365/ab7f2a` (visited on 23/06/2025) (cit. on p. 2).

Elkhashab, M. Y., D. Bertacca et al. (2024), *Euclid preparation. The impact of relativistic redshift-space distortions on two-point clustering statistics from the Euclid wide spectroscopic survey*, arXiv: `2410.00956[astro-ph]`, URL: `http://arxiv.org/abs/2410.00956` (visited on 12/12/2024) (cit. on pp. 6, 55).

Elkhashab, M. Y., C. Porciani and D. Bertacca (2021), *The large-scale monopole of the power spectrum in a Euclid-like survey: wide-angle effects, lensing, and the ‘finger of the observer’*, Monthly Notices of the Royal Astronomical Society **509** 1626, ISSN: 0035-8711, 1365-2966, arXiv: `2108.13424[astro-ph]`, URL: `http://arxiv.org/abs/2108.13424` (visited on 11/12/2024) (cit. on pp. 9, 20, 23, 32).

– (2024), *Measuring our peculiar velocity from spectroscopic redshift surveys*, URL: `http://arxiv.org/abs/2412.03953` (visited on 03/04/2025) (cit. on pp. 1, 2, 5, 22, 28, 32, 34, 37, 42, 58, 69–71, 91).

Elkhashab, M. Y. (2024), *Relativistic redshift-space distortions in stage iv galaxy surveys*, en, PhD thesis: Universita degli Studi di Padova, URL: `https://www.research.unipd.it/retrieve/e3943e65-9910-4592-9c82-7ac39aa85162/FINAL_THESIS_MOHAMED_YOUSRY_ABDELLATIF_ELKHASAB_AFTER_REVIEW.pdf` (cit. on p. 36).

Ellis, G. F. R. and J. E. Baldwin (1984), *On the expected anisotropy of radio source counts*, en, Monthly Notices of the Royal Astronomical Society **206** 377, ISSN: 0035-8711, 1365-2966, URL: `https://academic.oup.com/mnras/article-lookup/doi/10.1093/mnras/206.2.377` (visited on 23/06/2025) (cit. on p. 2).

Ellis, G. F. R. (2006), *Issues in the Philosophy of Cosmology*, arXiv:astro-ph/0602280, URL: `http://arxiv.org/abs/astro-ph/0602280` (visited on 07/07/2025) (cit. on p. 27).

Ellis, G. F. R. (2014), *On the philosophy of cosmology*, en, Studies in History and Philosophy of Science Part B: Studies in History and Philosophy of Modern Physics **46** 5, ISSN: 13552198, URL: `https://linkinghub.elsevier.com/retrieve/pii/S1355219813000671` (visited on 30/06/2025) (cit. on p. 27).

Erickcek, A. L. (2008), *Superhorizon perturbations and the cosmic microwave background*, Physical Review D **78** (cit. on p. 69).

Euclid Collaboration et al. (2025), *Euclid. I. Overview of the Euclid mission*, Astronomy & Astrophysics **697** A1, arXiv:2405.13491 [astro-ph], ISSN: 0004-6361, 1432-0746, URL: `http://arxiv.org/abs/2405.13491` (visited on 23/06/2025) (cit. on pp. 1, 65, 68, 90).

Feldman, H. A., N. Kaiser and J. A. Peacock (1994), *Power Spectrum Analysis of Three-Dimensional Redshift Surveys*, The Astrophysical Journal **426** 23, ISSN: 0004-637X, 1538-4357, arXiv: `astro-ph/9304022`, URL: `http://arxiv.org/abs/astro-ph/9304022` (visited on 16/03/2025) (cit. on p. 31).

Ferlito, F. et al. (2024), *Ray-tracing vs. Born approximation in full-sky weak lensing simulations of the MillenniumTNG project*, arXiv: `2406.08540[astro-ph]`, URL: `http://arxiv.org/abs/2406.08540` (visited on 09/12/2024) (cit. on p. 42).

Ferreira, P. d. S. and V. Marra (2024), *Tomographic redshift dipole: Testing the cosmological principle*, Journal of Cosmology and Astroparticle Physics **2024** 077, arXiv:2403.14580 [astro-ph], ISSN: 1475-7516, URL: `http://arxiv.org/abs/2403.14580` (visited on 27/09/2025) (cit. on pp. 3, 71, 87, 91).

Foreman-Mackey, D., D. W. Hogg, D. Lang and J. Goodman (2013), *emcee: The MCMC Hammer*, en, Publications of the Astronomical Society of the Pacific **125** 306, Publisher: IOP Publishing, ISSN: 1538-3873, URL: `https://iopscience.iop.org/article/10.1086/670067/meta` (visited on 22/09/2025) (cit. on p. 58).

Frigo, M. and S. G. Johnson (2005), *The Design and Implementation of FFTW3*, Proceedings of the IEEE **93** 216, Special issue on “Program Generation, Optimization, and Platform Adaptation” (cit. on p. 42).

Gibelyou, C. and D. Huterer (2012), *Dipoles in the sky: Dipoles in the sky*, en, Monthly Notices of the Royal Astronomical Society **427** 1994, ISSN: 00358711, 13652966, URL: `https://academic.oup.com/mnras/article-lookup/doi/10.1111/j.1365-2966.2012.22032.x` (visited on 23/06/2025) (cit. on p. 2).

Giesel, E., R. Reischke, B. M. Schäfer and D. Chia (2021), *Information geometry in cosmological inference problems*, Journal of Cosmology and Astroparticle Physics **2021** 005, arXiv:2005.01057 [gr-qc], ISSN: 1475-7516, URL: `http://arxiv.org/abs/2005.01057` (visited on 07/07/2025) (cit. on p. 28).

Gomes, H. D. A. (2025), *Gauge Theory and the Geometrisation of Physics*, 1st ed., Cambridge University Press, ISBN: 978-1-00-902930-8 978-1-00-954811-3 978-1-00-901408-3, URL: `https://www.cambridge.org/core/product/identifier/9781009029308/type/element` (visited on 23/06/2025) (cit. on p. 10).

Goodman, J. and J. Weare (2010), *Ensemble samplers with affine invariance*, en, Communications in Applied Mathematics and Computational Science **5** 65, ISSN: 2157-5452, 1559-3940, URL: `http://msp.org/camcos/2010/5-1/p04.xhtml` (visited on 22/09/2025) (cit. on p. 58).

Gott III, J. R. et al. (2005), *A Map of the Universe*, The Astrophysical Journal **624** 463 (cit. on pp. 6, 87).

Green, S. R. and R. M. Wald (2012), *Newtonian and relativistic cosmologies*, en, Physical Review D **85** 063512, ISSN: 1550-7998, 1550-2368, URL: `https://link.aps.org/doi/10.1103/PhysRevD.85.063512` (visited on 23/06/2025) (cit. on p. 10).

Grimm, N., C. Bonvin and I. Tutusaus (2024), *Testing General Relativity through the E_G Statistic Using the Weyl Potential and Galaxy Velocities*, Physical Review Letters **133** 211004, arXiv:2403.13709 [astro-ph], ISSN: 0031-9007, 1079-7114, URL: `http://arxiv.org/abs/2403.13709` (visited on 24/06/2025) (cit. on p. 22).

Hahn, O. and T. Abel (2011), *Multi-scale initial conditions for cosmological simulations*, Monthly Notices of the Royal Astronomical Society **415** 2101, ISSN: 0035-8711, URL: `https://ui.adsabs.harvard.edu/abs/2011MNRAS.415.2101H` (visited on 07/07/2025) (cit. on p. 40).

Hahn, O., F. List and N. Porqueres (2024), *DISCO-DJ I: a differentiable Einstein-Boltzmann solver for cosmology*, Journal of Cosmology and Astroparticle Physics **2024** 063, arXiv:2311.03291 [astro-ph], ISSN: 1475-7516, URL: `http://arxiv.org/abs/2311.03291` (visited on 07/07/2025) (cit. on p. 41).

Hahn, O., M. Michaux, C. Rampf, C. Uhlemann and R. E. Angulo (2020), *MUSIC2-monofonIC: 3LPT initial condition generator*, Astrophysics Source Code Library ascl:2008.024, ADS Bibcode: 2020ascl.soft08024H, URL: `https://ui.adsabs.harvard.edu/abs/2020ascl.soft08024H` (visited on 07/07/2025) (cit. on p. 40).

Hamilton, A. J. S. (1992), *Measuring Omega and the real correlation function from the redshift correlation function*, en, The Astrophysical Journal **385** L5, ISSN: 0004-637X, 1538-4357, URL: `http://adsabs.harvard.edu/doi/10.1086/186264` (visited on 30/06/2025) (cit. on p. 29).

– (1998), *Linear Redshift Distortions: a Review*, NATO ASI Series C **. . . , (No. 231)** 185, ed. by D. Hamilton (cit. on pp. 1, 5).

Hamilton, A. J. S. and M. Culhane (1997), *Spherical Redshift Distortions*, arXiv:astro-ph/9507021, URL: `http://arxiv.org/abs/astro-ph/9507021` (visited on 30/06/2025) (cit. on p. 29).

Hand, N., Y. Li, Z. Slepian and U. Seljak (2017), *An optimal FFT-based anisotropic power spectrum estimator*, Journal of Cosmology and Astroparticle Physics **2017** 002, ISSN: 1475-7516, arXiv: `1704.02357[astro-ph]`, URL: `http://arxiv.org/abs/1704.02357` (visited on 24/03/2025) (cit. on p. 39).

Hartlap, J., P. Simon and P. Schneider (2007), *Why your model parameter confidences might be too optimistic – unbiased estimation of the inverse covariance matrix*, Astronomy & Astrophysics **464** 399, arXiv:astro-ph/0608064, ISSN: 0004-6361, 1432-0746, URL: `http://arxiv.org/abs/astro-ph/0608064` (visited on 22/09/2025) (cit. on p. 59).

Heideman, M. T., D. H. Johnson and C. S. Burrus (1985), *Gauss and the history of the fast Fourier transform*, en, Archive for History of Exact Sciences **34** 265, ISSN: 0003-9519, 1432-0657, URL: `http://link.springer.com/10.1007/BF00348431` (visited on 07/07/2025) (cit. on p. 37).

Hockney, R. and J. Eastwood (2021), *Computer Simulation Using Particles*, en, 0th ed., CRC Press, ISBN: 978-0-367-80693-4, URL: `https://www.taylorfrancis.com/books/9781439822050` (visited on 07/07/2025) (cit. on pp. 37, 39).

Holmberg, E. (1941), *On the Clustering Tendencies among the Nebulae. II. A Study of Encounters Between Laboratory Models of Stellar Systems by a New Integration Procedure*, Astrophysical Journal **94** 385 (cit. on p. 5).

Hopersky, A. N., A. M. Nadolinsky and R. V. Koneev (2025), *On summation of $3j$-Wigner symbols*, arXiv:2504.11567 [physics], URL: `http://arxiv.org/abs/2504.11567` (visited on 07/07/2025) (cit. on p. 35).

Hu, B., M. Raveri, N. Frusciante and A. Silvestri (2014), *Effective Field Theory of Cosmic Acceleration: an implementation in CAMB*, Physical Review D **89** 103530, arXiv:1312.5742 [astro-ph], ISSN: 1550-7998, 1550-2368, URL: `http://arxiv.org/abs/1312.5742` (visited on 07/07/2025) (cit. on p. 41).

Hubble, E. (1937), *The Observational Approach to Cosmology*, en, Oxford, URL: `https://ned.ipac.caltech.edu/level5/Sept04/Hubble/paper.pdf` (cit. on p. 27).

Huggett, N., C. Hoefer and J. Read (2024), "Absolute and Relational Space and Motion: Post-Newtonian Theories", *The Stanford Encyclopedia of Philosophy*, ed. by E. N. Zalta and U. Nodelman, Fall 2024, Metaphysics Research Lab, Stanford University, URL: `https://plato.stanford.edu/archives/fall2024/entries/spacetime-theories/` (visited on 07/07/2025) (cit. on p. 2).

Jeong, D., F. Schmidt and C. M. Hirata (2012), *Large-scale clustering of galaxies in general relativity*, Physical Review D **85** 023504, ISSN: 1550-7998, 1550-2368, arXiv: `1107.5427[astro-ph]`, URL: `http://arxiv.org/abs/1107.5427` (visited on 17/04/2025) (cit. on pp. 3, 12, 15).

Jimenez, J. B. and A. L. Maroto (2009), *Large-scale cosmic flows and moving dark energy*, Journal of Cosmology and Astroparticle Physics **2009** 015, arXiv:0811.3606 [astro-ph], ISSN: 1475-7516, URL: `http://arxiv.org/abs/0811.3606` (visited on 27/09/2025) (cit. on p. 69).

Kaiser, N. (1984), *On the spatial correlations of Abell clusters.*, The Astrophysical Journal **284** L9, Publisher: IOP ADS Bibcode: 1984ApJ...284L...9K, ISSN: 0004-637X, URL: `https://ui.adsabs.harvard.edu/abs/1984ApJ...284L...9K` (visited on 15/04/2025) (cit. on p. 21).

Kaiser, N. (1987), *Clustering in Real Space and in Redshift Space*, Monthly Notices of the Royal Astronomical Society **227** 1 (cit. on pp. 5, 29).

Kovalevsky, J. (2003), *Aberration in proper motions*, Astronomy & Astrophysics **404** 743, ISSN: 0004-6361, 1432-0746, URL: `http://www.aanda.org/10.1051/0004-6361:20030560` (visited on 23/06/2025) (cit. on p. 4).

Kragh, H. (1999), *Cosmology and controversy: the historical development of two theories of the universe*, eng, Princeton, NJ: Princeton University Press, ISBN: 978-0-691-00546-1 978-0-691-22771-9 (cit. on p. 27).

Kristian, J. and R. K. Sachs (1966), *Observations in Cosmology*, Astrophysical Journal **143** 379 (cit. on p. 4).

Lapparent, V. de, M. J. Geller and J. P. Huchra (1986), *A Slice of the Universe*, The Astrophysical Journal **302** L1, Publisher: IOP ADS Bibcode: 1986ApJ...302L...1D, ISSN: 0004-637X, URL: `https://ui.adsabs.harvard.edu/abs/1986ApJ...302L...1D` (visited on 15/04/2025) (cit. on pp. 5, 6, 87).

Legendre, A. M. (1785), *Recherches sur l´attraction des spheroides homogenes*, fra, Mémoires de mathématique et de physique : prés. à l´Académie Royale des Sciences, par divers savans, et lûs dans ses assemblées **1785** 411, URL: `http://publikationen.ub.uni-frankfurt.de/frontdoor/index/index/docId/16049` (visited on 07/07/2025) (cit. on p. 29).

Lesgourgues, J. (2011), *The Cosmic Linear Anisotropy Solving System (CLASS) I: Overview*, URL: `http://arxiv.org/abs/1104.2932` (visited on 07/07/2025) (cit. on p. 41).

Lewis, A., A. Challinor and A. Lasenby (2000), *Efficient Computation of CMB anisotropies in closed FRW models*, The Astrophysical Journal **538** 473, arXiv:astro-ph/9911177, ISSN: 0004-637X, 1538-4357, URL: `http://arxiv.org/abs/astro-ph/9911177` (visited on 07/07/2025) (cit. on p. 41).

Limber, D. N. (1953), *Fluctuations in Brightness of the Milky way.*, en, The Astrophysical Journal **117** 145, ISSN: 0004-637X, 1538-4357, URL: `http://adsabs.harvard.edu/doi/10.1086/145673` (visited on 07/07/2025) (cit. on p. 28).

Lineweaver, C. H. (1996), *The CMB Dipole: The Most Recent Measurement And Some History*, arXiv:astro-ph/9609034, URL: `http://arxiv.org/abs/astro-ph/9609034` (visited on 23/06/2025) (cit. on p. 1).

Longair, M. S. (2006), *The cosmic century: a history of astrophysics and cosmology*, Cambridge, UK ; New York: Cambridge University Press, ISBN: 978-0-521-47436-8 (cit. on p. 27).

Ma, C.-P. and E. Bertschinger (1994), *Cosmological Perturbation Theory in the Synchronous vs. Conformal Newtonian Gauge*, arXiv: `astro-ph/9401007`, URL: `http://arxiv.org/abs/astro-ph/9401007` (visited on 06/11/2024) (cit. on p. 10).

Maartens, R. et al. (2021), *Magnification and evolution biases in large-scale structure surveys*, Journal of Cosmology and Astroparticle Physics **2021** 009 (cit. on pp. 44–48, 88).

Mann, R. G., J. A. Peacock and A. F. Heavens (1998), *Eulerian Bias and the Galaxy Density Field*, Monthly Notices of the Royal Astronomical Society **293** 209 (cit. on p. 21).

Mattia, A. d. and V. Ruhlmann-Kleider (2019), *Integral constraints in spectroscopic surveys*, Journal of Cosmology and Astroparticle Physics **2019** 036, arXiv:1904.08851 [astro-ph], ISSN: 1475-7516, URL: `http://arxiv.org/abs/1904.08851` (visited on 07/07/2025) (cit. on pp. 32, 33).

Mehrem, R. (2011), *The Plane Wave Expansion, Infinite Integrals and Identities involving Spherical Bessel Functions*, arXiv:0909.0494 [math-ph], URL: `http://arxiv.org/abs/0909.0494` (visited on 07/07/2025) (cit. on p. 35).

Mittal, V., O. T. Oayda and G. F. Lewis (2023), *The Cosmic Dipole in the Quaia Sample of Quasars: A Bayesian Analysis*, Monthly Notices of the Royal Astronomical Society **527** 8497, arXiv:2311.14938 [astro-ph], ISSN: 0035-8711, 1365-2966, URL: `http://arxiv.org/abs/2311.14938` (visited on 27/09/2025) (cit. on pp. 3, 71, 87, 91).

Munitz, M. K. (1962), *THE LOGIC OF COSMOLOGY*, en, The British Journal for the Philosophy of Science **13** 34, ISSN: 0007-0882, 1464-3537, URL: `https://www.journals.uchicago.edu/doi/10.1093/bjps/XIII.49.34` (visited on 30/06/2025) (cit. on p. 27).

Nadolny, T., R. Durrer, M. Kunz and H. Padmanabhan (2021), *A new way to test the Cosmological Principle: measuring our peculiar velocity and the large scale anisotropy independently*, Journal of Cosmology and Astroparticle Physics **2021** 009, arXiv:2106.05284 [astro-ph], ISSN: 1475-7516, URL: `http://arxiv.org/abs/2106.05284` (visited on 07/07/2025) (cit. on p. 34).

Neyman, J., E. L. Scott and C. D. Shane (1956), "Statistics of Images of Galaxies with Particular Reference to Clustering", *Proceedings of the Third Berkeley Symposium on Mathematical Statistics and Probability, Volume 3: Contributions to Astronomy and Physics*, vol. 3.3, University of California Press 75, URL: `https://projecteuclid.org/ebooks/berkeley-symposium-on-mathematical-statistics-and-probability/Proceedings-of-the-Third-Berkeley-Symposium-on-Mathematical-Statistics-and/chapter/Statistics-of-Images-of-Galaxies-with-Particular-Reference-to-Clustering/bsmsp/1200502191` (visited on 07/07/2025) (cit. on pp. 28, 54).

Nishizawa, A. J. (2014), *Integrated Sachs Wolfe Effect and Rees Sciama Effect*, Progress of Theoretical and Experimental Physics **2014** 6B110, arXiv:1404.5102 [astro-ph], ISSN: 2050-3911, URL: `http://arxiv.org/abs/1404.5102` (visited on 24/06/2025) (cit. on p. 22).

Nuske, R. S., S. Sprauer and J. Saborowski (2009), *Adapting the pair-correlation function for analysing the spatial distribution of canopy gaps*, en, Forest Ecology and Management **259** 107, ISSN:

03781127, URL: `https://linkinghub.elsevier.com/retrieve/pii/S0378112709007129` (visited on 07/07/2025) (cit. on p. 28).

Pain, J.-C. (2020), *Some properties of Wigner 3j coefficients: non-trivial zeros and connections to hypergeometric functions*, en, The European Physical Journal A **56** 296, ISSN: 1434-601X, URL: `https://doi.org/10.1140/epja/s10050-020-00303-9` (visited on 07/07/2025) (cit. on p. 35).

Peacock, J. A. (1991), *The power spectrum of galaxy clustering*, Monthly Notices of the Royal Astronomical Society **253** 1P, ISSN: 0035-8711, URL: `https://doi.org/10.1093/mnras/253.1.1P` (visited on 07/07/2025) (cit. on p. 32).

Peebles, P. J. E. (2020), *The Large-Scale Structure of the Universe*, eng, Princeton Series in Physics 98, Princeton, NJ: Princeton University Press, ISBN: 978-0-691-20671-4 (cit. on pp. 7, 23, 27, 28).

– (2022), *The Whole Truth: A Cosmologist's Reflections on the Search for Objective Reality*, eng, 1st ed, Princeton: Princeton University Press, ISBN: 978-0-691-23135-8 978-0-691-23136-5 (cit. on p. 3).

Pharr, M. and G. Humphreys (2010), *Physically based rendering: from theory to implementation*, eng, 2nd ed, Burlington, MA: Morgan Kaufmann/Elsevier, ISBN: 978-0-12-375079-2 (cit. on p. 39).

Planck Collaboration et al. (2020), *Planck 2018 results: I. Overview and the cosmological legacy of Planck*, Astronomy & Astrophysics **641** A1, ISSN: 0004-6361, 1432-0746, URL: `https://www.aanda.org/10.1051/0004-6361/201833880` (visited on 23/06/2025) (cit. on pp. 2, 3, 43, 71, 87, 91).

Pontzen, A. (2016), *Bianchi universes*, en, Scholarpedia **11** 32340, ISSN: 1941-6016, URL: `http://www.scholarpedia.org/article/Bianchi_universes` (visited on 27/09/2025) (cit. on p. 68).

Pourojaghi, S., M. Malekjani and Z. Davari (2024), *Cosmological constraints on dark energy parametrizations after DESI 2024: Persistent deviation from standard ΛCDM cosmology*, en, arXiv:2407.09767 [astro-ph, physics:gr-qc], URL: `http://arxiv.org/abs/2407.09767` (visited on 14/08/2024) (cit. on p. 28).

Pozzetti, L. et al. (2016), *Modelling the number density of H emitters for future spectroscopic near-IR space missions*, Astronomy & Astrophysics **590** A3, ISSN: 0004-6361, 1432-0746, URL: `http://www.aanda.org/10.1051/0004-6361/201527081` (visited on 20/01/2025) (cit. on p. 44).

Prat, J. and D. Bacon (2025), *Weak Gravitational Lensing*, arXiv:2501.07938 [astro-ph], URL: `http://arxiv.org/abs/2501.07938` (visited on 23/06/2025) (cit. on pp. 18, 21).

Reimberg, P., F. Bernardeau and C. Pitrou (2016), *Redshift-space distortions with wide angular separations*, Journal of Cosmology and Astroparticle Physics **2016** 048, ISSN: 1475-7516, URL: `https://iopscience.iop.org/article/10.1088/1475-7516/2016/01/048` (visited on 07/07/2025) (cit. on pp. 32, 33, 88).

Ripley, B. D. (1977), *Modelling Spatial Patterns*, en, Journal of the Royal Statistical Society Series B: Statistical Methodology **39** 172, ISSN: 1369-7412, 1467-9868, URL: `https://academic.oup.com/jrsssb/article/39/2/172/7027573` (visited on 07/07/2025) (cit. on p. 28).

Roux, M. C. N., B. A. H. Meunier and D. Mari (2023), *Study of Faraday waves in tanks in presence of polystyrene bead layers*, Emergent Scientist **7** 2, ISSN: 2556-8779, URL: `https://emergent-scientist.edp-open.org/10.1051/emsci/2023001` (visited on 07/07/2025) (cit. on p. 44).

Saadeh, D., S. M. Feeney, A. Pontzen, H. V. Peiris and J. D. McEwen (2016), *How isotropic is the Universe?*, Physical Review Letters **117** 131302, arXiv:1605.07178 [astro-ph], ISSN: 0031-9007, 1079-7114, URL: `http://arxiv.org/abs/1605.07178` (visited on 27/09/2025) (cit. on p. 68).

Sachs, R. K. and A. M. Wolfe (1967), *Perturbations of a Cosmological Model and Angular Variations of the Microwave Background*, en, The Astrophysical Journal **147** 73, ISSN: 0004-637X, 1538-4357, URL: `http://adsabs.harvard.edu/doi/10.1086/148982` (visited on 24/06/2025) (cit. on p. 22).

Santos, M. G., D. Alonso, P. Bull, M. Silva and S. Yahya (2015), *HI galaxy simulations for the SKA: number counts and bias*, arXiv:1501.03990 [astro-ph], URL: `http://arxiv.org/abs/1501.03990` (visited on 27/09/2025) (cit. on p. 46).

Schaffner, K. F. (1972), *Nineteenth-century aether theories*, 1st ed., The Commonwealth and international library. Selected readings in physics, Oxford, New York: Pergamon Press, ISBN: 978-0-08-015674-3 (cit. on p. 4).

Schaye, J. et al. (2023), *The FLAMINGO project: cosmological hydrodynamical simulations for large-scale structure and galaxy cluster surveys*, Monthly Notices of the Royal Astronomical Society **526** 4978, arXiv:2306.04024 [astro-ph], ISSN: 0035-8711, 1365-2966, URL: `http://arxiv.org/abs/2306.04024` (visited on 23/06/2025) (cit. on pp. 5, 44).

Schimd, C. (2009), *Signatures of dark energy on LSS*, EAS Publications Series **36** 33, ISSN: 1633-4760, 1638-1963, URL: `http://www.eas-journal.org/10.1051/eas/0936005` (visited on 23/06/2025) (cit. on p. 5).

Schindler, S. (2002), *Omega_m - Different Ways to Determine the Matter Density of the Universe*, Space Science Reviews **100** 299, arXiv:astro-ph/0107028, ISSN: 0038-6308, 1572-9672, URL: `http://arxiv.org/abs/astro-ph/0107028` (visited on 04/10/2025) (cit. on p. 71).

Schlick, M. (2007), *Space and time in contemporary physics: an introduction to the theory of relativity and gravitation*, eng, Great minds series, Amherst, NY: Prometheus Books, ISBN: 978-1-59102-417-0 (cit. on p. 4).

Schmidt, F. and D. Jeong (2012), *Cosmic Rulers*, Physical Review D **86** 083527, arXiv:1204.3625 [astro-ph], ISSN: 1550-7998, 1550-2368, URL: `http://arxiv.org/abs/1204.3625` (visited on 23/06/2025) (cit. on pp. 12, 15, 18).

Scoccimarro, R. (2015), *Fast Estimators for Redshift-Space Clustering*, Physical Review D **92** 083532, ISSN: 1550-7998, 1550-2368, arXiv: `1506.02729[astro-ph]`, URL: `http://arxiv.org/abs/1506.02729` (visited on 03/02/2025) (cit. on p. 39).

Secrest, N. J., S. Von Hausegger, M. Rameez, R. Mohayaee and S. Sarkar (2022), *A Challenge to the Standard Cosmological Model*, The Astrophysical Journal Letters **937** L31, ISSN: 2041-8205, 2041-8213, URL: `https://iopscience.iop.org/article/10.3847/2041-8213/ac88c0` (visited on 23/06/2025) (cit. on p. 2).

Seljak, U. and M. Zaldarriaga (1999), *CMBFAST: A microwave anisotropy code*, Astrophysics Source Code Library ascl:9909.004, ADS Bibcode: 1999ascl.soft09004S, URL: `https://ui.adsabs.harvard.edu/abs/1999ascl.soft09004S` (visited on 07/07/2025) (cit. on p. 41).

Shapiro, I. I. (1964), *Fourth Test of General Relativity*, Physical Review Letters **13** 789 (cit. on p. 22).

Sheth, R. K. and A. Diaferio (2001), *Peculiar velocities of galaxies and clusters*, Monthly Notices of the Royal Astronomical Society **322** 901, ISSN: 0035-8711, URL: `https://doi.org/10.1046/j.1365-8711.2001.04202.x` (visited on 22/09/2025) (cit. on p. 58).

Singal, A. (2021), *Our Peculiar Motion Inferred from Number Counts of Mid Infra Red AGNs and the Discordance Seen with the Cosmological Principle*, en, Universe **7** 107, ISSN: 2218-1997, URL: `https://www.mdpi.com/2218-1997/7/4/107` (visited on 23/06/2025) (cit. on p. 2).

Sommerfeld, A. (1896), *Mathematische Theorie der Diffraction*, de, Mathematische Annalen **47** 317, ISSN: 1432-1807, URL: `https://doi.org/10.1007/BF01447273` (visited on 07/07/2025) (cit. on p. 35).

Springel, V. (2005), *The cosmological simulation code GADGET-2*, Monthly Notices of the Royal Astronomical Society **364** 1105, Publisher: OUP ADS Bibcode: 2005MNRAS.364.1105S, ISSN: 0035-8711, URL: `https://ui.adsabs.harvard.edu/abs/2005MNRAS.364.1105S` (visited on 07/07/2025) (cit. on p. 41).

Stewart, G. W. (1992), *On the early history of the singular value decomposition*, en, URL: `https://hdl.handle.net/11299/1868` (visited on 26/09/2025) (cit. on p. 64).

Stewart, J. M. and D. W. Sciama (1967), *Peculiar Velocity of the Sun and its Relation to the Cosmic Microwave Background*, en, Nature **216** 748, ISSN: 0028-0836, 1476-4687, URL: `https://www.nature.com/articles/216748a0` (visited on 23/06/2025) (cit. on p. 2).

Strutt, J. W. (1877), *The Theory of Sound: Volume 2*, eng, Cambridge library collection. Physical Sciences, Cambridge: Cambridge University Press, ISBN: 978-1-108-03221-6 978-1-139-05809-4 (cit. on p. 35).

Synge, J. L. (1960), *Relativity: The General Theory*, Amsterdam: North-Holland Publishing Co. (cit. on p. 15).

Szalay, A. S., T. Matsubara and S. D. Landy (1998), *Redshift Space Distortions of the Correlation Function in Wide Angle Galaxy Surveys*, The Astrophysical Journal **498** L1, arXiv:astro-ph/9712007, ISSN: 0004637X, URL: `http://arxiv.org/abs/astro-ph/9712007` (visited on 07/07/2025) (cit. on p. 29).

Tam, S. M. (1985), *On Covariance in Finite Population Sampling*, Journal of the Royal Statistical Society. Series D (The Statistician) **34** 429, Publisher: [Royal Statistical Society, Wiley], ISSN: 0039-0526, URL: `https://www.jstor.org/stable/2987828` (visited on 22/09/2025) (cit. on p. 59).

Tegmark, M. and P. J. E. Peebles (1998), *The Time Evolution of Bias*, Astrophysical Journal Letters **500** L79 (cit. on p. 21).

Tegmark, M., A. Taylor and A. Heavens (1997), *Karhunen-Loeve eigenvalue problems in cosmology: how should we tackle large data sets?*, The Astrophysical Journal **480** 22, arXiv:astro-ph/9603021, ISSN: 0004-637X, 1538-4357, URL: `http://arxiv.org/abs/astro-ph/9603021` (visited on 26/09/2025) (cit. on p. 64).

Tiwari, P. et al. (2024), *An Independent Measure of the Kinematic Dipole from SDSS*, en, The Astrophysical Journal **975** 279, Publisher: The American Astronomical Society, ISSN: 0004-637X, URL: `https://doi.org/10.3847/1538-4357/ad815b` (visited on 27/09/2025) (cit. on pp. 3, 71, 87, 91).

Toussaint, U. von (2011), *Bayesian inference in physics*, Reviews of Modern Physics **83** 943 (cit. on p. 57).

Turner, M. S. (1991), *Tilted Universe and other remnants of the preinflationary Universe*, en, Physical Review D **44** 3737, ISSN: 0556-2821, URL: `https://link.aps.org/doi/10.1103/PhysRevD.44.3737` (visited on 27/09/2025) (cit. on p. 69).

Vogelsberger, M., S. Genel et al. (2014), *Introducing the Illustris Project: Simulating the coevolution of dark and visible matter in the Universe*, Monthly Notices of the Royal Astronomical Society

444 1518, arXiv:1405.2921 [astro-ph], ISSN: 0035-8711, 1365-2966, URL: `http://arxiv.org/abs/1405.2921` (visited on 07/07/2025) (cit. on p. 44).

Vogelsberger, M., F. Marinacci, P. Torrey and E. Puchwein (2019), *Cosmological Simulations of Galaxy Formation*, arXiv: `1909.07976[astro-ph]`, URL: `http://arxiv.org/abs/1909.07976` (visited on 06/03/2025) (cit. on p. 43).

Wainwright, J., A. A. Coley, G. F. R. Ellis and M. Hancock (1998), *On the isotropy of the Universe: do Bianchi VIIh cosmologies isotropize?*, Class. Quant. Grav. **15** 331 (cit. on p. 68).

Wang, D. (2024), *The Self-Consistency of DESI Analysis and Comment on "Does DESI 2024 Confirm ΛCDM?"*, en, arXiv:2404.13833 [astro-ph, physics:gr-qc, physics:hep-ph, physics:hep-th], URL: `http://arxiv.org/abs/2404.13833` (visited on 14/08/2024) (cit. on pp. 41, 70).

Wigner, E. P. (1993), "On the Matrices Which Reduce the Kronecker Products of Representations of S. R. Groups", en, *The Collected Works of Eugene Paul Wigner*, ed. by A. S. Wightman, Berlin, Heidelberg: Springer Berlin Heidelberg 608, ISBN: 978-3-642-08154-5 978-3-662-02781-3, URL: `http://link.springer.com/10.1007/978-3-662-02781-3_42` (visited on 07/07/2025) (cit. on p. 35).

Wishart, J. (1928), *The Generalised Product Moment Distribution in Samples from a Normal Multivariate Population*, Biometrika **20A** 32, Publisher: [Oxford University Press, Biometrika Trust], ISSN: 0006-3444, URL: `https://www.jstor.org/stable/2331939` (visited on 22/09/2025) (cit. on p. 59).

Yahya, S. et al. (2015), *Cosmological performance of SKA Hi galaxy surveys*, Monthly Notices of the Royal Astronomical Society **450** 2251, ISSN: 0035-8711, URL: `https://doi.org/10.1093/mnras/stv695` (visited on 27/09/2025) (cit. on pp. 46, 47).

Yamamoto, K. (2003), *Optimal Weighting Scheme in Redshift-Space Power Spectrum Analysis and a Prospect for Measuring the Cosmic Equation of State*, en, The Astrophysical Journal **595** 577, ISSN: 0004-637X, 1538-4357, URL: `https://iopscience.iop.org/article/10.1086/377488` (visited on 07/07/2025) (cit. on p. 31).

Yamamoto, K., M. Nakamichi, A. Kamino, B. A. Bassett and H. Nishioka (2006), *A Measurement of the Quadrupole Power Spectrum in the Clustering of the 2dF QSO Survey*, Publications of the Astronomical Society of Japan **58** 93, ISSN: 0004-6264, 2053-051X, arXiv: `astro-ph/0505115`, URL: `http://arxiv.org/abs/astro-ph/0505115` (visited on 16/03/2025) (cit. on pp. 32, 34).

Yamamoto, K., H. Nishioka and A. Taruya (2000), *The effect of bias and redshift distortions on a geometric test for the cosmological constant*, arXiv:astro-ph/0012433, URL: `http://arxiv.org/abs/astro-ph/0012433` (visited on 07/07/2025) (cit. on p. 32).

Yip, J. H. T., A. Rouhiainen and G. Shiu (2025), *Learning from Topology: Cosmological Parameter Estimation from the Large-scale Structure*, Machine Learning: Science and Technology **6** 025063, arXiv:2308.02636 [astro-ph], ISSN: 2632-2153, URL: `http://arxiv.org/abs/2308.02636` (visited on 07/07/2025) (cit. on p. 28).

Yoo, J. (2010), *General Relativistic Description of the Observed Galaxy Power Spectrum: Do We Understand What We Measure?*, Physical Review D **82** 083508, arXiv:1009.3021 [astro-ph], ISSN: 1550-7998, 1550-2368, URL: `http://arxiv.org/abs/1009.3021` (visited on 23/06/2025) (cit. on p. 18).

Zwicky, F. (1953), *Species of cosmic matter.*, The Astronomical Journal **58** 237, ISSN: 00046256, URL: `http://adsabs.harvard.edu/cgi-bin/bib_query?1953AJ.....58..237Z` (visited on 07/07/2025) (cit. on p. 28).

List of Figures

1.1 Comparing a selection of claims in literature about observer peculiar velocity as inferred from a late universe dipole. We see that while some measurements are in general agreement with the CMB measurement (vertical dashed line), other can display a tension up to 4.9σ. Measurements and errors are reported from Darling (2022), Dam, G. F. Lewis and Brewer (2023), P. d. S. Ferreira and Marra (2024), Mittal, Oayda and G. F. Lewis (2023), Tiwari et al. (2024) and Planck Collaboration et al. (2020). Also see Fig. 1 of P. d. S. Ferreira and Marra (2024) for a comparison between a different set of late universe dipole measurements. 3

1.2 Wedges from early and modern surveys illustrating filaments and voids in the large scale matter distribution: (a) Center for Astrophysics (CfA) Survey (Lapparent, Geller and Huchra, 1986); (b) 2 degree Field Galaxy Redshift Survey (2dFGRS) (Cole et al., 1998); (c) Sloan Digital Sky Survey (SDSS)(Gott III et al., 2005); (d) Dark Energy Spectroscopic Instrument (DESI) Survey (with inverted colors) (DESI Collaboration et al., 2016). 6

1.3 Visualizing impact of linear-order general-relativistic redshift-space distortions (GRRSD). Simulated large-scale matter distribution on an observer light-cone shown within an equatorial slice ($z \in [-250, 250]\ h^{-1}$Mpc) and with a Gaussian smoothing kernel ($\sigma = 1.8$px). Top Left: Dark matter overdensities as represented in their real-space positions. Top Right: Same filaments and voids after including GR-RSD in heliocentric frame. Bottom Left: The difference between real-space overdensities and the overdensities represented in redshift space for an observer in the CMB frame. Here, one can see large-scale concentric compression (Kaiser effect). Bottom Right: The difference between overdensities in redshift space for CMB and heliocentric frames. The most noticeable effect is the dipole in the overdensities induced by the observer velocity. While these features are already suggestive, the full cosmological information encoded in these distortions can only be harvested with the systematic modeling and estimators described later in this thesis. See §2.2.2 for details of the LIGER method used to generate these mock observations. 8

2.1 Legendre polynomials (left) and Spherical Bessel Functions (right) computed for a range of different ℓs. These functions serve as helpful basis for projecting out the multipole structure of redshift space distortions and estimating the different multipole orders of two-point statistics. 30

2.2 Illustration of three possible parameterizations available for wide-angle formalism as discussed in Reimberg, Bernardeau and Pitrou (2016). `LIGER` papers adopt the mid-point parameterization as it is the standard chosen within the Euclid collaboration. The observer is depicted by a (stable-diffusion generated) cartoon of Euclid at the bottom. 33

2.3 Power spectrum multipoles estimated for a Euclid like survey using a Yamamoto-Bianchi estimator. The different curves represent estimates for different catalogs $\mathcal{R}$ (real-space with no distortions), $\mathcal{G}$ (all relativistic effects in CMB rest frame) and $\mathcal{O}$ (all relativistic effects with peculiar velocity). In real-space, only the monopole is non-zero. Peculiar velocity of galaxies introduce power in $\ell = 2$ and $\ell = 4$ (Eq. 2.13) and observer peculiar velocity leaves an imprint across all multipoles on the largest scales (Eq. (2.37)). The inset figures zoom into the bandwidth relevant for the FOTO signal. Barring the FOTO signal, monopole term remains the dominant contribution to the total power. Note that $kP(k)$ is plotted (instead of $P(k)$) and, hence, the shape of the curves is artificially lifted for larger values of k. 38

2.4 Theoretical expectations for FOTO effect computed for a Euclid-like survey in a redshift bin of $z \in [0.9, 1.8]$, assuming an observer velocity of v_o = 369km/s. The even multipoles appear with a real part while for the odd multipoles only the imaginary component survives. However, this only reflects the anti-symmetry of our estimator. We can easily choose a different convention which leads to imaginary even multipoles and real odd multipoles. The theoretical expectations for the FOTO signal are compared with measurements of simulated mocks in §3. 38

2.5 LIGER method workflow used in this thesis. MonophonIC generates Newtonian N-body snapshots from Einstein–Boltzmann-consistent initial conditions; after conversion to Gadget-2 format these snapshots are processed by *LIGER*, which finds light-cone intersections and performs line-of-sight integrations to build fully relativistic dark-matter catalogs. *Buildcone* performs baryon painting based on survey functions to obtain a galaxy-overdensity map, which feeds the *Statistics* step (i.e. computing power-spectrum multipoles, signal-to-noise ratio of the FOTO signal, Bayesian inference for observer velocity, etc.). 41

2.6 Survey functions for SKAO2-like and Euclid-like surveys plotted according to the prescription by Maartens et al. (2021). These functions, with the exception of the evolution bias $\mathcal{E}$ for HI tracers, are used to create mock galaxy catalogs. The evolution bias for HI tracers fails self-consistency test and, hence, a differently calibrated function is utilized for the final mocks. 45

2.7 The classical and observed values of α computed for Euclid-like and SKA-like survey functions over a range of redshifts. This figure suggests that the amplitude of the FOTO signal should be higher for Euclid like mocks. This observation is verified in the results discussed in the next chapter. 47

2.8 Testing the self-consistency of the survey functions prescribed by (Maartens et al., 2021) based on the Eq. (2.64). While the Euclid survey functions are self-consistent, the SKAO2 survey functions fail to satisfy this consistency check. Thus, we modify the evolution bias by calibrating it with respect to the LHS of Eq. (2.64) for our further analysis. 48

2.9 Comparing the number density provided to `Buildcone` via input survey functions with the number density reconstructed from the output catalogs. For both survey types, our baryon painting procedure faithfully reproduces the theoretical inputs. Vertical gray lines in the figure represent the tomographic redshift bins considered in Fig. 3.1 and Fig. 3.2. The reason why the fluctuations appear to have higher frequency for Hα is that the redshift histograms were binned in equal sizes of redshift but are plotted in units of comoving distance. 49

3.1 Finger-of-the-Observer effect across various redshift bins and multipole orders for an HI type redshift survey. The various panels demonstrate that the mean of mock measurements agree very well with the model predictions. For this specific choice of survey functions, the FOTO signal decays quickly with increasing redshift. The red shaded region represents 1σ scatter of the FOTO measurement across different realizations. 52

3.2 Similar to Fig. 3.1 but for Hα survey type. Here, again, the measurements provide excellent agreement with the model. Notably, the FOTO amplitude is higher than HI survey functions and remains noticeable even in farther redshift bins. The oscillations happen at a higher frequency and higher multipoles survive even at smaller scales where the monopole signal is dampened. 53

3.3 FOTO multipole measurements for widest Euclid bin allowed by our survey functions i.e. $z \in (0.9, 1.8)$. This is the highest amplitude for the FOTO signal that we can achieve with the smallest scatter across various configurations. Thus, for the remainder of our statistical analysis, we will use the power spectrum measurements of this redshift bin. 54

3.4 Comparing the likelihood ratios for the null hypothesis (Blue) of being at rest with the CMB frame and the alternate hypothesis of observing FOTO effect (red) as computed for monopole-only and all-multipoles cases. The figure suggests an increase in the SNR when higher multipole orders are considered for the null test. The distance between the peaks of the histogram is expressed in terms of the standard deviation of λ_O. 56

3.5 Comparing SNR computed using all combinations of the first five power spectrum multipoles of the null hypothesis (CMB rest frame) and the alternate hypothesis (peculiar velocity's FOTO signal). Different conventions for defining the distance between the peaks of the likelihood ratio distributions lead to different choices for the top-performing multipole combination. The solid and dashed frames represent the highest and lowest signal-to-noise achieved within each convention. 57

3.6 Comparing the posterior distributions for a single realization inferred using likelihood with only monopole, only even multipoles, only odd multipoles and all multipoles of the FOTO signal. Shaded regions represent the 68% confidence intervals. Colored vertical lines represent the median velocity of the corresponding distribution and the gray dashed line represents the fiducial velocity. A generalization of these results across all realizations is shown in Fig. 3.7. 59

3.7 Posteriors for $v_\odot$ in $z \in (0.9, 1.8)$ for monopole, even, odd, and all multipoles (12 bins per multipole with $\delta k = 0.34 \times 10^{-3}\, h\,\mathrm{Mpc}^{-1}$). Horizontal lines represent the fiducial $v_\odot$. Average half-width highest posterior density intervals are $\bar{\Delta}\mathrm{HPDI}_{\ell=0} = 63.6$ and $\bar{\Delta}\mathrm{HPDI}_{\ell=0,1,2,3} = 49.5$. Histograms in the right columns represent the scatter of median velocity in the MCMC chains across realizations. 60

3.8 Effect of number of bins considered (per multipole; $\delta k = 0.346 \times 10^{-3}$ h/Mpc) on the half-width of the HPDI with (solid) and without (dashed) applying finite-sample correction to the covariance during inference of $v_\odot$. The different line colors depict inference results using different sets of power spectra multipoles. Without the Hartlap correction, preparing data vectors with concatenated multipoles can provide up to 30% tighter constraints on velocity. The correction inflates confidence intervals and the advantage in using longer data vectors is substantially subdued. 61

3.9 Distribution of best-fit $v_\odot$ over 125 mocks using Hartlap-corrected covariances for Bayesian inference. The scatter of best fits tightens from $\sigma = 57.6\,\mathrm{km\,s^{-1}}$ to $\sigma = 44.6\,\mathrm{km\,s^{-1}}$ ($\approx 23\%$ reduction), hinting at extra information in higher multipoles. However, the average 68% HPDI does not shrink case due to a higher finite-sample correction to the precision matrix (see Fig. 3.8), motivating compression. 62

3.10 This figure compares the average half-width HPDI for Hartlap-corrected inference chains before (left) and after (right) re-binning to wider bandwidths. Looking at the bottom panels, one notices that by re-binning, the competing influences of higher multipoles and precision matrix debiasing can be neatly disentangled. The curves in bottom right column stay consistently above zero (reaching almost 12.5%) indicating a clear (albeit small) advantage in using higher multipoles. However, the top panels reveal that this relative gain arises not because re-binning genuinely shrinks the HPDI but because the signal in the monopole is washed out and it's constraining power is diluted. 63

3.11 Heatmap illustrating the magnitude of terms in the correlation matrix for power spectra multipoles of $\mathcal{O}$. The left and right panels compare the correlations before and after re-binning from $\delta k = 0.34 \times 10^{-3}\, h\,\mathrm{Mpc}^{-1}$ to $\delta k = 1.14 \times 10^{-3}\, h\,\mathrm{Mpc}^{-1}$. Even after re-binning, the cross-multipole correlations survive (as seen in the off-diagonal banded structures on the left) and eliminating these require different compression techniques. 64

3.12 Eigenvalue spectra (top) and cumulative variance (bottom) for covariance of power spectra measurements of $\mathcal{O}$ and $\mathcal{G}$. The left and right columns compare the cases of considering only monopole against considering higher multipoles before performing PCA. In both cases, the spectra falls sharply in the presence of FOTO signal and most of the covariance can be reconstructed with projections along only a few eigenvectors. 65

3.13 (Left) Relativistic distortion to a slice of overdensity field contributed by the observer velocity term. In 2D, the gradient demonstrates a planar symmetry that is a projection of a dipole in the angular power spectrum. See the caption of Fig. 3.13(a) for details on the production of this illustration. (Right) Figure reproduced from Euclid Collaboration et al. (2025) showing angular power spectrum measurement of the FOTO signal's contribution to the overdensity field in a Euclid-like survey. In the C_ℓ representation, we find that the entire signal resides in the dipole term for full-sky and only leaks into higher multipoles when convoluted with a window function. 68

3.14 Figure reproduced from (Elkhashab, Porciani and Bertacca, 2024) summarizing the variation of signal-to-noise for FOTO monopole-only measurements in Hα widest bin with respect to sky coverage fraction. The red-cross is indicative of a realistic Euclid-like survey footprint with approximately one-third sky fraction. The impact of partial sky-coverage on inference with higher-multipoles remains to be seen. 70

3.15 A recreation of Fig. 1.1 to highlight the potential constraining power of the PCA compressed multipoles of the FOTO signal (for one specific realization). An important caveat in this comparison is that other measurements come from partial sky footprints and the FOTO projections are presented assuming full-sky coverage. Applying realistic survey masks would lead to a drop in the FOTO amplitude as shown in Fig. 3.14. Measurements are quoted from Darling (2022), Dam, G. F. Lewis and Brewer (2023), P. d. S. Ferreira and Marra (2024), Mittal, Oayda and G. F. Lewis (2023), Tiwari et al. (2024) and Planck Collaboration et al. (2020). Gaussian errors are assumed for ease of illustration. 71

List of Tables

3.1 Summary of inference results and their sensitivity to binning and compression choices. The average half-width HPDI are reported for the best configurations found for each case. The last column reports the relative gain in constraining power of a particular combination of multipoles over the posteriors inferred using the monopole only. . . . 66
3.2 A summary of the number of principal components required to capture 95% of the covariance across tomographic redshift bins of SKA-like mocks. 67